Review

Helium-3 spin-echo: Principles and application to dynamics at surfaces

A.P. Jardine [a,*], H. Hedgeland [a], G. Alexandrowicz [b], W. Allison [a], J. Ellis [a]

[a] The Cavendish Laboratory, JJ Thomson Ave., Cambridge, CB3 0HE, UK
[b] Schulich Faculty of Chemistry, Technion – Israel Institute of Technology, Haifa 32000, Israel

ARTICLE INFO

Commissioning Editor: Dr. H. Petek

Keywords:
Surface dynamics
Diffusion
Helium atom scattering
Quasielastic scattering
Spin-echo
Interatomic potentials

ABSTRACT

In this review we give a detailed description of the recently developed helium-3 spin-echo technique and its application to several classes of surface dynamic measurements. We review existing surface dynamical probes briefly and illustrate the need for new experimental tools that measure on nanoscale distances and over picosecond timescales. We then describe the helium-3 spin-echo method, which is one such tool, together with the approaches used to describe such measurements and the instrumentation developed to realise its application. The main application of helium-3 spin-echo is the study of surface dynamics, hence we review the approaches which have been established to interpret dynamical data and the signatures for various forms of motion, before going on to summarise the experimental studies to date. We also describe Fourier transform atom spectroscopy, a new method for measuring elastic and resonant scattering that is facilitated by the availability of spin-echo instruments. Finally, we look towards future scientific challenges for the technique.

© 2009 Elsevier Ltd. All rights reserved.

Contents

* Corresponding author. Tel.: +44 1223 337207; fax: +44 1223 350266.
  E-mail address: apj24@cam.ac.uk (A.P. Jardine).

1. Introduction

Understanding the fundamental dynamical behavior of atoms and molecules on surfaces presents one of the remaining major challenges in the well established, but consistently rich, field of surface science. Many surface experimental techniques [1] have been used to provide information about both adsorbate and substrate vibrational modes, including infra-red spectroscopy [2], electron energy loss spectroscopy (EELS) [3] and inelastic helium atom scattering (HAS) [4,5]. Similarly, many techniques have been applied to study diffusion of atoms and molecules on surfaces, providing a comprehensive body of literature [6,7]. The main focus in early experimental work was to deduce diffusion constants and hence make a connection to macroscopic diffusion theory [8]. More recently, the availability of high spatial resolution has led to a "bottom-up" approach in which the emphasis has changed to one of understanding surface mass-transport starting with the atomic scale dynamics of adsorbate motion. However, despite these efforts, there is still relatively little experimental knowledge about the fundamental nature of aperiodic diffusive processes on both atomic length-scales and nanosecond to picosecond timescales. Microscopic measurements, particularly on fast timescales are extremely challenging since most experimental techniques operate on either much longer length-scales, or on much slower timescales.

Generally, the lack of knowledge in this region is not related to any perceived lack of interest. In fact, a detailed knowledge of atomic scale diffusive behavior is crucial to understanding a great many technologically important processes. For example, self assembly of nonstructural, heterogeneous catalysis, and epitaxial growth of semiconductor structures all involve a crucial mass-transport step, which determines the resulting rate and occasionally limits the process. More fundamentally, it is only on atomic length-scales that the discrete nature of atomic and molecular diffusion is revealed, which corresponds to the point where theory requires more than simple diffusion constants and Fick's famous laws of diffusion [9] to describe the underlying physical behavior. Similarly, it is only at elevated temperatures, when atoms and molecules can move readily on fast timescales, that many complicated forms of atomic scale motion emerge. Such motion is characteristic of the interatomic potentials and of the rates of energy transfer that underlie physical systems.

In this article, we review the recently developed helium-3 spin-echo technique (^{3}HeSE), a novel approach which allows these outstanding issues to be addressed experimentally. In fact, ^{3}HeSE provides a generic ultra high energy resolution scattering tool for studying surfaces. The key feature of the approach is that the energy change of individual ^{3}He atoms is measured directly when they scatter from the surface, rather than in relation to the energy of the beam as a whole. Crucially, the initial distribution of energies in the helium beam – previously the major experimental limitation – is overcome. The ^{3}HeSE technique is particularly appropriate for measuring adsorbate dynamics at surfaces, as it provides surface correlation measurements in the picosecond to nanosecond time range. Spatial sensitivity is determined by the momentum of the helium atoms and scattering geometry of the instrument, which places the technique in the sub-nanometre range of greatest experimental interest. To date, application of ^{3}HeSE remains dominated by measurements of adsorbate dynamics, although it has also been applied to a number of problems in elastic and inelastic scattering.

The present review is arranged in the following way. In Section 2 we set the context for ^{3}HeSE measurements. We give a brief overview of the theory used to describe diffusion on surfaces and existing experimental approaches. We then summarise the elastic and inelastic helium atom scattering techniques in relation to recent work, before describing the quasi-elastic helium atom scattering (QHAS) method for studying adsorbate dynamics. In Section 3, we describe the principles of helium spin-echo. We describe the basic framework within which the experiment can be understood, both in terms of a quantum picture (which provides a useful physical insight into the technique) and a classical model

(which facilitates convenient analysis). In Section 4 we describe the experimental implementation of [3]HeSE and compare the features of the existing helium spin-echo spectrometers. In Section 5, we describe the techniques used to analyse diffusion measurements and report the signatures of various forms of motion that have been established in the literature. Section 6 reviews the experimental results published to date and the unique physical insights obtained. A further application of the [3]HeSE method is to the study of reflectivity variations caused by elastic, resonant scattering of atoms. The method, which we call Fourier transform atom spectroscopy is described in Section 7. Finally, in Section 8 we present a summary and look towards the future for the technique.

2. Background: surface diffusion, helium atom scattering and the role of QHAS

A very extensive body of literature already exists describing surface diffusion studies, including a number of reviews from an experimental perspective [10–12,7,13,6,14] and also from a theoretical viewpoint [15,16,8,17,18]. A further general review of diffusion is beyond the scope of the present work. However, we will briefly summarise a number of the key concepts that are important to set the context for [3]HeSE measurements, and to provide some references where the reader may find more information.

2.1. Models of surface diffusion

The broad term 'surface diffusion' encompasses several distinct concepts. At any finite temperature, surface species are in continuous thermal motion. If the trajectories of individual atoms can be 'traced', through measurements or simulations at the atomic level, the resulting properties are known as *tracer* diffusion [6,15]. For finite coverages, the concept of tracer diffusion is still important, providing the motion of individual species can be distinguished. However, the motion depends on the local configuration of adsorbates in a more complicated way. In the literature, the term *collective* or *chemical* diffusion refers to the macroscopic transport of many particles over large distances. Collective diffusion is determined by Fick's laws, and applies in the presence of concentration gradients but ceases as the concentration gradients tend to zero. It should not be confused with correlated tracer motion on the atomic scale, which also has a collective nature. Clearly, a realistic model of collective diffusion, to compare with experiment, requires many physical processes to be accounted for, including diffusion in a range of coverage regimes, over terraces, step edges, etc. The concept of tracer diffusion is much simpler, and is most likely to form the building blocks of the former.

With modern computers it is time consuming but straightforward to simulate the classical motion of an assembly of particles, such as a slab of surface atoms supporting a mobile adsorbate [19,20]. The simulated (tracer) properties of the surface atom may be extracted and analysed. In theory, these 'computational experiments' enable predictive simulations, but are reliant on the quality of the force-fields involved, which is unknown for most surface systems. In addition, the large number of degrees of freedom often make it difficult to attribute resulting characteristics to specific input parameters, and therefore to gain useful physical insights.

Generally, the starting point for analytic considerations of atomic scale surface motion is the concept of a particle moving classically in a 1D lateral potential, as illustrated in Fig. 1. When the temperature is low, $k_B T \ll E_b$, the adsorbate is generally confined to the bottom of the adsorption well and a simple hopping rate, Γ, can be obtained using the Arrhenius relationship [15],

$$\Gamma = v_0 \exp\left(-E_b/k_B T\right), \tag{1}$$

where E_b is the diffusion barrier and v_0 is a pre-exponential factor or attempt frequency. v_0 is often taken to be the frustrated translational vibrational mode (T-mode) frequency of the atom in the bottom part of the potential well. The simple model may be generalised into 2D, and corresponding expressions have been obtained [6] for tracer diffusion constants, D^*, in terms of hopping rates, to enable comparison with experiment.

Rate theories such as transition state theory (TST) [8] have been widely used to provide estimates of the hopping rate, given the statistical thermodynamic properties of the system. In this case, the
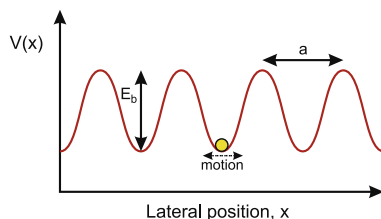
Fig. 1. Schematic illustration of an atom moving in a 1D lateral potential energy surface (PES). The corrugation of the potential forms an energy barrier to diffusion, E_b. The atom occasionally gains enough energy to cross the barrier, resulting in hopping diffusion. Between such events the atom oscillates around the energy minimum, the frequency of the vibration being given by the mass and local curvature of the potential. Note that although $V(x)$ is expected to have the same periodicity, a, as the substrate, the complex nature of the possible adsorbate–surface interactions mean that there is no general criteria for the position of the potential extrema within a unit cell.

underlying idea is to use the ratio of the partition functions in the transition state, Z_s, to the well state, Z_0, to provide an estimate of the hopping rate, given by [15]

$$\Gamma = \frac{k_B T}{h} \frac{Z_s}{Z_0} \exp(-E_b/k_B/T). \tag{2}$$

However, such models take no account of the rate of energy transfer or *friction* between the adsorbate and surface, unlike, for example the Langevin or Fokker–Plank equations [21]. In low friction systems the rate of activation is reduced as the adsorbate only gains sufficient energy to escape the adsorption site relatively infrequently, while also giving rise to long jumps [22]. At high friction, the overall transport rate is also reduced as the friction is high enough to reverse adsorbate trajectories and cause barrier recrossing [23,24]. In fact, TST corresponds to the intermediate friction regime and is only expected to provide an upper limit of the hopping rate [6,23].

High temperatures, when $k_B T \gg E_b$, correspond to an entirely different regime. The adsorbate does not feel the corrugation of the lateral potential and consequently the concept of either a hopping rate or of a transition state does not apply. Adsorbates will undergo either ballistic or Brownian motion, depending on both adsorbate coverage and the frictional coupling to the substrate [6].

A general treatment, which can accommodate these distinct regimes, as well as the vibrational motion of particles, without requiring large numbers of degrees of freedom, is provided by the Langevin dynamics approach [6,15]. Here, the interaction between the adsorbate and the large number of atoms in the surface is approximated by a 'frozen' lateral potential energy surface. Essentially, all the substrate degrees of freedom are integrated out, to yield a 2D potential with characteristics similar to the 1D case shown in Fig. 1, which is usually reasonable providing complex forms of atomic motion, such as exchange processes [15] are not present. The frictional interaction with the substrate is modeled using a frictional coupling parameter, η, which scales both fluctuation and dissipation in the system [25]. Dissipation corresponds to a viscous drag term, while fluctuation is introduced through an additional force term, $\xi(t)$, which mimics random energy impulses applied to the adsorbate from the substrate energy bath. Together, these give the Langevin equations of motion,

$$m\ddot{\mathbf{R}}_i = -\nabla V(\mathbf{R}_i) - m\eta\dot{\mathbf{R}}_i + \xi_i(t) + \sum_{j\neq i} F(\mathbf{R}_j - \mathbf{R}_i), \tag{3}$$

where the stochastic white noise force term $\xi(t)$ satisfies the fluctuation–dissipation theorem, such that the mean force is zero and

$$\langle \xi(t)\xi(t-\tau) \rangle = 2m\eta k_B T\delta(\tau). \tag{4}$$

The final term in Eq. (3) accounts for finite coverages, by including the force on each adsorbate due to the presence of j other adsorbates on the surface, due to forces, F, between adsorbates. The presence of this term introduces the possibility of correlated effects, ranging from simple site blocking to phase transitions. These approximations are entirely classical, but work well providing atoms are not too

light and adsorbate–substrate forces are not too strong [15], that the adsorbate–adsorbate and adsorbate–substrate forces are separable, and that the pairwise force approximation is valid (see Section 6.2.2). The classical approximation is usually good, with the notable exception of the diffusion of hydrogen or deuterium, where the adsorbate mass is sufficiently small that quantum effects must be accounted for.

Historically, the very different timescales between surface diffusion measurements (see below) and measurements of adsorbate vibrational modes led to the two phenomena being treated quite separately. However, it has since become clear that the two are intimately linked. The frustrated translational vibration (T-mode) [26] frequency gives a guide to the hopping attempt frequency, v_0, or can be used to provide the curvature of the lateral potential around the adsorption site [27–30]. Similarly, recent work suggests that in molecular systems, transport may be limited by the excitation of other vibrational modes, such as the frustrated rotation mode [31]. Within the Langevin framework, both vibration and diffusion are treated equally, enabling a complete dynamical description to be produced, starting with the vibrational period and extending to longer timescales.

A different analytical approach is the interacting single adsorbate (ISA) model developed recently by Miret-Artes et al. [32–35], discussed in more detail in Section 5.3.4. As well as simplifying the adsorbate–substrate interaction, as before, the ISA model also replaces the adsorbate–adsorbate interaction with a shot noise term. It provides an empirical, but nonetheless quantitative, description of some features, such as the coverage dependence of average hopping rates, without needing to reproduce the exact form of the adsorbate motion.

A number of approaches have been adopted to obtain dynamical information from the Langevin equations. Direct numerical integration is the most common approach and has been used widely in both theoretical investigations and in the interpretation of QHAS measurements, as discussed below. The main disadvantage is that, in order to compare with experiment, many particles and long simulation times are needed so that the calculations are expensive to perform. Alternatively, Kramers' turnover theory [16,8] provides information about jump rates and subsequent diffusion constants. Further analytical solutions can be obtained under special circumstances [18,8,15], using the equivalent Fokker–Plank equation (which describes the distribution of possible trajectories) and methods such as the matrix-continued-fraction approach [18,36] or the Mori projection operator formalism method [17,15]. Considerable insights have been obtained including, for example, information about jump distributions and rates for a variety of different potentials and damping regimes [23,22,37], the importance of memory effects [38] and the nature of sub- and super-diffusion and Levy flights [39].

A key issue, which we hope will be clear to the reader, is that while various models can be used to derive macroscopic diffusion coefficients, given sufficient microscopic detail about a particular system, the reverse is not possible. In other words, macroscopic diffusion constants, as have frequently been reported in the literature, do not adequately describe the rich spread of physical behavior expected on the microscopic level in real systems. Measurements of detailed atomic scale information is therefore crucial for benchmarking any microscopic theory.

2.2. Experimental approaches to surface diffusion

A considerable number of experimental techniques have been developed to study diffusion of particles on surfaces. Comprehensive descriptions of many have already been given in reviews by Gomer [7], Barth [6] and others [10,12,40]. Here, we give an overview to enable the reader to distinguish the similarities, differences and benefits of the spin-echo QHAS technique that we describe below.

Following Gomer, we observe a distinction between two broad classes of diffusion measurement; profile evolution techniques and equilibrium methods. Profile methods involve establishing an initial concentration gradient on the surface, such as a simple step profile, whose time evolution is then monitored and used in conjunction with Fick's laws to determine the collective diffusion coefficient, D_c. A variety of techniques have been used to monitor the concentration profile, such as work function probes, scanning auger microscopy (SAM), photoemission electron microscopy (PEEM) and even helium reflectivity, depending on their suitability to the systems being studied [7]. One of the most important approaches is laser induced thermal desorption (LITD), where the entire surface is covered, then a focused laser is used to repeatedly desorb a small region of the surface coverage into a mass

spectrometer, enabling the rate of refilling and hence D_c to be obtained. More recently, laser optical diffraction (LOD) has been developed to enable more delicate measurements. In this case, an optical grating pattern is desorbed from the surface, which decays as the overlayer diffuses. An important point to consider when analysing data from any laser based technique is the potential for surface damage, as has recently been observed [41]. Electron based microscopic and spectroscopic techniques are also susceptible to inducing surface damage, ranging from electron stimulated desorption of weakly bound species to the serious forms of damage often seen in high power electron microscopes.

Fig. 2 gives a graphical comparison of the length and timescales over which a selection of techniques are sensitive to diffusion. In general terms, imaging techniques occupy the longer timescales while scattering methods offer greater potential in the short timescale region. Techniques, such as laser optical diffraction (LOD), are an intermediate case in that they follow the evolution of a macroscopic, non-equilibrium profile and thus provide important information on macroscopic processes, but rather restricted information about processes on the microscopic scale. Experimental results have therefore been compared with microscopic theory only rather indirectly, usually through macroscopic diffusion constants.

Equilibrium methods generally involve monitoring atomic diffusion or other larger scale fluctuations of in the surface configuration with time. Typical techniques include field ion microscopy (FIM), scanning tunneling microscopy (STM), field emission microscopy (FEM) [7] and fluorescence correlation spectroscopy (FCS) [42]. FEM and FCS provide fluctuation measurements as isolated particles move in and out of a defined measurement volume. They operate on intermediate length-scales, defined by the measurement volume, which enables diffusion constants to be extracted. Both FIM and

Fig. 2. Graphical comparison of the principal experimental techniques which have been applied to surface diffusion, in terms of the approximate length- and timescales to which the measurement process corresponds. Labels indicate primarily microscopic imaging based techniques (**M**), optical or laser based techniques (**O**) and scattering based methods (**S**). Increasing these ranges of applicability is still the subject of ongoing work. Note that simple diffusion processes can be measured using several different techniques over either short lengths and times, or equally over longer lengths and times. However, microscopic phenomena are only evident on atomic length-scales and fast times. Currently, QHAS is the only surface technique which simultaneously allows microscopic length-scales and picosecond to nanosecond timescales to be studied, while the system is in true thermal equilibrium. The figure is constructed using information from [7,6] with additional information on STM [43], FEM [10], FCS [42], LOD/SHD [45,46], PEEM (either limited by phosphor decay/ CCD framing rates [47] or as a pulse synchronised measurement [48,49]). Quasi-elastic neutron scattering (QENS) [50] is only weakly surface sensitive, but is included for comparison with QHAS.

STM provide atomic resolution, enabling hopping of individual atoms to be distinguished. However, they are limited to relatively slow framing rates, at best in the millisecond regime [43,44]. Both require conductive samples and in the case of FIM (as with FEM), very high electric fields are applied, which both restricts the number of suitable samples and may modify diffusion in some systems. Even STM measurements apply a considerable electric field through the presence of the tip, which will affect delicate forms of motion. These microscopic measurements can be applied when the motion is slow enough to allow completion of an image before there has been a substantial amount of motion, for example, between hops in a particularly slow systems, as often encountered at extremely low temperatures. While the real space nature of these techniques provides valuable insights in to the dynamics, the fact that the motion is probed through snapshots does not allow detailed information, such as the path of the motion to be obtained. Consequently, atomic scale hopping results are also frequently expressed in terms of simple diffusion constants, for comparison with other experiments and theory, even though such values do not convey the full breadth of microscopic detail.

In contrast, quasi-elastic scattering measurements, as we describe below, provide a completely different and complimentary approach to equilibrium surface diffusion measurements. As indicated in Fig. 2, they are the only current opportunity to continually monitor fully mobile species on both Angstrom length and picosecond timescales, providing detailed microscopic information for comparison with theory. Both neutrons and helium atoms have the requisite features and resolution for such measurements. QENS has been established for longer and is a better developed technique, giving access to a wider range of measurement timescale. However, neutron beams have a low flux and neutrons scatter extremely weakly from surfaces. Both factors limit the range of surface experiments that are possible and require multilayered samples with extremely large surface areas. Quasi-elastic helium atom scattering offers a much higher beam flux and is fully surface sensitive. Thus, it has the potential to be used much more widely in surface systems.

2.3. Helium atom scattering

As a surface probe, helium atoms have a number of advantages over more conventional surface probes such as electrons. There are a number of comprehensive reviews and several books on the subject describing the technique in detail [51–55,5]. Almost all the important features of the helium scattering technique are relevant to helium spin-echo experiments. The key features of thermal energy helium atoms are, (i) an inert and almost totally non-destructive nature, coming from their uncharged nature and the low energies used, (ii) exclusive surface sensitivity due to scattering from the interaction with the outer surface electrons, and (iii) a wavelength that roughly corresponds to the spacing of atoms in matter.

Nearly monochromatic helium beams are usually produced using a supersonic free jet expansion [56] of high pressure helium ($\sim$100 bar) into vacuum ($\sim 1 \times 10^{-3}$ mbar). The typical thermal helium energies used for scattering experiments are $\sim$1–100 meV, corresponding to nozzle temperatures of 5–500 K. The centreline of the expansion is separated using a skimmer and directed, through several stages of differential pumping, onto the sample. These helium atoms scatter from the sample surface through the interaction between the helium s-orbital and the outer electrons in the surface.

Fig. 3 shows helium-surface scattering in a schematic way. The variation of the scattering potential with distance from the surface, z, is illustrated in the right of the figure and the iso-potential contours shown in the main part illustrate the lateral corrugation. The potential naturally follows the periodicity of the surface, and varies locally with position within the unit cell. Both the weak, long-range attractive interaction and the strong, short-range repulsive wall affect the helium trajectories. The incident helium beam (**A**) can scatter in a number of ways. If there is no energy exchange then the outgoing beam (**B**), corresponds to a specular scattering, as shown, or to elastic diffraction if there is an exchange of crystal-momentum with the surface. In the case of energy exchange with substrate phonons or adsorbate vibrations, the outgoing trajectory (**C**) may be deflected away from the specular direction giving discrete, single-phonon, energy loss/gain features plus the possibility of a broad multi-phonon background. Scattering from moving aperiodically surface species results in a quasi-elastic broadening around the elastic peak, which forms the origin of diffusion measurements and is discussed in much more detail below. It is also possible for atoms to scatter diffractively into an
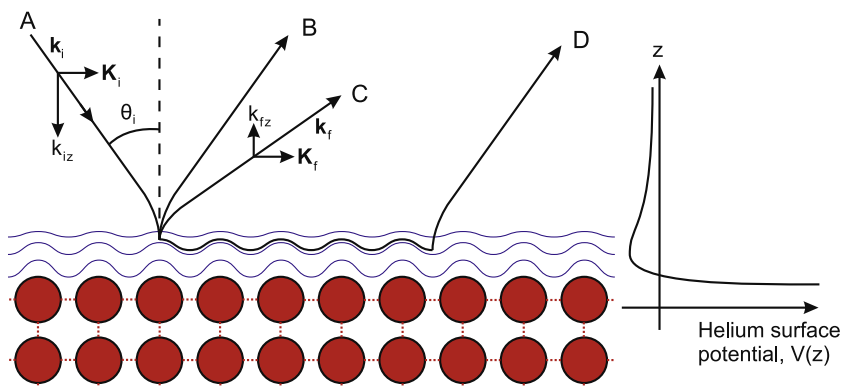
Fig. 3. Schematic illustration of the typical helium-surface interaction potential above a lattice of surface atoms. The potential follows the periodicity of the surface and has the general z-dependence shown. Incoming helium atoms (**A**) can scatter (or diffract) elastically (**B**), scatter inelastically by exchanging energy with the substrate (**C**) or can enter selective adsorption resonance (**D**) where they are transiently trapped in one of the energy levels of the potential well.

evanescent state where they remain localised at the surface but propagate, parallel to the surface, before a second diffractive process scatters the atom away from the surface. The corresponding trajectory (**D**) is indicated in Fig. 3. The phenomenon is known as resonant scattering since interference between the two coherent emerging trajectories, (**B**) and (**D**), leads to strong variations in the diffraction intensity.

A further feature of the helium-surface interaction is the total diffuse scattering cross section of an isolated defect on a surface (e.g. an adsorbed particle) is much larger than its expected geometric size [52]. Farias and Rieder give an overview of recent total cross section determinations for atoms and small molecules [54], indicating $\sim$120 Å^2 is typical. Following comparison with gas phase measurements, these *giant* cross sections are usually attributed to small deviations introduced in helium atom trajectories by long-range dispersive interactions around the adsorbate [52], which scatter the atoms from the specular direction. An important consequence of the *giant* cross section is that HAS is exceptionally sensitive to small adsorbate coverages, making measurements down to $\sim$0.01 ML relatively straightforward.

Key parameters for describing helium scattering experiments are the momentum transfer and energy exchanged during scattering. Measuring energy transfer, $\Delta E = \hbar\Delta\omega$, is usually the subject of the experiment, while momentum transfer is defined by the geometry of the experiment and beam properties. Following the convention shown in Fig. 3 (using capitals to denote surface projected properties), we write the wavevector of the incident helium beam as $\hbar\mathbf{k}_i = m\mathbf{v}_i$, which can be resolved into a surface parallel component, $\mathbf{K}_i$, and a normal component, k_{iz}. For a scattering apparatus with source-sample-detector total scattering angle, θ_{SD}, the momentum transfer parallel to the surface, $\Delta\mathbf{K}$, is given by

$$\Delta\mathbf{K} = k_f \sin(\theta_{SD} - \theta_i) - k_i \sin(\theta_i), \tag{5}$$

where θ_i is the angle of incidence.

2.3.1. Elastic scattering: structure and growth in the quasi-static limit

Elastic helium scattering experiments from static, or quasi-static, surfaces can be broadly divided into (i) diffraction experiments, (ii) specular and diffuse scattering experiments and (iii) selective adsorption experiments. Diffraction experiments date back to the pioneering work of Frisch and Stern [57,58]. They enable the periodicity of the surface to be examined through diffraction peak locations, and the morphology of the unit cell to be understood through the respective peak intensities. Since the helium atoms scatter from the electron density at the surface, rather than the ion cores, the method is particularly suited to studying small adsorbates, such as H atoms [51,59,60].

Additionally, close packed metal surfaces typically appear uncorrugated, providing an opportunity to study adsorbate phases since the diffraction intensity arises almost exclusively from the adsorbates. The technique has been applied to many adsorption structures on metals, semiconductors and insulators [51,54]. Recently there has been increasing use of helium scattering to study larger molecules, e.g. [61,62] or alkanethiol self assembled monolayers, e.g. [63,64]. HAS is also finding useful application in understanding systems where traditional techniques, such as electron spectroscopies, are less appropriate. Particular applications are insulator surfaces, e.g. [65] and delicate ice/water surfaces e.g. [66–68].

Helium scattering has also been widely used to monitor physical processes on both ordered and disordered surfaces through changes in specularly reflected intensity [52]. Epitaxial growth may be monitored rather precisely through specular intensity oscillations, as adatoms form first isolated defects, reducing specular intensity, before coalescing into complete layers and causing the specular intensity to recover. The overlap of giant cross sections with increasing coverage, as monitored during uptake using the specular helium intensity, enables information about the adsorbate interatomic forces to be obtained. Both repulsive and attractive forces have distinct signatures [52], as does, for example, the condensation of a 2D gas into a condensed phase with increasing coverage. These techniques have been applied to a number of physical systems [54,53,52,51]. Applications included studying isolated and step edge cross sections and densities, nucleation and thin film growth processes, phase and order–disorder transitions, and even macroscopic diffusion through the profile evolution approach. Such measurements also provide key background information for quasi-elastic scattering measurements of diffusion.

Another field which can be studied using elastic scattering is the phenomena of selective adsorption resonance (SAR) [54,53,69], which occurs when incoming helium atoms satisfy the kinematic condition,

$$E = \frac{\hbar^2 \mathbf{k}_i^2}{2m} = \frac{\hbar^2 (\mathbf{K}_i + \mathbf{G})}{2m} + E_n(\mathbf{K}_i, \mathbf{G}) \tag{6}$$

and become trapped in a z bound state of the helium-surface potential, E_n, while remaining free to move parallel to the surface. After some time, depending on the corrugation and quality of the surface, the bound atoms scatter back into an outgoing diffraction channel. Such resonances were originally observed by Frisch and Stern [57,58] and have since been studied using several methods, including spin-echo techniques. The position, shape and widths of resonances provide a powerful route to accurate experimental determination of the attractive part of the helium-surface potential, and hence provide an exceptionally sensitive test of any corresponding theory.

A precise model of helium-surface scattering is rather complicated, due to the extended nature of the interaction with the surface, unlike the related case of thermal neutron scattering, where simple s-wave scattering applies [50]. Elastic helium scattering calculations require both a realistic helium-surface potential and a suitable scattering calculation scheme. Both empirical and theoretical approaches have been used to establish interaction potentials. For scattering calculations, a range of accurate and approximate techniques have been established. The main, exact, quantum mechanic methods are the wavepacket propagation method [70] and the close-coupling method [71], which have been compared recently by Nave and Lemoine [72]. However, these are computationally intensive, particularly for systems with large unit cells. A number of approximate methods have been developed using both realistic potentials and simplified hard corrugated wall interactions. The sudden approximation [73] provides a convenient soft wall approach, and approximations such as the RR and eikonal method [54,51] may be used in the hard wall case. Finally, in the case of scattering from isolated particles, it is convenient to make use of the simplest kinematic approximation, where the scattered intensity can be written as

$$I(\Delta \mathbf{K}, \Delta \omega) = S(\Delta \mathbf{K}, \Delta \omega) \cdot |F(\Delta \mathbf{K}, \Delta \omega)|^2, \tag{7}$$

in terms of an intensity structure factor, S, given by the position of the scatterers on the surface, and an amplitude form factor, F, which describes the shape of each scatterer on the surface. Such an approximation is particularly useful for very large systems, where other methods are still infeasible.

2.3.2. Inelastic scattering: periodic dynamical processes

High resolution inelastic helium atom scattering measurements were made possible by two principal technical developments. Firstly, the development of supersonic nozzle sources yielded sufficiently monochromatic helium beams, with a velocity spread of 1% or lower. Secondly, time-of-flight instrumentation, including highly differentially pumped scattering instruments with sensitive, fast temporal response detectors, provided accurate measurement of the scattered beam velocity distribution. A comprehensive overview of these experimental approaches has been given by Toennies [74].

Inelastic helium scattering has been applied to study a range of surface phenomena. Most importantly, the technique has provided a huge amount of empirical information about surface phonons [5,53,75], where previously little was available. Such measurements provide information about interatomic interactions and have shown significant differences between the surface and bulk force constants. Phonon dispersion curves are readily measurable, although the practical resolution limit of ∼0.3 meV [76] presents a significant lower energy limit. Linewidth measurements (providing lifetime and anharmonicity information) are limited to those with an intrinsic width which is at least a considerable fraction of the resolution. Broad, multi-phonon backgrounds have also been measured [53].

A wide range of low energy adsorbate vibrations, such as the frustrated translational vibrational mode (*T*-mode) have also been measured [26,77,76]. The lateral *T*-mode is particularly relevant to surface diffusion studies as its frequency provides information about the curvature of the lateral PES around the adsorption site, while its width is often taken as a measure of the adsorbate–substrate energy coupling (friction) [76]. *T*-mode frequency shifts and broadening with temperature also provide PES anharmonicity information, although as in the case of phonons, accurate measurements are not always possible, particularly for narrow linewidths (long lived vibrations in low friction systems) or for very low energy vibrations (weakly corrugated surfaces or large adsorbate masses). Fortunately, spin-echo techniques further improve the resolution for inelastic scattering, such that very narrow linewidths can now be measured [78].

2.3.3. Quasi-elastic helium atom scattering: adsorbate dynamics and surface diffusion

When a beam of helium atoms scatter from mobile species on a surface, individual helium atoms can exchange energy with the surface atoms. Periodic processes, as described above, give rise to the exchange of well defined quanta of energy. In contrast, aperiodic motion, such as hopping between adsorption sites, gives a continuum of small, but measurable energy transfers with the surface, in a process analogous to a Doppler broadening. Each individual energy exchange is different, but the distribution is centred around the elastic peak and so, when averaged over the whole beam, gives a *quasi-elastic* broadening of the elastic peak. The extent of the broadening depends on the rate and mechanism of the diffusion. The principle of quasi-elastic helium atom scattering (QHAS) measurement [79] is to use these quasi-elastic energy broadenings to provide a detailed description of adsorbate dynamics, as discussed in Section 5.

Such measurements can be made with exactly the same high resolution time-of-flight instrumentation as used the for the inelastic measurements described above. Time-of-flight techniques were first applied to QHAS measurements in the late 1980's by Frenken et al. [80] to study surface pre-melting of lead. The technique was quickly applied to adsorbate diffusion by Hinch et al. [81], shortly followed by the observation of microscopic jump diffusion by Ellis and Toennies [82]. Since then, around ten systems have been studied using TOF QHAS. A comprehensive review of the approach and early experimental work and was published by Frenken and Hinch [83]. More complete reviews of the systems to which TOF QHAS has been applied have been published by Jardine et al. [84] and Graham [76].

The framework within which QHAS diffusion measurements have been understood comes from the ideas developed by van Hove and others in the 1950's to describe neutron scattering [50]. In particular, Van Hove showed [85] that the dynamic structure factor, $S(\Delta\mathbf{K}, \Delta\omega)$, is related to the pair correlation function, $G(\mathbf{R}, t)$, by a double Fourier transform in both space and time,

$$G(\mathbf{R}, t) \stackrel{Spatial\ FT}{\Longleftrightarrow} I(\Delta\mathbf{K}, t) \stackrel{Temporal\ FT}{\Longleftrightarrow} S(\Delta\mathbf{K}, \Delta\omega). \tag{8}$$

The pair correlation function, $G(\mathbf{R}, t)$, can be interpreted classically as the probability of finding an atom at $(\mathbf{R}, t)$ providing there was an atom at $(0, 0)$. It can be subdivided into the sum of a self part (same atom) and a distinct part (different atom). Within the kinematic approximation, $S(\Delta\mathbf{K}, \Delta\omega)$ is proportional to the observable quantity in an ideal TOF experiment, provided the momentum-transfer and energy-transfer dependence of the scattering form factor is weak and can be neglected (see Eq. (7)).

The Fourier relationship in (8) indicates the principal benefit of the QHAS technique: since QHAS experiments typically probe momentum transfers between 0 and 4 Å^{-1} and energy changes much less than 1 meV, they provide microscopic tracer information on both Ångström length-scales and picosecond timescales. In effect, QHAS continually monitors microscopic surface motion over the entire substrate, rather than just providing snapshots of the mobile species in adsorption sites. QHAS therefore provides exactly the fundamental information required to relate models of adsorbate motion to experiment, as discussed in Section 2.1. As illustrated in Fig. 2, no other surface experimental techniques provide information from this regime. Only quasi-elastic neutron scattering (QENS), the bulk analogue of QHAS, can provide similar information, but due to the weak scattering of neutrons at surfaces can only be applied to layered samples with extremely large effective surface areas. Quasi-elastic helium and neutron scattering therefore provide complimentary surface and bulk measurement techniques [86]. Recent work has been used to confirm the equivalence of the information given by the two techniques [87], as a precursor to combined studies where both 3D and surface contributions are important, e.g. in 3D zeolite matrices or inside carbon nanotube arrays.

The energy resolution in the present generation of state-of-the-art instruments presents a serious limitation to TOF–QHAS. The monochromaticity of ^{4}He beams are limited both fundamental and technically to about 0.1 meV, but more usually $\sim$0.3 meV [76]. Consequently, TOF–QHAS is limited to studying a relatively few, exceptionally fast moving systems, when the quasi-elastic broadening is comparable to or larger than the beam monochromaticity. Even when a quasi-elastic energy broadening can be clearly resolved, the limited energy resolution can convolve two or more processes together, such as inter-unit cell diffusion and vibrational dephasing (intracell diffusion) [88]. Fortunately, the helium-3 spin-echo technique circumvents these resolution limitations, enabling a much wider range of processes to be clearly distinguished, dramatically increasing the scope of the technique.

A number of the early QHAS measurements yielded diffusion barriers substantially lower than other techniques, which were better established at that time. The differences are discussed in [89–91] and summarised conveniently in [92]. The lower barriers given by QHAS arise because they are dominated by microscopic processes over atomically flat terrace regions, while many of the other techniques average over larger areas, so are more likely to be affected by defects, such as step edges. This is an important point since it highlights the fact that QHAS is sensitive to the fastest process occurring on a surface, whereas macroscopic measurements are influenced by the rate-limiting step for long-range mass-transport, which may have a very different origin. In the case of transport across a surface step, PEEM measurements show a build up of adsorbates at step edges [93] and re-entrant growth indicating a lack of interlayer mass-transport [94]. Both of these observations, and many others, provide confirmation of significantly higher energy barrier at the step edge. However, even with simple atomic adsorbates, TOF–QHAS measurements can be complicated by contributions due to intra-cell diffusion (vibrational dephasing) [88]. Each contribution to the broadening is convoluted with the intrinsic energy resolution of the measurement and individual components cannot be separated if the resolution is limited. The effect of an incomplete deconvolution is that the effective barrier to adsorbate motion can be lower than the true, adiabatic barrier. The additional resolution available with the spin-echo method helps to eliminate this problem.

3. The helium-3 spin-echo principle

The principle of spin-echo was first developed for neutron beams by Mezei in the early 1970's, as an approach to achieve exceptionally high energy resolution in neutron scattering experiments [95,96]. The concept quickly led to the development of the IN11 beamline at the Institut Laue Langevin

in Grenoble, revolutionising ultra-high resolution measurements of slow dynamical processes in the bulk [50]. In the intervening 30 years, roughly fifteen spin-echo instruments have been developed at neutron scattering facilities around the world [96], and even now a new generation of instruments are currently being developed [97–99]. A detailed comparison of helium and neutron spin-echo techniques is currently being prepared [86].

The helium-3 spin-echo technique was first demonstrated by the DeKieviet and Dubbers group in Heidelberg in 1995 [100,101] when the methods used to manipulate the neutron spin were applied to the nucleus of helium-3; thus combining the benefits of exceptional energy resolution with the established surface technique of helium scattering. The Heidelberg instrument provided an energy resolution improvement of more than three orders of magnitude over time-of-flight methods, dramatically increasing the range of applicability for helium scattering experiments. The spin-echo method in fact provides a general purpose, ultra-high energy resolution technique for analysing scattering experiments. Essentially, the method uses Larmor precession of the nuclear spin of each helium-3 atom as an internal timer on each individual atom in the beam. Unlike time-of-flight, which measures the absolute velocity of all scattered atoms, spin-echo enables only the energy *changes* introduced during scattering to be measured, and hence the initial velocity spread in the helium beam to be rejected. Elastic, inelastic and quasi-elastic scattering all benefit from the improvement in energy resolution offered by the spin-echo method.

The perspective of improved energy resolution is helpful in relating the spin-echo and TOF methods; however, it is more natural to discuss the relationship between adsorbate dynamics and the spin-echo method in the time-domain. As we show below, 'standard' spin-echo measurements provide a direct measurement of the intermediate scattering function, $I(\Delta\mathbf{K}, t)$, as given by Eq. (8) where it relates directly to the van Hove pair correlation function. $I(\Delta\mathbf{K}, t)$ is a *measure of surface correlation*, on the length-scale and direction given by $\Delta\mathbf{K}$, after time t. Both these parameters are conveniently adjustable in the spin-echo experiment: $\Delta\mathbf{K}$, is determined by the energy of the ^{3}He beam, the angle of incidence of the beam on the sample and the total scattering geometry of the experiment. The time, t, is determined by the nuclear-spin manipulation applied by the spin-echo coils, which is adjusted by varying the current in the windings.

Spin 1/2 particle beams, such as helium-3 or neutron beams, may be described by classical Larmor precession in all situations except where the Stern–Gerlach effect is appreciable [102]. Hence, the spin-echo experiment has traditionally been described in terms of classical spin precession [96,78]. Alternatively, semi-classical and quantum formalisms can also be applied [103]. In the remainder of this section we describe the principles of the spin-echo experiment and compare these different approaches. We start with the simple classical description of Mezei. We then compare this with a quantum description of the measurement process, similar to that of Gähler, which provides an intuitive approach to understanding the origin of the sensitivity to surface correlations. Finally, we describe a classical double Fourier transform model [78,104], which provides a convenient framework within which elastic, inelastic and quasi-elastic measurements can all be understood.

3.1. Concept and simple classical model

The concept of spin-echo is illustrated classically in Fig. 4, although details of the instrumentation are discussed in Section 4 below. Initially, a beam of unpolarised thermal energy helium-3 is produced in a supersonic expansion, **A**, typically giving an energy spread of 5–20%. The beam is passed through a magnetic spin-polariser, **C**, which transmits only one polarisation of the beam and aligns the outgoing polarised atoms in one direction, perpendicular to the beamline. The beam is then directed through a precession solenoid field, **D**, where the classical spin vector, **S**, undergoes precession according to the classical equation

$$\frac{d\mathbf{S}}{dt} = \gamma\mathbf{S} \times \mathbf{B}, \tag{9}$$

where γ is the gyromagnetic ratio for helium-3 ($\gamma/2\pi = 32.43$; MHz/T). Since **B** is oriented in the direction of the beam, the spins precesses about the beam direction a number of times, although the exact phase angle accumulated depends on the velocity of the individual atom concerned. The
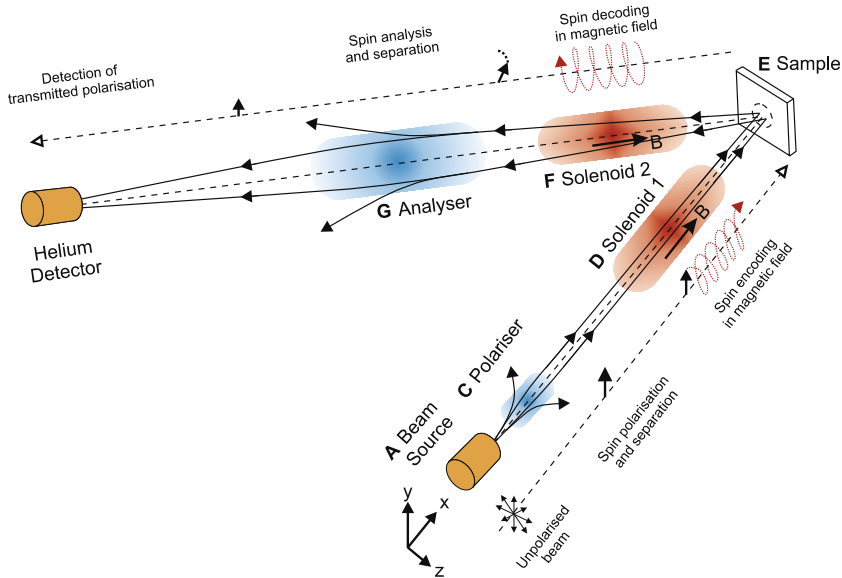
Fig. 4. Classical schematic representation of the spin-echo technique. An unpolarised helium-3 beam is first produced in beam source, **A**, before being passed through the nuclear spin polariser, **C**. The polarised spins are transferred into the precession solenoid field, **D**, before scattering from the surface, **E**. Some of the scattered atoms pass through an identical, but reversed field, **F**, before being spin-analysed, **G**, and counted in the detector, to provide a beam averaged polarisation measurement, following [78].

encoded beam is then incident on a sample surface, **E**, from which it scatters. Providing the form factor can be ignored, as is usually the case for QHAS measurements, the distribution of scattered atoms is given by the dynamic structure factor, $S(\Delta\mathbf{K}, \Delta\omega)$. Some of the scattered atoms pass through the second beamline and therefore through a second precession field, **F**, before entering a spin-analyser, **G**. The analyser transmits only a selected polarisation into the detector, usually the cosine or 'x' component, corresponding to the analyser being aligned with the polariser.

The total spin precession angle accumulated as a helium atom passes through either of the precession fields is simply a result of the total time, T, the helium atom spends within the precession field of length, L, and the magnetic field integral it consequently experiences, which is given by

$$\phi = \gamma \int_0^T B dt = \frac{\gamma}{v} \int_0^L B dl, \tag{10}$$

where v refers to the velocity of atoms as they pass through either coil. The total phase accumulated for helium atoms which sequentially pass through both precession fields is then given by

$$\phi = \phi_1 + \phi_2 = \frac{\gamma}{v_1} \int_0^L B_1 dl + \frac{\gamma}{v_2} \int_0^L B_2 dl. \tag{11}$$

If the fields are equal and opposite, which is the usual condition for 'standard' spin-echo experiments, we can simplify this expression to give

$$\phi = \gamma \left(\frac{1}{v_1} - \frac{1}{v_2} \right) \int_0^L B dl \approx \gamma \frac{(v_2 - v_1)}{v_1^2} \int_0^L B dl, \tag{12}$$

which is valid when the changes in velocity are small. Since the energy change for a single helium atom is also given by $\hbar\Delta\omega = \frac{1}{2}mv_2^2 - \frac{1}{2}mv_1^2 \approx mv_1(v_2 - v_1)$ we obtain

$$\phi = \frac{\gamma}{mv^3} \hbar\Delta\omega \int_0^L B dl, \tag{13}$$

where we now take v to be the mean velocity of atoms in the beam, which indicates that ϕ provides a first order approximation to the energy change experienced by an individual helium atom. Real measurements average over the distribution of energies in the scattered beam. A measurement of beam averaged polarisation is obtained by passing the beam through the analyser, described above, which transmits atoms according to the cosine of their classical spin-phase, with respect to the original polarisation direction. The beam averaged polarisation, P_x, is therefore given by the beam average,

$$P_x = \langle \cos \phi \rangle. \tag{14}$$

Since the distribution of atoms in the scattered beam is given by the dynamic structure factor, $S(\Delta\mathbf{K}, \Delta\omega)$, the beam average can be expressed in terms of a cosine Fourier transform,

$$P_x = \frac{\int S(\Delta\mathbf{K}, \Delta\omega) \cos (\Delta\omega t) d\Delta\omega}{\int S(\Delta\mathbf{K}, \Delta\omega) d\Delta\omega} = \frac{Re[I(\Delta\mathbf{K}, t)]}{S(\Delta\mathbf{K})} = Re\left[\frac{I(\Delta\mathbf{K}, t)}{I(\Delta\mathbf{K}, 0)}\right], \tag{15}$$

where $I(\Delta\mathbf{K}, t)$ is the intermediate scattering function described earlier and the quantity, t, usually referred to as the 'spin-echo time', is given by

$$t = t_{SE} = \frac{\gamma\hbar}{mv^3} \int_0^L B dl. \tag{16}$$

A similar argument shows that measurement of the orthogonal polarisation, $P_y = \langle \sin \phi \rangle$, corresponds to the imaginary part of the normalised ISF, $P_y = Im[I(\Delta\mathbf{K}, t)/I(\Delta\mathbf{K}, 0)]$.

Providing the energy changes introduced during scattering are small compared to the mean energy of the helium atoms, measurement of both polarisation components provides the normalised intermediate scattering function in full. At this point, we limit ourselves to pointing out that since $I(\Delta\mathbf{K}, t)$ is the Fourier transform of the pair correlation function, $G(\mathbf{R}, t)$, the measurement provides a complete statistical description of surface motion, as seen by the helium beam. In Section 5 below we describe the interpretation of $I(\Delta\mathbf{K}, t)$ to understand the nature of the surface motion.

It is not essential to measure both P_x and P_y in every experiment. A measurement of P_x alone gives the real part of $I(\Delta\mathbf{K}, t)$. If, for example, the imaginary part is taken to be zero for all t, then Fourier transformation will force the dynamical structure factor, $S(\Delta\mathbf{K}, \Delta\omega)$, to be symmetric about zero energy transfer, i.e. identical energy losses and gains will be produced by the transform, providing the energy exchanges are small. In the case of aperiodic motion of adsorbates, $G(\mathbf{R}, t)$ is expected to be a symmetric function so that it can be reconstructed accurately from the real part of the classical ISF and it is, therefore, reasonable to use measurements of P_x alone. Other inelastic processes, such as phonon creation and annihilation, will generally correspond to an asymmetric form for the dynamical structure factor, so that measurements of both components of the polarisation are necessary. In fact, in a helium spin-echo experiment, both the cosine and sine terms may be measured [78,105], enabling Eq. (15) to be converted to a complete, complex, Fourier transform, and an asymmetric energy transfer spectrum to be constructed. There are three approaches which can be used to obtain the sine term:

- either one of the polariser or analyser assemblies can be rotated through and angle of $\pi/2$ with respect to the other;
- an additional switchable guide field between the analyser and the first precession coil can be used to rotate the initial polarisation by $\pi/2$, before precession begins;
- an extra $\pi/2$ rotation can be added in the first precession coil.

The latter has the advantage of being simplest to implement, but the precise rotation angle is affected by the beam energy and spread. Fortunately, for a beam with a reasonably narrow energy spread the correct angle can be achieved to an acceptable precision, and consequently this technique has been used in the Cambridge apparatus, e.g. in [78,105].

3.2. Semi-classical description

The semi-classical approach, described by Gähler et al. [103], gives a useful alternative, which provides additional physical insight into the spin-echo process. We consider the beam to be produced and polarised exactly as before, which corresponds to preparing the helium atoms in the $|+\rangle_x$ spin state. As the helium atoms enter the precession solenoids, the spin must align parallel or anti-parallel to the magnetic field. The existing helium wavepacket can be therefore be represented as a superposition of the two $|\pm\rangle_z$ spin eigenstates, parallel and anti-parallel to the z-aligned field, given by,

$$|+\rangle_x = \frac{1}{\sqrt{2}}\left(|+\rangle_z + |-\rangle_z\right). \tag{17}$$

The magnetic field splits the energies of these two components, which become $mv^2/2 \pm \mu B$, respectively, as can be shown from energy conservation. Inside the magnetic field, the velocities of the two states are given by $v_\pm = v \pm \mu B/mv$, so one component, which is aligned with the field is accelerated while the other component, which is anti-parallel, slows down. Consequently, the two components take different lengths of time, $t_\pm$, to traverse the solenoid field, given by

$$t_\pm = \frac{\int_0^L dl}{v} \pm \frac{\mu}{mv^3}\int_0^L B\,dl, \tag{18}$$

and results in the two wavepackets components separating before they reach the sample. Writing μ in terms of the ^{3}He spin and gyromagnetic ratio, $\gamma\hbar/2$, shows this time difference is exactly the same spin-echo time as in Eq. (16),

$$t_{SE} = t_+ - t_- = \frac{\gamma\hbar}{mv^3}\int_0^L B\,dl, \tag{19}$$

except this time we may associate it with a physical attribute of the system: the temporal separation of the two spin-components as they reach the sample. Atoms scattered with a particular $\Delta\mathbf{K}$ (i.e. having a particular scattering angle) pass down the second arm of the machine, where the spin-components are recombined in space and time, interfering, before reaching the detector. If the surface does not change during t_{SE}, both wavepacket components scatter identically. If the second solenoid field has an identical magnitude but opposite direction, then by the end of the field the two wavepackets will be recombined to regenerate their initial spin orientation. However, if the surface changes, due to mobile scattering centres, the two spin-components will be scattered differently and the recombined wavepacket will not have the same final spin-state, leading to a measurable loss in polarisation that corresponds to the loss in correlation of the surface.

The net effect of the spin-echo experiment is to prepare two coherent wave packets which are separated in time, scatter from the sample, and are then recombined. It is the re-combination of the time-separated wavepackets which gives the technique its sensitivity to correlations in the surface configuration. We show this by writing the scattered amplitude in terms of a position function for j kinematic scattering centres on the surface (with identical form factors),

$$A(\Delta\mathbf{K}, t, t_{SE}) \propto \sum_j \exp\left(i\Delta\mathbf{K} \cdot \mathbf{R}_j(t)\right) + \exp\left(i\Delta\mathbf{K} \cdot \mathbf{R}_j(t + t_{SE})\right). \tag{20}$$

It is convenient to write

$$\exp\left(i\Delta\mathbf{K} \cdot \mathbf{R}_j(t)\right) = \int \delta(\mathbf{R} - \mathbf{R}_j(t)) \exp\left(i\Delta\mathbf{K} \cdot \mathbf{R}(t)\right) d\mathbf{R}, \tag{21}$$

and to define a position function, $P(\mathbf{R}, t) = \sum_j \delta(\mathbf{R} - \mathbf{R}_j(t))$. Hence, we have,

$$A(\Delta\mathbf{K}, t, t_{SE}) \propto \int [P(\mathbf{R}, t) + P(\mathbf{R}, t + t_{SE})]e^{i\Delta\mathbf{K}\cdot\mathbf{R}} d\mathbf{R}, \tag{22}$$

where the integration limits are $\pm\infty$. These gives the scattered intensity at a particular time as

$$I(\Delta\mathbf{K}, t, t_{SE}) \propto AA^*$$

$$\propto \iint [P(\mathbf{R}_1, t) + P(\mathbf{R}_1, t + t_{SE})][P(\mathbf{R}_2, t) + P(\mathbf{R}_2, t + t_{SE})]e^{i\Delta\mathbf{K}\cdot(\mathbf{R}_2 - \mathbf{R}_1)}d\mathbf{R}_1 d\mathbf{R}_2. \tag{23}$$

Rewriting $\mathbf{R} = \mathbf{R}_2 - \mathbf{R}_1$ gives

$$I(\Delta\mathbf{K}, t, t_{SE}) \propto \iint [P(\mathbf{R}_1, t) + P(\mathbf{R}_1, t + t_{SE})][P(\mathbf{R}_1 + \mathbf{R}, t) + P(\mathbf{R}_1 + \mathbf{R}, t + t_{SE})]d\mathbf{R}_1 e^{i\Delta\mathbf{K}\cdot\mathbf{R}}d\mathbf{R}, \tag{24}$$

which is the Fourier transform with respect to $\mathbf{R}$ of

$$\int P(\mathbf{R}_1, t)P(\mathbf{R}_1 + \mathbf{R}, t)d\mathbf{R}_1 + \int P(\mathbf{R}_1, t)P(\mathbf{R}_1 + \mathbf{R}, t + t_{SE})d\mathbf{R}_1$$

$$+ \int P(\mathbf{R}_1, t + t_{SE})P(\mathbf{R}_1 + \mathbf{R}, t)d\mathbf{R}_1 + \int P(\mathbf{R}_1, t + t_{SE})P(\mathbf{R}_1 + \mathbf{R}, t + t_{SE})d\mathbf{R}_1. \tag{25}$$

The first and fourth terms are proportional to $G(\mathbf{R}, 0)$, the static pair correlation function, which is usually written as $g(\mathbf{R})$. The second term, when evaluated and averaged over time gives a result proportional to $G(\mathbf{R}, t_{SE})$. The third term is proportional to $G(\mathbf{R}, -t_{SE})$, which providing the particles have no 'memory' of where they have been is equal to $G(\mathbf{R}, t_{SE})$. A beam averaged measurement of intensity at the in-phase condition, where the recombined wavepackets interfere constructively, is therefore proportional to the spatial Fourier transform of $g(\mathbf{R}) + G(\mathbf{R}, t_{SE})$,

$$I_{max}(\Delta\mathbf{K}, t_{SE}) \propto \int [g(\mathbf{R}) + G(\mathbf{R}, t_{SE})]\exp(i\Delta\mathbf{K}\cdot\mathbf{R})d\mathbf{R}. \tag{26}$$

Intensities are the observable quantity in a spin-echo experiment, although the corresponding polarisation, $P(\Delta\mathbf{K}, t)$, is usually presented. As usual, polarisation is given by

$$P = \frac{I_{max} - I_{min}}{I_{max} + I_{min}}, \tag{27}$$

so in order to calculate the polarisation, we also require the minimum intensity, I_{min}, at the out of phase condition, which corresponds to switching the plus in Eq. (22) between P terms, to a minus. When followed through, this gives an intensity proportional to the Fourier transform of $g(\mathbf{R}) - G(\mathbf{R}, t_{SE})$ and an equivalent form for Eq. (26). Substituting into (27) we find the measured polarisation is then given by the normalised Fourier transform of $G(\mathbf{R}, t_{SE})$,

$$P(\Delta\mathbf{K}, t_{SE}) = \frac{\int G(\mathbf{R}, t_{SE})e^{i\mathbf{K}\cdot\mathbf{R}}d\mathbf{R}}{\int G(\mathbf{R}, \mathbf{0})e^{i\mathbf{K}\cdot\mathbf{R}}d\mathbf{R}} = \frac{I(\Delta\mathbf{K}, t_{SE})}{I(\Delta\mathbf{K}, 0)}, \tag{28}$$

which is the familiar intermediate scattering function.

The semi-classical approach, which demonstrates the relation between the correlation of the surface and the spin-dynamics of the helium atoms, provides considerably greater insights into the spin-echo experiment than the traditional classical derivation. A fully quantum approach has been described [103] but it gives few additional insights.

3.3. 2D matrix representation and tilted projection measurements

The analysis described in Section 3.1 shows that in the limit of small energy changes, a polarisation measurement at the elastic spin-echo point (when $\int_0^L B_1 dl = -\int_0^L B_2 dl$, or equivalently when $d\phi/d\nu = 0$ for the range of velocities, ν, in the beam) provides $I(\Delta\mathbf{K}, t)$. Conversely, when ΔE is comparable with $E_0, P(\Delta\mathbf{K}, t)$ is not directly proportional to $I(\Delta\mathbf{K}, t)$. It is then necessary to take into account that strictly, P is related to the dynamic structure factor, S, by a Fourier transform between complimentary variables of spin-echo time, t, and the de Broglie wavelength, λ. In general, to obtain $S(\Delta\mathbf{K}, \Delta\omega)$ from $P(\Delta\mathbf{K}, t)$ we then require a Fourier transform, followed by a non-linear scaling to covert wavelength to energy [78]. Finally, if required, $S(\Delta\mathbf{K}, \Delta\omega)$ can be transformed to obtain the true form for $I(\Delta\mathbf{K}, t)$. If the field in only one of the precession solenoids is varied, a similar procedure can be applied to reconstruct the absolute distribution of energies in the scattered beam in a process rather like

Fourier transform spectroscopy. Such measurements form the basis of the selective adsorption resonance data described in Section 7.1 below.

Alexandrowicz et al. recently presented a representation of the spin-echo technique which enables a wide range of experiments to be treated within the same framework [104,78]. The idea is to represent the spin-echo process as a double Fourier transform, using a transfer matrix which maps intensity from the incoming beam to the outgoing beam. The matrix provides a visual representation of the different classes of experiment which can be performed.

For convenience, the accumulated phase in either solenoid can be written in terms of wavelength,

$$\phi = \frac{\gamma m \lambda}{2\pi h} \int_0^L B dl = C \lambda I, \tag{29}$$

where a number of parameters are absorbed into the constant, $C = \gamma m B_{eff}/2\pi h$, where the magnetic field integral is replaced by an effective field per unit current, $B_{eff} = \int_0^L B dl/I$. λ and I form a true Fourier transform pair, along with the constant C. For a single coil, the measured polarisation is then given by

$$P(I) = P_x(I) + iP_y(I) = \int \rho(\lambda)[\cos(2\pi C\lambda I) + i\sin(2\pi C\lambda I)]d\lambda, \tag{30}$$

where $\rho(\lambda)$ is the wavelength distribution of the helium atoms as they pass through the solenoid. Using both coils, the total accumulated phase is still $\phi_1 + \phi_2$ as before, so if both real and imaginary parts of the polarisation can be measured, the polarisation, P, can be generalised to a 2D Fourier transform,

$$P(I_1, I_2) \propto \iint I(\lambda_1, \lambda_2) \exp(2\pi i C\lambda_1 I_1 + 2\pi i C\lambda_2 I_2) d\lambda_1 d\lambda_2, \tag{31}$$

where $I(\lambda_1, \lambda_2)$ is a matrix that represents the relative intensity of the beam that has a wavelength of λ_1 in the first arm and λ_2 in the second, and for convenience, we take both coils to be identical. The wavelength intensity matrix $I(\lambda_1, \lambda_2)$ can be treated as the product of the wavelength distribution in the incident beam, $\rho(\lambda_1)$, and a wavelength mapping $S(\lambda_1 \rightarrow \lambda_2)$, describing the probability of changing the wavelength from one value to another during scattering.

In principle the matrix $I(\lambda_1, \lambda_2)$ contains information about all the possible energy transfer processes that are 'illuminated' by the wavelengths in the incident beam. The underlying physical processes, such as the width (or lifetime) of a particular excitation, can be obtained by examining the shape and width of the features in the matrix. These are equivalent to the position, shape and width of features in $S(\Delta\mathbf{K}, \Delta\omega)$, that can be obtained from time-of-flight experiments, but without the effect of the instrumental resolution. In fact, the wavelength intensity matrix contains much more information than $S(\Delta\mathbf{K}, \Delta\omega)$, which implicitly assumes that only energy transfers are important, regardless of incident energy. As an illustration, a simple $I(\lambda_1, \lambda_2)$ matrix is shown in Fig. 5 along with several different possible measurements. There are several high intensity lines present in the matrix. The elastic peak shows up as a delta function at $\lambda_1 = \lambda_2$. Any diffusion induced quasi-elastic broadening of the elastic peak shows up as a width of the $\lambda_1 = \lambda_2$ line. Inelastic modes, corresponding to finite energy transfers appear above or below $\lambda_1 = \lambda_2$, and also have an associated width.

In principle, measuring $P(I_1, I_2)$ for a range of both I_1 and I_2 and Fourier transforming provides a measurement of $I(\lambda_1, \lambda_2)$, and hence complete information about all of the dynamical processes present. However, the two-dimensional nature of $I(\lambda_1, \lambda_2)$ and the need to reconstruct it with sufficient resolution requires exceptionally high signal to noise, or alternatively very long acquisition times. To date, such a measurement has not been reported. Instead, it is usual to make use of the Fourier projection theorem, which states: a measurement along a particular line in $P(I_1, I_2)$ space corresponds to the Fourier transform of the projection of the entire $I(\lambda_1, \lambda_2)$ matrix onto the equivalent line through $I(\lambda_1, \lambda_2)$ space [78]. The projections **A**–**D** in Fig. 5 illustrate how this principle may be used to examine the features of the various modes.

The simplest measurements are the projections labeled **A** and **B** in Fig. 5. These correspond to polarisation measurements along the $I_2 = 0$ and $I_1 = 0$ lines through $P(I_1, I_2)$, i.e. varying the current in only one of the solenoids. By looking at the projection of the wavelength intensity matrix onto these
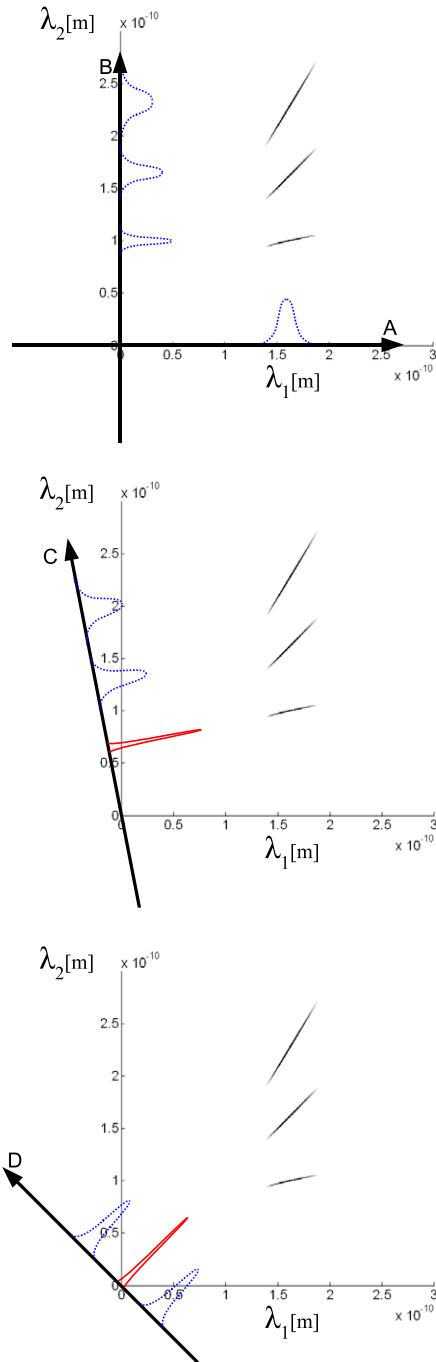
Fig. 5. Illustration of a simple wavelength transfer matrix, $I(\lambda_1, \lambda_2)$ and several projected measurements, reproduced from [78]. The same transfer matrix is shown in all three panels and includes quasi-elastic intensity, plus distinct energy-gain and energy-loss inelastic modes. projections **A–D** show a number of different measurements, optimised to obtain different characteristics of the wavelength transfer matrix.

Table 1
Summary of features of different tilted projection spin-echo measurements.

Measurement type	Tilt angle	Rejection of beam velocity spread	Additional notes
Quasi-elastic optimised	135°	Complete	Equal and opposite currents: the 'standard' spin-echo experiment
Elastic optimised	0°, 90°	None	Current in one coil only
Inelastic optimised	Any	Partial	Current in both coils in fixed ratio

lines, we see the effect of such measurements. As indicated by the dotted blue lines[1], projection **A** yields the initial velocity distribution in the incident beam, whereas projection **B** yields the velocity distribution in the scattered beam. The information obtained using projection **B** is directly comparable to and is limited in the same way as a time-of-flight experiment. However, it is also possible to scan along any other line through $P(I_1, I_2)$ and the benefits of being able to do so should now be evident. In order to measure the fundamental linewidths, the projection can be adjusted to suit the feature concerned. For example, projection **C** is adjusted to provide a measurement of the width of an energy gain peak, while projection **D** is adjusted to measure the (quasi-) elastic peak width, using an $I_2 = -I_1$ measurement.

In general, most lines in $I(\lambda_1, \lambda_2)$ are curved, including those corresponding to dispersionless modes at finite energy transfer. Only the elastic peak follows a straight line, which explains why a conventional spin-echo measurement with $I_2 = -I_1$, is independent, to first order, of the spread in λ_1. The curvature of features also means that no single projection provides an optimum measurement of all excitations. In particular, a quasi-elastic measurement, such as projection **D**, yields the true quasi-elastic linewidth, but will overestimate the width of the inelastic modes. In general, the optimum tilt angle, α, is given by [78],

$$\frac{d\lambda_2}{d\lambda_1} = -\tan\alpha = -\frac{I_1}{I_2}. \tag{32}$$

The location of any particular feature in the projected measurement varies according to the projection angle used. The apparent wavelength at which features appear, λ_{exp}, may be converted to the true outgoing wavelengths, λ_{abs}, using the following scaling and shift [104],

$$\lambda_{abs} = \frac{\lambda_{exp}}{\cos\left(\alpha - \frac{\pi}{2}\right)} + \langle\lambda_1\rangle \tan\left(\frac{\pi}{2} - \alpha\right). \tag{33}$$

We should also point out that the resolution of any measurement is uniform in wavelength space, so varies non-linearly with energy transfer. Quasi-elastic measurements ($\alpha = 135°$) are limited only by the maximum field strength that can be applied, whereas for finite energy transfer processes there are a number of additional broadening processes [104,78], even for measurements at an optimal tilt angle. These originate in the curvature of the features in $I(\lambda_1, \lambda_2)$ and the finite angular resolution of any real spectrometer. Finally, the concept of a spin-echo time only makes sense in the context of standard, $\alpha = 135°$, measurements. A summary of the three distinct classes of tilted projection measurements is given in Table 1.

4. Experimental implementation

At present, there are two published implementations of the helium spin-echo technique, by groups in Heidelberg and Cambridge, although there is an additional mention of a project in Berlin [106] and another instrument is presently being developed in Israel. The first implementation, by the DeKieviet group in Heidelberg, was published in 1995 [100]. This pioneering work demonstrated the concept and established helium-3 spin-echo as a viable surface analogue to neutron spin-echo. This first work

---

[1] For interpretation of colour in Fig. 5, the reader is referred to the web version of this article.

demonstrated measurement of neV level energy changes in the gravitational potential of a beam of atoms traveling up a 10% incline. The work was shortly followed by application of the HeSE technique to surface science [101], measuring quasi-elastic energy changes occurring due to dynamics on a quartz surface, described in more detail below.

As a scattering technique, ideally ^{3}HeSE measurements would be made over a large range of Fourier times and over a wide range of momentum transfer values. However, in the spin-echo experiment the beam requirements for these two conditions are mutually incompatible. For large Fourier times (corresponding to high energy resolution), a slow beam is required to facilitate magnetic manipulation, whereas for large momentum transfer (high spatial resolution) a fast beam with considerable momentum is required. The Heidelberg apparatus operates at a very low beam energy, achieving exceptionally high energy resolution (see Table 2), with variable scattering geometry and is well suited to very 'slow', long length-scale surface processes [100], rather like recent cold neutron spin-echo spectrometers. In contrast, the Cambridge apparatus operates at a much higher beam energy in order to provide more momentum in the beam and allow measurements on much smaller scales. The Cambridge instrument uses a fixed 45° scattering geometry and a nominal beam energy of 8 meV, with the aim of permitting measurements up to about $\Delta\mathbf{K} = 4$ Å^{-1}.

Fig. 6 shows a top down schematic of the Cambridge apparatus, illustrating the general layout. The instrument follows the schematic given in Fig. 4 quite closely. After the beam is produced in the source (which includes recycling of the helium-3 gas which does not go into the final beam) the beam is directed onto the sample, via. the required magnetic fields. Atoms scatter diffusely in all directions, and some pass through the second arm of the machine, and the magnetic fields there, to reach the detector. The entire beamline is maintained at high vacuum to avoid attenuation of the helium beam, but only the sample chamber and detector require ultra high vacuum levels.

4.1. Magnetic components

In order to implement the spin-echo method described above, the key magnetic components are the nuclear spin-polariser and spin-analyser, the precession solenoids, and the transition fields between them. Several magnetic components have been described in some detail, which we review here.

4.1.1. Polariser and analyser

Although other methods are possible, nuclear spin polarisation and analysis of helium-3 beams have been achieved in spin-echo experiments using strong inhomogeneous magnetic fields. The magnetic field, $\mathbf{B}$, produces a force on the nuclear spin, given by $\mathbf{F} = \pm\mu\nabla|\mathbf{B}|$, where μ is the nuclear magnetic dipole moment. As the beam is passed through the field, the opposite forces separate the two spin-components spatially and one may be removed before the beam atoms reach the sample. Although quadrupole magnets have been used [101], hexapole magnets (also referred to as sextupole magnets) are the preferred option for this purpose [108,109,101] as the linear field gradient also gives rise to true geometric focusing of the helium-3 beam, enabling the intensity of the beam to be improved significantly. On leaving the hexapole, the nuclear spins are polarised with respect to the local

Table 2
Comparison of parameters for the Heidelberg and Cambridge helium-3 spin-echo implementations. Parameters for the instruments are taken from the information in [100,101] and [107], respectively; the respective sets of values are illustrative and other nozzle temperatures can be used.

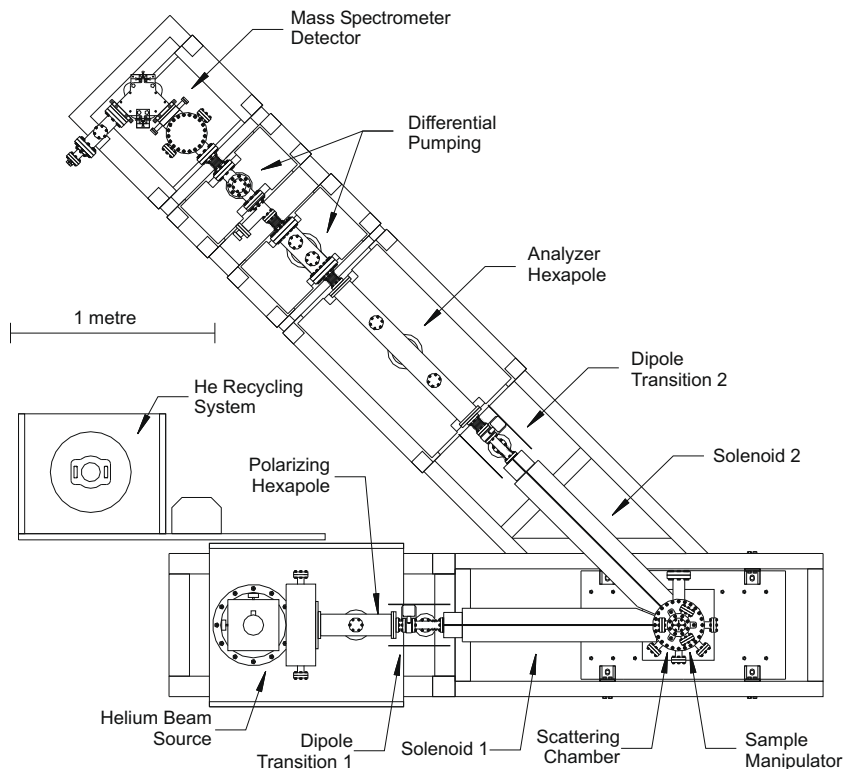| Parameters	Heidelberg		Cambridge	
Typical nozzle temperatures (K)	1	4.2	37	56
Beam energy (meV)	0.22	0.9	8.0	12.0
Beam wavevector (Å^{-1})	0.56	1.1	3.4	4.2
Maximum $\Delta\mathbf{K}$ (Å^{-1})	~0.56	~1.1	~5.8	~7.1
Total scattering angle (°)	90–180 variable		44.4 fixed	
Fourier time	–	>12 ns	680 ps	370 ps
Energy resolution (spectrum reconstruction)	–	< 0.2 µeV	3 µeV	6 µeV

Fig. 6. Top down view of the Cambridge spin-echo apparatus. The helium beam is produced in the beam source (bottom left) and directed through the polariser and incoming solenoid to the sample chamber (bottom right). Part of the scattered beam is selected and passes through the outgoing solenoid and nuclear spin analyser to the detector, reprinted with permission from Rev. Sci. Inst. 76, 053109 (2005), copyright 2005, American Institute of Physics.

field. The hexapole is usually followed by an additional dipole to orient the spins in a uniform direction in the lab frame.

In order to focus a helium-3 beam of energy $\sim$10 meV, typically pole-piece fields of up to $\sim$1 T are required, extending over a length of a few tens of centimetres. Such strong fields are difficult to achieve, but a number of approaches have been described. In the last 10 years there has been a notable emphasis on focusing neutron beams. For helium-3 focusing the most important classes of design are soft iron pole-pieces surrounding the beam, as used by Steinhof [106], and the segmented multi-pole proposed by Halbach [110], where typically 18 or 24 segments of permanent magnetic material, of rotating orientation are used to generate the hexapole field. The description of the Steinhof magnet [106] refers to helium-3 focusing, but only presents detailed measurements for neutrons. However, the polariser and analyser used in the Cambridge apparatus have been described in some detail [108,109]. These both use permanent magnets, as shown in Fig. 7.

The Cambridge polariser is used to focus and polarise the diverging helium beam to a 2 mm diameter parallel beam, directed onto the sample. The assembly is 300 mm long, has a 2 mm diameter bore and the pole-piece field is 1.1 T. The main requirement is for the polariser to operate correctly on a high intensity beam, which means that the defocused atoms (which hit the internal walls of the magnet and form background gas) must be conducted away from the beamline to prevent catastrophic attenuation of the beam. The gaps between the polepieces are adjusted to give sufficient gas conductance. Within these limits, the pole-piece shape and yoke are adjusted to give a strong field with small aberrations [108]. The analyser hexapole is positioned along the second arm of the instrument and focused one polarisation of atoms from an effective source on the sample, to an image at the detector. It
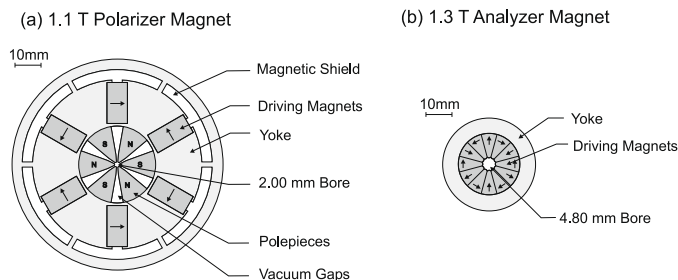
(a) 1.1 T Polarizer Magnet   (b) 1.3 T Analyzer Magnet

Fig. 7. Comparison of two types of hexapole magnet used for the nuclear spin polariser and analyser in the Cambridge HeSE apparatus. (a) Shows the polariser magnet developed for use with high intensity atomic beams, including vacuum pumping gaps between the pole-pieces to allow the defocused gas to escape. (b) Shows the optimised Halbach type magnet used for the spin-analyser, where the scattered beam intensity is much lower. Here, the segment shape is adjusted to minimise hexapole field aberrations, reprinted with permission from Rev. Sci. Inst. 76, 053109 (2005), copyright 2005, American Institute of Physics.

experiences a helium flux several orders of magnitude lower than the polariser. It is therefore possible to use a Halbach type device, without pumping gaps, which can achieve fields that are ~20% stronger. Stronger fields enable a larger bore with same optical properties, improving the signal transferred to the detector. In the Cambridge analyser an optimised segment shape was used to minimises multi-pole field aberrations [109]. The resulting device is 800 mm long, has a bore of 4.8 mm and gives pole-piece fields of 1.3 T.

Both these Cambridge magnets are used in vacuo, unlike for example the Steinhof design, where a small internal vacuum tube is used. In the Cambridge design the pole-pieces can be brought closer to the helium beam, but the background pressure is limited to sub-UHV, meaning further differential pumping is required between the hexapole and sample or detector chambers. To avoid introducing additional aberrations in the magneto-optical properties of the field a manufacturing precision of ~10 μm or better is required [108].

4.1.2. Precession solenoids

In current HeSE experiments, the variable strength precession magnetic fields are produced using conventional conductor solenoid-like windings [101,107]. In any such devices there are precession aberrations, corresponding to different atoms experiencing different magnetic field integrals. These aberrations come from two sources, different length trajectories due to different angular trajectories through the finite sized beam and the unavoidable divergence of the B field with increasing radius. For the same field integral, long solenoids give better aberration characteristics than short solenoids. Zeyen and Rem showed that the optimal field takes a sinusoidal form [111], and both the Heidelberg and Cambridge instruments use this form, as illustrated schematically in Fig. 8. Most neutron spin-echo instruments also use conventional windings, but the larger beam diameter (typically around 40 mm) means substantially larger assemblies are necessary, with more severe aberrations. NSE instruments typically use simple rectangular solenoid fields with additional aberration correction coils, rather than the optimal field shape.

The ultimate resolution in a given instrument is determined by both the maximum magnetic field integrals and the field aberrations, which give an intrinsic depolarisation of the beam that must also be accounted for. The Cambridge instrument shows no drop in intrinsic polarisation at full current (when limited by power dissipation in the windings), indicating stronger coils and more severe aberrations could be accepted, if higher currents were tolerable. The HeSE coils are surrounded by several layers of mu-metal shielding (see Fig. 8), enabling the same coils to be used to zero current, unlike most neutron spin-echo implementations. The precession field integrals are the only parameters necessary to calibrate the instrument, and these can easily be obtained to high precision either by calculation, based on the coil design, or experimentally, by calibration using a monochromating crystal such as LiF [107].
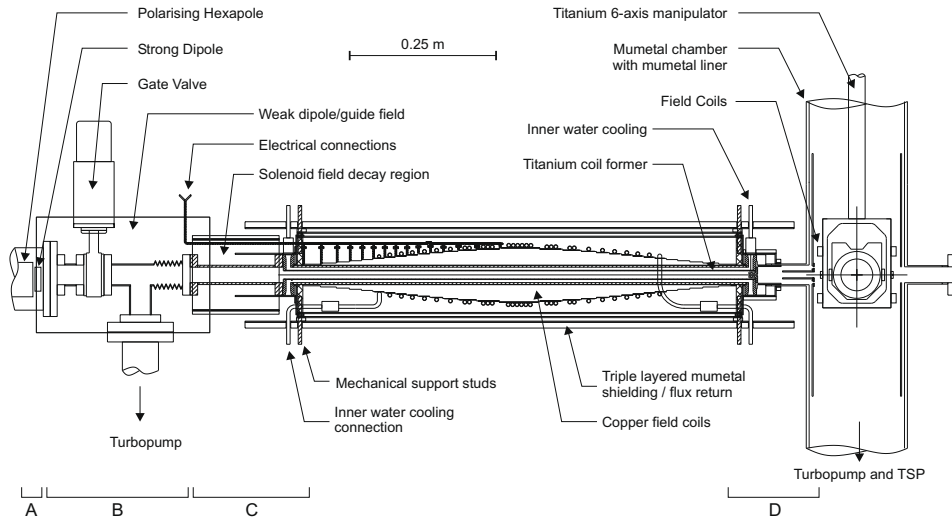
Fig. 8. Schematic of the Cambridge helium spin-echo solenoid assembly and magnetic shielding, plus transition regions between the polariser and sample chamber. **A** indicates the end of the polariser assembly. **B** is a weak dipole guide field though a gate valve and pumping assembly. **C** shows the transition region between the dipole and solenoid fields, and **D** the transition region between the solenoid and sample chamber, reprinted with permission from Rev. Sci. Inst. 76, 053109 (2005), copyright 2005, American Institute of Physics.

4.1.3. Transition regions

Correct design of the transitions between the magnetic elements is crucial to avoid loss of polarisation. The key concept is the 'rate' of a magnetic transition, as defined by the apparent the rate of change of the field orientation compared to the Larmor precession rate for ^{3}He, $\omega_L = \gamma B$, where $\gamma/2\pi = 32.43$ MHz/T. Transitions between the polariser and dipole stage must be 'slow'; the rate of precession must be much faster than the rate of change of field direction, such that precession allows the polarised spins to follow the field orientation. The condition has been achieved by maintaining strong fields throughout the transition region [100,107]. Between the dipole and precession coils the polarised spins must not follow the changing field direction. These 'fast' transitions have been achieved by reducing the field level to approximately zero before the orientation of the magnetic field changes. In the Heidelberg apparatus, the fast transition is achieved through the use of long regions of tubular mu-metal magnetic shielding, into which the magnetic field decays exponentially [100]. The Cambridge apparatus uses a more complex shielding geometry, illustrated in Fig. 8, which increases the rate of field decay, in order to reduce the overall length of the beamlines and subsequent $1/r^2$ loss in scattered intensity [107]. The main disadvantage with this approach is that significantly stronger magnetic fields are liable to saturate the mu-metal and limit the applicability of this scheme where larger magnetic fields are required.

4.2. Additional novel instrumentation

4.2.1. Recycling ^{3}He beam source

Since the spin-echo experiment does not require a highly monochromatic beam, the primary requirements on the source are high intensity, stability at low temperature and good reliability. Given current prices, at a typical flow rate of 10 mbar l/s helium-3 flows through the nozzle at a rate of more than \$3 per second, yet only a tiny fraction constitutes the final beam. It is therefore economically vital to recycle gas flowing through the nozzle, which makes the beam-source gas handling significantly more complex than usual. The Cambridge beam-source is described in [107], and recent changes are given in [112], which improve the reliability and continuous recycler throughput, hence the useful intensity of the beam. Hedgeland et al. also describe and model measurements of anomalous

attenuation effects seen in these very low energy helium beams [113], originating from direct back-scattering of atoms into the free jet expansion (as opposed to atoms from the background chamber gas). They suggest a skimmer geometry which may enable the intensity of very low energy helium beams to be more than doubled.

4.2.2. Sample manipulator

In the Cambridge apparatus, the sample is mounted on a custom six-axes manipulator, as indicated in Fig. 8. To avoid any possibility of stray fields causing beam depolarisation, all components penetrating the magnetically shielded sample chamber are made from entirely non-magnetic materials; primarily titanium instead of the usual stainless steel. The primary angle of incidence of the beam on the sample, used to control momentum transfer, can be varied continuously through 360°, the azimuthal orientation of the crystal can be varied by 100°, and the tilt angle, which is normally only used for alignment, by nominally ±5° from the in-plane scattering condition. Sample cooling is by liquid nitrogen or helium, giving base temperatures of ~100 K and ~60 K, respectively, while heating is by radiation and electron bombardment using a tungsten filament, permitting temperatures well in excess of 1200 K to be achieved. Together, these allow a wide range of systems to be studied and facilitate a broad variety of in situ cleaning procedures.

4.2.3. Detector

The available intensity almost always limits spin-echo measurements. However, given the proliferation of TOF instruments, most existing helium detectors (usually based on electron impact ionisation [114]) are intended to provide fast temporal resolution, eg. [115–119], which typically limits the beam ionisation efficiency to the region $10^{-4}-10^{-5}$. Since in spin-echo experiments time response faster than ~100 ms is not typically required, different ionisation geometries can be used to increase the detector sensitivity. In 2001, DeKieviet et al. [120] applied the Penning like solenoidal magnetic confinement geometry, more frequently used for ion beam sources, to produce a high efficiency detector aimed specifically at helium-3 spin-echo experiments. They report a sensitivity of 0.22 A/mbar, which corresponded to a beam detection efficiency of >0.007. Detectors using similar ion sources have been tested by Toennies and co-workers [121]. More recently, Alderwick et al. published a detailed analysis of the underlying electron behavior inside solenoidal ion sources, and described several different approaches for electron injection and ion extraction [122].

5. Characterisation of diffusion using helium-3 spin-echo QHAS

The primary aim of the spin-echo technique, and the subject of most experimental work and related analysis to date, is the study of surface diffusion and related phenomena using the QHAS technique. In this section, we aim to describe how measurements of $I(\Delta\mathbf{K}, t)$ have been used to obtain comprehensive information about atomic scale surface dynamical processes.

At stated earlier, the underlying framework for analysis comes from the principles established by Van Hove [85]. In particular, the key is the Fourier relationship in Eq. (8) and the concept of the pair correlation function, $G(\mathbf{R}, t)$ and the intermediate scattering function, $I(\Delta\mathbf{K}, t)$. In general, relating either the pair correlation function or the intermediate scattering function to the usual physical parameters used to described the system, such as the energy barriers to hopping or the shape of the adsorbate–substrate potential, is non-trivial. Since the pair correlation function, $G(\mathbf{R}, t)$, in principle contains a full statistical description of surface dynamics, an appropriate analysis technique would therefore seem to be to obtain a series of measurements of $I(\Delta\mathbf{K}, t)$, which can be Fourier transformed in space to give $G(\mathbf{R}, t)$. However, to perform this inversion we would also need a detailed knowledge of the scattering form factor, as in Eq. (7). Since in general this is not available, we cannot make the inversion. Instead, we can make use of the *shape* of $I(\Delta\mathbf{K}, t)$, or equivalently, the shape of the quasi-elastic broadening of the elastic peak in the dynamic structure factor. The way these shapes vary with momentum transfer, temperature and coverage gives a sensitive measurement of the behavior of physical systems.

Although $G(\mathbf{R}, t)$ may be constructed and Fourier transformed for simple models of diffusion, real systems rarely conform to the ideal (see Section 6) and more sophisticated methods are usually
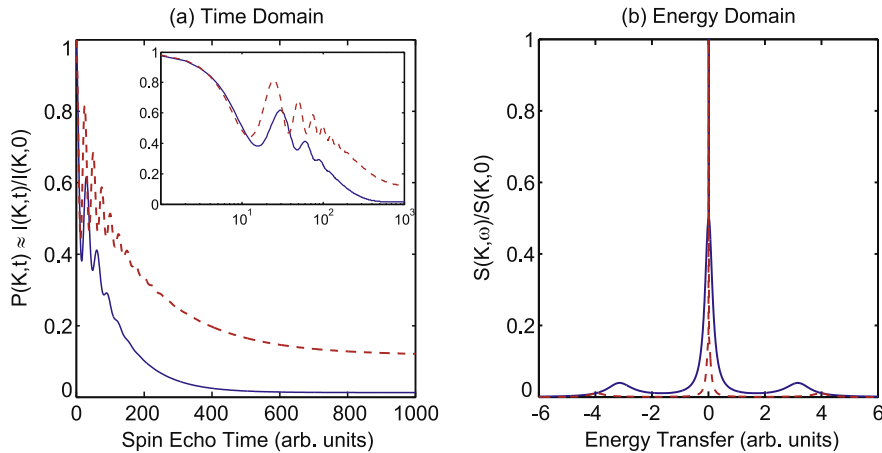
Fig. 9. Example of typical spin-echo data for vibration and diffusion. (a) Illustrates measurements in the time domain, where $I(\Delta \mathbf{K}, t)$ provides a correlation measurement. Periodic motion results in oscillations in $I(\Delta \mathbf{K}, t)$, while aperiodic diffusion gives an overall decay. Elastic scattering from the immobile part of the surface gives rise to a non-decaying background level. Compared to the solid blue line, the dashed red line illustrates to slower diffusion, with a longer lifetime surface vibrational mode and a higher background elastic signal. The inset shows the same data on a log time scale, which is convenient given the dynamic range often measured over. (b) Shows the data converted to the energy domain, where the elastic component shows up as a delta function at zero energy transfer, diffusion gives a quasi-elastic energy broadening around zero, and periodic processes give peaks at finite energy transfer. (For interpretation of the references to colour in this figure legend, the reader is referred to the web version of this article.)

required. The general principle of *experimental* spin-echo/QHAS analysis is to find simple surface dynamical models which reproduce the measurements; for example, a lattice and series of hopping rates, or a 2D Langevin model with a suitably shaped adsorbate–substrate potential energy surface and friction. These simple models can be used as an intermediary, enabling more sophisticated theory (e.g. first principles calculations) to be compared with a simplified, but realistic experimental description of the system.

Fig. 9 schematically illustrates the results of a typical spin-echo QHAS measurement in both the (a) time and (b) energy domain. Providing the energy changes on scattering are small, the time domain measurement of $P(\Delta \mathbf{K}, t)$ for a conventional spin-echo experiment (with a tilted projection angle of 135°, as discussed in Section 3.3) gives a normalised measurement of the intermediate scattering function, $I(\Delta \mathbf{K}, t)$, directly. It is intuitive to treat $I(\Delta \mathbf{K}, t)$ as a surface-structure correlation measurement, as seen by the helium beam, in the direction and on the length-scale given by $\Delta \mathbf{K}$ (the associated length-scale being $2\pi/\Delta \mathbf{K}$, and determined by the scattering geometry of the experiment), and the timescale given by the spin-echo time, t (being controlled by the current in the precession coils). A static surface maintains a perfect correlation with time, so would yield a line at unity. In contrast, if particles on the surface are diffusing, there will be a loss of correlation with time, in the part of the signal coming from the mobile species. The loss leads to an overall decay in the level of $I(\Delta \mathbf{K}, t)$, although it will not decay to zero unless the entire signal comes from mobile species. For simple forms of random motion, such as hopping or Brownian motion (see below), we expect the correlations to decay exponentially, leading to the general form

$$I(\Delta \mathbf{K}, t) = A \exp(-\alpha t), \tag{34}$$

where α is a dephasing rate which characterises the diffusion rate in the measurement. Examining the variation of α with $\Delta \mathbf{K}$ provides a sensitive measurement of the diffusion mechanism, as does its variation with temperature and coverage. Oscillatory surface processes, such as adsorbate vibrations or substrate vibrational modes (phonons), naturally lead to an additional oscillation in the correlation measurement, as shown in Fig. 9a.

Often vibrational modes and diffusion are separated in time, i.e. oscillations have died away before the major diffusional decay, making analysis in the time domain convenient. In fact, since diffusive processes are aperiodic, measurement and analysis in the time domain seems most appropriate. However, in the case of fast diffusion, the two can overlap substantially. Although both forms of the measurement are equivalent, in this case it can be more convenient to treat the data in the energy domain. The energy domain measurement, shown in Fig. 9b, corresponds to the observable quantity in an ideal TOF experiment, and can be obtained by Fourier transforming $I(\Delta\mathbf{K}, t)$ in time.[2] Here, the overall decay corresponds to a quasi-elastic broadening of the zero energy transfer peak, which for random processes is Lorentzian shaped, with FWHM $2\hbar\alpha$. Oscillatory processes correspond to distinct peaks at finite energy transfer.

5.1. General features of QHAS measurements

5.1.1. Scattering correlation effects

For a finite coverage of a diffusing species on a surface, the 2D pair correlation function, $G(\mathbf{R}, t)$, can be written in terms of a self part and a distinct part,

$$G(\mathbf{R}, t) = G_s(\mathbf{R}, t) + G_d(\mathbf{R}, t), \tag{35}$$

which relate to the correlation of either the same particle, or a distinct particle. Through Eq. (8), this leads to the measured intermediate scattering function being the sum of a self and distinct part,

$$I(\Delta\mathbf{K}, t) = I_s(\Delta\mathbf{K}, t) + I_d(\Delta\mathbf{K}, t).$$

Quasi-elastic neutron scattering experiments can sometimes be tuned to select either the complete or self parts, through the use of isotopes which scatter coherently or incoherently, respectively [50]. However, helium scattering is always coherent, so the complete function is always measured and correlation effects will appear if they exist.

In order to estimate the effect of G_d, the distinct part of the correlation function, Frenken and Hinch showed [79] that Vineyard's convolution approximation [123] may be used to express G_d in terms of G_s and the static pair correlation function, $g(\mathbf{R}) = G_d(\mathbf{R}, 0)$,

$$G_d(\mathbf{R}, t) = \int g(\mathbf{R}') G_s(\mathbf{R} - \mathbf{R}', t) d\mathbf{R}',$$

which using the convolution theorem, indicates that $I_d(\Delta\mathbf{K}, t)$ is given by the product of $I_d(\Delta\mathbf{K}, 0)$ and $I_s(\Delta\mathbf{K}, t)$. This yields

$$I(\Delta\mathbf{K}, t) = [1 + I_d(\Delta\mathbf{K}, 0)]I_s(\Delta\mathbf{K}, t) = I(\Delta\mathbf{K}, 0)I_s(\Delta\mathbf{K}, t),$$

or equivalently in the energy domain

$$S(\Delta\mathbf{K}, \Delta\omega) = S_s(\Delta\mathbf{K}, \Delta\omega) + S_d(\Delta\mathbf{K}, \Delta\omega) = S(\Delta\mathbf{K})S_s(\Delta\mathbf{K}, \Delta\omega).$$

In other words, the Vineyard approximation indicates the effect of the coherent summation of scattered amplitude from the distribution of scatterers on the surface is just to scale the overall scattered intensity; there are no further modulations due to interference. The Vineyard approximation is only valid providing interactions between adsorbates are not strong enough to introduce correlations in the motion. Providing this condition is satisfied, the Vineyard convolution approximation allows an analysis of experimental measurements in terms of analytic or numeric models of self-diffusion.

5.1.2. Measurement isotropy

[3]HeSE measurements of $I(\Delta\mathbf{K}, t)$ provide information about the isotropy of diffusion, since $\Delta\mathbf{K}$ corresponds to a particular direction on the surface. Spin-echo QHAS measurements are usually obtained along the principle lattice directions of a given substrate. However, information is only truly

---

[2] As discussed in Section 3.3, $I(\Delta\mathbf{K}, t)$ is only equal to the measured $P(\Delta\mathbf{K}, t)$ in the limit of small energy transfer. For larger energy transfers, the temporal Fourier transform should be made between the measured polarisation and wavelength domain, followed by a non-linear scaling to convert to energy [78].

independent if these directions are orthogonal. On a twofold symmetric substrate, such as a fcc (1 1 0) surface, or a vicinal stepped surface, information can be obtained for diffusion along and perpendicular to the close packed rows or steps. Since ^{3}HeSE measurements are directly sensitive to motion on the atomic length-scale, this provides a novel opportunity to study asymmetric motion in nanostructured systems.

In the case of non-orthogonal azimuths, more care is needed. For example, in the case of a (1 0 0) surface, since the principle directions are only separated by 45°, the $\alpha(\Delta\mathbf{K})$ signature for a measurement along $\langle 1 0 0 \rangle$ will correspond to motion along that direction, plus a the contribution of motion from the two surrounding $\langle 1 0 0 \rangle$ directions, projected onto $\langle 1 0 0 \rangle$. Hence, even if motion is predominately along one principle lattice direction, is will be visible in ^{3}HeSE measurements along both. On hexagonal close packed surfaces, such as an fcc (1 1 1) surface, the problem is exacerbated as the principle axes are only separated by 30°, and so the contributions from several different lattice directions are always important. Anisotropy information can still be extracted, but requires the projections to be included explicitly in either analytic models or numerical calculations [30,124].

5.1.3. Activation energies

A widely used procedure is to assume values of the dephasing rate, α, as a function of temperature, at otherwise constant measurement conditions, follow the Arrhenius form

$$\alpha = \alpha_0 \exp(-E_a/k_B T), \tag{36}$$

from which an activation energy, E_a, can be extracted. Values of E_a provides information about the energy barriers to diffusion and the adsorbate–substrate potential. However, E_a does *not* in general correspond to the true adiabatic energy barrier to diffusion, which is depicted in Fig. 1 [88]. In fact, quite different *effective* QHAS activation energies can be obtained at different values of momentum transfer. As the temperature of a system changes, so does the mechanism underlying the motion. QHAS measurements are generally obtained when species are highly mobile, so the mobile species frequently experience a large proportion of the lateral potential, not just the lowest energy parts. Consequently, small changes in temperature have, through anharmonicity, a significant effect on aspects of the motion, such as the jump length distribution. The implicit assumption of an invariant mechanism underlying the motion may be incorrect so that the use of Eq. (36) to fit data will result in an approximate, or effective, activation energy.

The effective activation barrier is usually lower than the adiabatic barrier and would be lower than a barrier obtained from other experimental techniques (see Section 2.3.3). It is not, however, a difficulty related to the underlying principle of the QHAS technique, but one relating to the degree of sophistication used in interpreting the QHAS data. An accurate way to extract the adiabatic barrier for diffusion is to run molecular dynamics simulations, as discussed in Section 5.4, and optimise the adsorbate–substrate potential to achieve agreement with the experiment [27,30].

The projection of QHAS measurements along adjacent lattice directions (described in Section 5.1.2), means that Arrhenius activation energies obtained along the two principle lattice directions do *not* reflect the isotropy of the barriers of the underlying PES. Instead, Alexandrowicz et al. pointed out that the ratio of the maximum values of the dephasing rate, α, along the two lattice directions would be expected to provide a better estimate [30].

5.1.4. Scattering model limitations

The analysis framework used in the interpretation of spin-echo/QHAS experiments assumes simple kinematic scattering from a series of point scatters. A fully realistic scattering model would also include the effects of the extended, soft, helium-surface interaction, including the possibility of quantum mechanical effects and multiple scattering. Fortunately, the existing evidence is that such corrections play a relatively minor role. Numerical simulations performed using a more sophisticated scattering model showed little effect on the quasi-elastic peak width [125]. Multiple scattering, which might be expected to be important for measurements on the timescales that correspond to the interaction of helium atoms with the surface, also appear to be relatively unimportant. Comparative helium and neutron spin-echo measurements have been made on the benzene/graphite system [87,126] and are in good agreement. Since multiple scattering is unimportant in the neutron scattering

measurements, the results support multiple scattering corrections being relatively unimportant in QHAS.

5.2. Simple QHAS signatures for diffusion

5.2.1. Simple 2D modes of diffusion at low coverage

The simplest form is continuous random motion, or continuous Brownian motion. In this case, we expect the form of $G_s(\mathbf{R}, t)$ to be [79],

$$G_s(\mathbf{R}, t) = \frac{1}{4\pi D|t|} \exp\left(-\frac{R^2}{4D|t|}\right). \tag{37}$$

After Fourier transforming in space, this gives an exponential decay in the time domain,

$$I_s(\Delta\mathbf{K}, t) = \exp(-\Delta K^2 D|t|) \tag{38}$$

of after a further Fourier transform gives a Lorentzian quasi-elastic broadening in the energy domain,

$$S(\Delta\mathbf{K}, \Delta\omega) = \frac{D\Delta\mathbf{K}^2}{\pi(\omega^2 + D^2\Delta\mathbf{K}^2)}. \tag{39}$$

The time domain dephasing rate, $\alpha(\Delta\mathbf{K})$, or equivalently, the full width half-maximum (FWHM) of the Lorentzian in the energy domain, Γ, is given by

$$\Gamma(\Delta\mathbf{K}) = 2\hbar\alpha(\Delta\mathbf{K}) = 2\hbar D\Delta\mathbf{K}^2. \tag{40}$$

The key features for continuous random motion are the exponential decay and the quadratic dependence of α on momentum transfer, $\Delta\mathbf{K}$, as illustrated in Fig. 10. In the limit of large length-scales, or measurements of sufficiently small $\Delta\mathbf{K}$, all diffusion must conform to this macroscopic limit.

At sufficiently low temperatures, atomic scale motion becomes dominated by the periodic arrangement of atoms and we expect to see the effect of discrete hops between adsorption sites. Hopping motion was first analysed by Chudley and Elliot in order to analyse neutron scattering data from 3D liquids [127]. Following from this work, similar expressions were developed by Frenken et al. to describe the hopping of atoms on surfaces [128,79]. The starting point is the rate equation
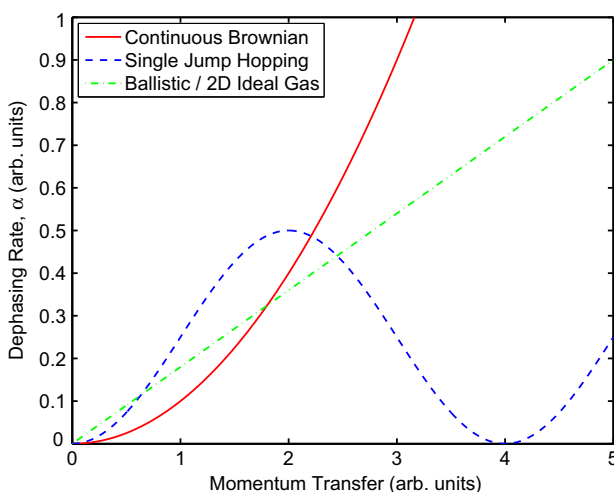

Fig. 10. Illustration of spin-echo QHAS signatures for simple modes of diffusion. Random motion gives an exponential decay in $I(\Delta\mathbf{K}, t)$. For continuous random motion the decay rate, α, varies quadratically with $\Delta\mathbf{K}$, whereas for hopping the dependence is sinusoidal with a period given by the jump length. Ballistic motion gives a Gaussian decay in $I(\Delta\mathbf{K}, t)$, whose FWHM varies linearly with $\Delta\mathbf{K}$.

$$\frac{\partial G_s(\mathbf{R}, t)}{\partial t} = \sum_j v_j [G_s(\mathbf{R} + \mathbf{j}, t) - G_s(\mathbf{R}, t)],$$ (41)

for instantaneous jumps on the appropriate Bravais lattice, where the sum is over the number of allowed jump vectors, **j**. The solution [79] also gives an exponentially decaying intermediate scattering function, $I_s(\Delta\mathbf{K}, t) = \exp[-\alpha(\Delta\mathbf{K})|t|]$, with the rate $\alpha(\Delta\mathbf{K})$ given by

$$\alpha(\Delta\mathbf{K}) = 2 \sum_j v_j \sin^2\left(\frac{\Delta\mathbf{K} \cdot \mathbf{j}}{2}\right).$$ (42)

In the energy domain, we also have a Lorentzian quasi-elastic peak shape, with FWHM $2\hbar\alpha(\Delta\mathbf{K})$. In this case, the 'signature' of the motion is a sinusoidal dependence of $\alpha(\Delta\mathbf{K})$, as illustrated in Fig. 10. The $\Delta\mathbf{K}$ position of the minimum corresponds to the position of the Bragg diffraction peak for the surface. All lattice sites scatter in phase at a Bragg peak, so the amplitudes contributing to $I(\Delta\mathbf{K}, t)$ are insensitive to jumps between sites, resulting in a dephasing rate, α, of zero. When a number of different jump lengths are possible these simply contribute to the overall value of α as a number of Fourier components. In the small $\Delta\mathbf{K}$/ long length-scale limit, the sinusoidal form approaches the quadratic form given in Eq. (40). The tracer diffusion constant for a particular direction can be estimated from the hopping rate using [83]

$$D_{\Delta K} = \frac{1}{2} v \langle j_{\Delta K}^2 \rangle,$$ (43)

where $j_{\Delta K}$ is the diffusion along a particular $\Delta\mathbf{K}$ direction, and D_K is the resulting diffusion coefficient in that direction.

If the corrugation of the substrate appears small, compared to the energy of diffusing particles, and their coupling to the substrate is also weak, we expect to observe ballistic, 2D gas like motion on sufficiently small length and timescales. In this case, the pair correlation function will be given by [129],

$$G_s(\mathbf{R}, t) = \frac{1}{\pi(v_0 t)^2} \exp\left(-\frac{R^2}{(v_0 t)^2}\right),$$ (44)

where $v_0^2 = 2k_B T_s / m$. The corresponding Fourier transforms give a Gaussian lineshape in both the time and energy domains [129], yielding

$$S(\Delta K, \Delta\omega) = \frac{2\sqrt{\pi}}{v_0 \Delta K} \exp\left(-\frac{(\hbar\Delta\omega)^2}{(\hbar\Delta\mathbf{K} v_0)^2}\right),$$ (45)

where the corresponding FWHM is $\Delta E = \left(8 \ln 2 \hbar^2 k_B T / m\right)^{1/2} \Delta K$. In this case, in addition to the Gaussian lineshape, the variation of the FWHM is again distinct, this time linear with ΔK, as shown in Fig. 10. More generally, on small enough length and timescales, all motion appears Ballistic, so we expect this to be the limiting form for large $\Delta\mathbf{K}$.

These three basic signatures form the core references from QHAS experiments are usually interpreted, enabling us to understand the underlying mechanism of surface diffusion. Within the widely used Langevin framework, surface diffusion generally can be broadly divided into four categories, as shown in Table 3, which are each related to one predominant type of motion described above. How-

Table 3
Table indicating limiting regimes for diffusion in the Langevin framework, in relation to standard QHAS signatures for motion, with illustrative examples.

	Low PES corrugation	High PES corrugation
Low adsorbate–substrate friction	Ballistic motion $I(\Delta\mathbf{K}, t)$ Gaussian e.g. Xe/Pt(1 1 1) [129]	Extended 'long' jumps $I(\Delta\mathbf{K}, t)$ exponential e.g. Cs/Cu(0 0 1) [105]
High adsorbate–substrate friction	Continuous random motion $I(\Delta\mathbf{K}, t)$ exponential e.g. benzene/graphite [126]	Generally short jumps $I(\Delta\mathbf{K}, t)$ exponential e.g. Na/Cu(0 0 1) [130]

ever real systems, as described in Section 6 below, rarely exhibit a perfect single mode of motion, since for example real hops do not take place infinitely quickly, as implicitly assumed in Eq. (41). While these analytic models allow qualitative statements about the diffusion mechanisms, simple combinations of these models cannot usually reproduce real data quantitatively; combined molecular dynamics and scattering simulations are usually required.

5.2.2. Confined diffusion

In some systems there are physical constraints, such as the presence of steps or other forms of nanoscale patterning, which limit the freedom of movement of species. If a surface species is confined to a finite region, the effect on $G(\mathbf{R}, t)$ is to eliminate the probability of finding an atom outside the length-scale of the confinement. Fig. 11 illustrates this effect in 1D; Fig. 11a shows $G_s(\mathbf{R}, t)$ for a particle undergoing continuous random motion in 1D. With increasing time, the probability spike at $(\mathbf{R} = 0, \ t = 0)$ decays in height and broadens, with the process continuing indefinitely. However, if the diffusion is restricted, the probability spike decays only until the region of confinement has been fully explored and knowledge of the original configuration has been lost, as shown in Fig. 11b [104].

When Fourier transformed to provide the intermediate scattering function, a distinct signature for confined motion is evident. Fig. 11c shows the form of $I(\Delta\mathbf{K}, t)$, at several values of $\Delta\mathbf{K}$, for conventional random diffusion; a simple exponential form decaying to zero after long times. In contrast, for confined diffusion, as shown in Fig. 11d, the curves only decay to a finite value, which depends on the level of confinement compared to the length-scale of the measurement. In the small $\Delta\mathbf{K}$ limit, $I(\Delta\mathbf{K}, t)$ decays by only a small amount, whereas for larger values of momentum transfer the decay is larger as the effect of confinement is proportionally less apparent. A quantitative relation between the residual level and the region of confinement is given in [104,130]. The form of $I(\Delta\mathbf{K}, t)$ for confined diffusion is not a simple exponential. Several forms have been derived to model neutron scattering, which may be re-applied to model QHAS, a summary of which is given in [50] for incoherent scattering.
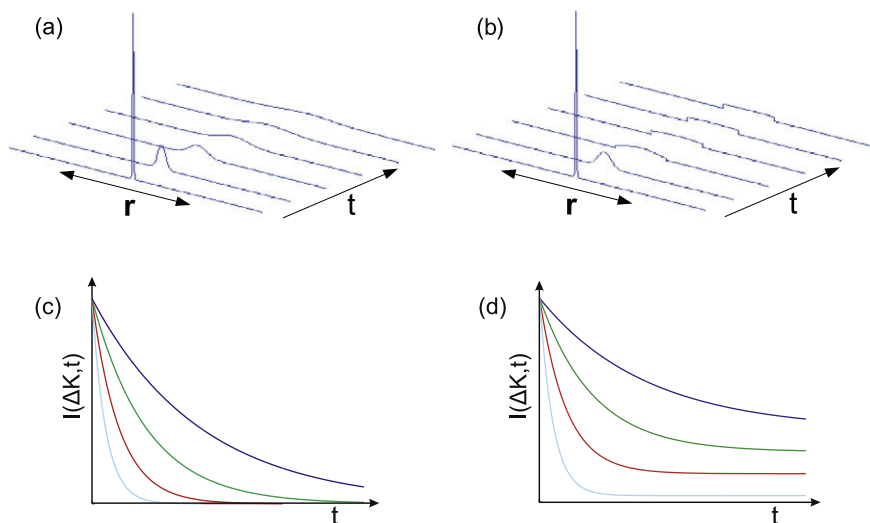

Fig. 11. Illustration of the features of confined diffusion in a QHAS measurement, following [78]. (a) Shows $G(r, t)$ for unconstrained diffusion in 1D, while (b) indicates equivalent motion when confined within a finite sized box. (c and d) Illustrate the respective forms of $I(\Delta\mathbf{K}, t)$ for random diffusion; faster decays correspond to larger values of $\Delta\mathbf{K}$. In the case of unconstrained diffusion, $I(\Delta\mathbf{K}, t)$ decays fully for all values of $\Delta\mathbf{K}$. In the case of confined diffusion, $I(\Delta\mathbf{K}, t)$ only decays to finite values, depending on the length-scale of the measurement compared to the region of confinement.

In the interpretation of experiment, which has a finite level of accuracy, the principal difficulty is in distinguishing the signature of confinement from an additional elastically scattered component, or if limited curvature is visible in the measurement, from a decaying process. In addition to the curvature of $I(\Delta \mathbf{K}, t)$, the variation of the residual level, analogous to the well known EISF in neutron scattering [50], is a key quantity. These characteristics of confined motion have been observed experimentally, [104,130], however, rather than using analytical forms, analysis of confined diffusion in QHAS to date has generally been interpreted through comparison with MD simulation.

5.2.3. Perpendicular motion

Although surface scattering experiments are usually concerned with momentum transfer parallel to the surface, $\Delta \mathbf{K}$, the scattered helium amplitude is determined by a phase factor which depends on the full 3D momentum transfer vector, $\mathbf{k}$, given by $\exp[i\Delta \mathbf{k} \cdot \mathbf{r}] = \exp[i\Delta \mathbf{K} \cdot \mathbf{R} + i\Delta k_z z]$. With care, QHAS measurements can therefore provide information about motion perpendicular to the surface, as demonstrated in [130].

Within a backscattering geometry such as the Cambridge apparatus, Δk_z only varies slowly with incidence angle, so can be regarded as constant in many experiments. Effects of perpendicular motion are only evident when the surface parallel contribution can be neglected, i.e. in the limit of $\Delta \mathbf{K} = 0$. Unconfined motion perpendicular to the surface will also result in desorption, so any surface-perpendicular motion is therefore expected to yield a confinement like QHAS characteristic, accompanied by a finite dephasing rate in the limit of $\Delta \mathbf{K} = 0$.

5.2.4. Vibration and intra-cell diffusive motion

Although quasi-elastic/spin-echo measurements are usually associated with diffusion, vibrational contributions are also present in the quasi-elastic peak. In their analysis of early Na/Cu(001) measurements, Chen and Ying first showed that the quasi-elastic peak in $S(\Delta \mathbf{K}, \Delta \omega)$ contains vibrational information [131], in the form of a wide background. More generally, the vibrational contribution to QHAS measurements can be considered as a combination of periodic and aperiodic motion, confined within a particular unit cell [88]. The periodic component is due to the oscillation of a particle moving in a potential well, and gives rise to oscillations in $I(\Delta \mathbf{K}, t)$, or the familiar energy loss/gain vibrational peaks in $S(\Delta \mathbf{K}, \Delta \omega)$. Superposed on this completely deterministic motion is the effect of anharmonicity in the potential and coupling to the substrate heat bath, which results in dephasing of the oscillations. The dephasing element of the motion is aperiodic, so appears as an additional (usually rapid) decay in the absolute value of $I(\Delta \mathbf{K}, t)$, and correspondingly as an additional (usually very wide) broadening of the quasi-elastic peak in $S(\Delta K, \Delta \omega)$. The motion remains confined to the unit cell, so $I(\Delta \mathbf{K}, t)$ only decays to a finite value, depending on momentum transfer, as described above.

The rate associated with dephasing of the frustrated vibration mode, or intra-cell diffusion, is closely linked to the frictional adsorbate–substrate coupling term, η. Vega et al. provide expressions which enable the friction coefficient to be extracted from the quasi-elastic peak [132,124]. Values of η are typically lie in the range $0.1\text{--}5$ ps^{-1} and the precise value indicates the timescale of the decay in $I(\Delta \mathbf{K}, t)$ or the width of the quasi-elastic energy broadening. The intra-cell rate of decay of $I(\Delta \mathbf{K}, t)$ is usually considerably faster than intra-cell hopping, hence allowing the two processes to be distinguished through separation of timescales. Usually, in spin-echo experiments this can be accomplished by control of the temperature, given the temperature dependence of inter- and intra-cell motion is quite different.

Providing the two components can be separated in the time domain, they should also be distinguishable in the energy domain, where inter-cell diffusion usually shows up as a narrow peak while intra-cell motion gives a much broader, peaked background. However, in early TOF experiments the limited experimental resolution convolved both processes together, making it impossible to distinguish the true behavior of the system [88,28,89,91]. Generally, if the two processes cannot be separated we expect the resulting mixture to give a rise in $\alpha(\Delta \mathbf{K})$ with increasing $\Delta \mathbf{K}$, which becomes pronounced above $\Delta \mathbf{K} \cdot \mathbf{R} \sim \pi/4$ [88]. If the time domain measurement does not decay significantly, Fourier transforming is unlikely to give satisfactory results, since as in any measurement, the Fourier transform window will broaden and distort the features in the energy space.

5.2.5. Correlated motion

Two signatures of correlated motion in QHAS measurements have been established in the literature. Generally, in systems where there is an attractive interaction between adsorbed species, reducing the temperature leads to a 2D gas to liquid phase transition. The characteristic feature of the liquid state, compared to solid or gas phases, is correlated motion. Ellis and Graham showed [133] that a key characteristic feature of such behavior is the presence of a finite gradient in the $\alpha(\Delta K)$ signature at small values of ΔK. In contrast, for all signatures of isolated diffusion, both the value of α and the gradient of $\alpha(\Delta K)$ tend to zero in the long length-scale limit. Ellis and Graham also showed that the value of α provides the most sensitive measurement of the phase transition condition, compared to several other experimentally observable quantities.

In the case of repulsive interactions, which also give rise to correlations in atomic scale motion, we observe a narrowing of the linewidth in the surface experiment that is closely analogous to same effect seen in liquids and originally explained by De Gennes [134]. Strongly repelling adsorbates tend to order themselves into a quasi-hexagonal arrangement that maximises the mean interatomic spacing, as illustrated in Fig. 12. On a more realistic surface, the degree of ordering will depend on the relative importance of the inter-adsorbate forces compared to the adsorbate–substrate forces (only an uncorrugated surface will give a perfect hexagonal overlayer), and the disordering effect of temperature. In an ideal hexagonal structure the inter-adsorbate forces are balanced. In other configurations, the forces are not balanced exactly so there is a net force, which acts to reduce the stability of that particular configuration and increase the likelihood of further, *correlated*, motion.

For adsorbates spaced at the preferred hexagonal distance, the dephasing rate, α, of the adsorbate configuration will be lower than the rate for atoms spaced at other length-scales, in other words the lifetime of that configuration will be longer. In the energy domain the increased stability yields an equivalent *narrowing* of the dynamic structure factor. Consequently, the signature of strong, repulsive forces is correlation in the motion, which is seen as a dip in $\alpha(\Delta K)$ at $\Delta K = 4\pi/\sqrt{3}a_{hex}$, which also corresponds to the position of the diffraction ring associated with the incommensurate hexagonal structure, where a_{hex} is nearest neighbour distance in the pseudo-hexagonal structure. At other values of ΔK there will be an increase in $\alpha(\Delta K)$ corresponding to the reduced lifetime of configurations, on longer and shorter length-scales, as indicated in Fig. 12 (see also online information supplementary to [135]). Such features have been observed in several recent studies [130,105], confirming the nature of the forces between adsorbates. However, correlated motion is notably absent in other systems where strong inter-adsorbate forces have previously been expected [135], forcing reinterpretation of the established body of experimental literature.
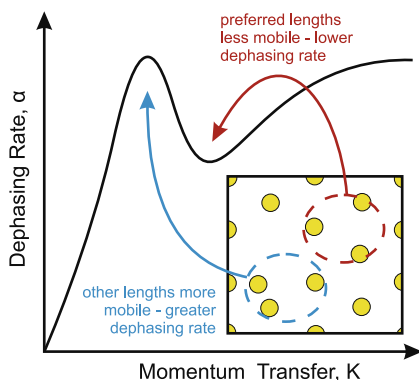

Fig. 12. Illustration of the signature for correlated motion originating from repulsive adsorbate–adsorbate interactions. Repulsion causes adsorbates to arrange into a thermally disordered, incommensurate quasi-hexagonal structure, whose quality depends on the strength of the interactions. Configurations close to the equilibrium structure are more stable, so correspond to a lower dephasing rate, α, than other configurations. These manifest as a peak and de Gennes narrowing 'dip' in the $\alpha(\Delta K)$ signature, whose presence and amplitude provide a sensitive and unique measurement of inter-adsorbate forces.

5.2.6. Rotational motion

QHAS can observe rotational motion through its quasi-elastic signature. Note that such a measurement is distinct from inelastic excitation of a well defined rotational mode. Rotation is visible providing the mobile species has a rotationally asymmetric scattering cross section, and its asymmetry is not overwhelmed by overall giant scattering cross section of the species.

Signatures of rotational motion have been established in order to interpret quasi-elastic neutron scattering measurements [50], which provide a basis for QHAS analysis. Pure rotational characteristics of $I(\Delta\mathbf{K}, t)$ resemble those of confined diffusion, since the rotational centre constrains the motion of the rest of the molecule. In this case, the functional form of $I(\Delta\mathbf{K}, t)$ consists of a series of exponential terms [50], which depend on whether rotational motion proceeds as a continuous process, or as rotational 'hopping'. Misfitting $I(\Delta\mathbf{K}, t)$ with a single exponential can provide an approximate $\alpha(\Delta\mathbf{K})$ signature, which usually consists of plateaus and peaks, caused by the differing dominant exponential terms, which depend on the periodicity and effective radius of the motion. As in the case of confined motion, $I(\Delta\mathbf{K}, t)$ decays to a finite value, and the variation of the limiting values with momentum transfer also provides information about the rotational geometry.

In real systems, rotational contributions will generally be mixed with translation, as in the case of propane on Pt(1 1 1) [124]. Here, molecular dynamics simulations provided a simpler approach to modeling the system, allowing experimental data and simulation, including both rotation and translation, to be compared directly. In the propane/Pt(1 1 1) system, rotational contributions to motion were much smaller than predicted by the literature [124]. Rotationally dominated adsorbate motion has not been observed to date.

5.3. Analytical modeling of QHAS

As discussed in Section 2.1, a huge range of literature exists describing approaches that have been used to model surface dynamical processes analytically. The field includes several models which have been developed or applied specifically to reproduce experimental QHAS measurements, which we discuss here. Generally, these attempt to treat QHAS measurements more completely than the simple analytic models described above, typically given existing dynamical frameworks. These provide important techniques for interpretation of measurements and provide alternative methods to extract simple dynamical parameters from experimental data, without requiring large numerical calculations.

5.3.1. Generalised quasi-elastic line shapes

As surface motion varies between random and ballistic regimes, by for example decreasing friction, or increasing temperature or momentum transfer, the intermediate scattering function changes from an exponential form to a Gaussian form, or correspondingly from a Lorentzian to Gaussian in the energy domain, as given above for the limiting cases. Miret-Artes and co-workers have shown that in the limit of an uncorrugated surface the lineshape can be described by a universal analytical form [136–138]. Here, the intermediate scattering function is expressed as

$$I(\Delta\mathbf{K}, t) = \exp[-\chi^2(e^{-\eta t} + \eta t - 1)], \tag{46}$$

which in the energy domain corresponds to a sum of a series of Lorentzian terms,

$$S(\Delta\mathbf{K}, \Delta\omega) = \frac{e^{\chi^2}}{2\pi} \sum_{n=0}^{\infty} \frac{(-1)^2 \chi^{2n}}{n!} \frac{2(\chi^2 + n)/\tau}{\Delta\omega^2 + [(\chi^2 + n)/\tau]^2}, \tag{47}$$

in terms of a shape parameter, χ, defined as

$$\chi \equiv \sqrt{\langle v_0^2 \rangle} \Delta K / \eta = \bar{l} \Delta \mathbf{K}. \tag{48}$$

η is the adsorbate–substrate coupling or friction, and $\bar{l} \equiv \tau \sqrt{\langle v^2 \rangle}$ is the mean free path. In the Brownian limit, corresponding to small $\Delta\mathbf{K}$ and high friction, $\chi \ll 1$, so $I(\Delta\mathbf{K}, t)$ becomes exponential and $S(\Delta\mathbf{K}, \Delta\omega)$ Lorentzian, with the $n = 0$ term being dominant. Conversely, in the ballistic limit, χ is large

and both $I(\Delta\mathbf{K}, t)$ and $S(\Delta\mathbf{K}, \Delta\omega)$ become Gaussian. They suggest treating the dephasing rate or quasi-elastic peak width by using a free parameter, μ, which takes a value between 0 and 1,

$$\Gamma = 2\hbar\alpha = 2\mu\eta\chi^2 + 2\sqrt{2\ln 2}(1 - \mu)\eta\chi.$$

The method has been applied to describe data for the uncorrugated Xe/Pt(111) system. There is good agreement between data and Langevin simulations and the calculations display a change in line-shape, analogous to the *motional narrowing* effect seen in magnetic resonance experiments.

More recently, Martinez-Casado et al. have extended the above model to include quantum effects [139]. Here, they show that a quantum treatment of the phase correlation-functions leads to an imaginary component in the intermediate scattering function, which then becomes complex. As in the case of neutron scattering [140], the imaginary part can be understood from the recoil of the target species during the scattering process. Helium is a light atom and, for all but the lightest adsorbates, the recoil is small and therefore the imaginary component in the intermediate scattering function is expected to be much smaller than the real part. The effect is illustrated with results for Na diffusion on uncorrugated surfaces, where an analytic form for the complete ISF is given, and on corrugated surfaces, where numerical simulations are required.

5.3.2. Combined vibration-jump models

In the past, diffusion and vibration have typically been treated separately due to the distinct time-scales in conventional diffusion measurements. Several approaches have been developed to treat QHAS measurements, where it is important to treat both on an equal footing. The earliest of several treatments are usually attributed to Chen and Ying [131,141], who applied a Mori projection operator formalism to obtain the dynamic structure factor, based on a particular adsorbate–substrate potential. They obtained good agreement with early TOF QHAS data for Na/Cu(001) and demonstrated the importance of the vibrational contribution to the quasi-elastic peak.

More recently, Martinez-Casado et al. [142] adopted a different approach to obtain a generalised form for both the quasi-elastic and T-mode peaks in $S(\Delta\mathbf{K}, \Delta\omega)$. They assume that the velocity autocorrelation function usually follows the general form

$$C(t) = \langle v_{\Delta K}^2 \rangle e^{-\gamma t} \cos(\omega_T t + \delta), \tag{49}$$

which leads to a form for $S(\Delta\mathbf{K}, \Delta\omega)$ in terms of the three parameters, γ, ω_T and δ. By taking these parameters as adjustable, they achieve excellent reproduction of the shape of the dynamic structure factor in simulations based on Langevin numerical simulations [142].

5.3.3. Models of transport rates

Interpretation of QHAS typically requires either the use of simple analytical models with a number of possible free parameters (such as Eq. (42)) or numerically intensive techniques. Chen and Ying have applied the Mori-projection operator formalism described above [131,141]. Guantes et al. have reported application of Kramers' turnover theory to model experimental results in the activated hopping regime [143,24]. The model provides a two parameter representation of activated diffusion on a model potential, in terms of a spatial diffusion rate and the energy loss to the surface. It provides good estimates of rates, diffusion coefficients and jump distributions, giving a useful alternative to Langevin MD analysis. It is suited to diffusion in one-dimensional systems, providing the reduced potential barrier, $V/k_B T$ is greater than ~ 3. However, application to multidimensional diffusion is considerably more complicated.

5.3.4. Interacting single adsorbate model

An interesting approach developed by Miret-Artes and co-workers to simplify the analysis of interacting systems is the interacting single adsorbate (ISA) model [33,34,32,35]. The idea is to replace the interaction forces between adsorbed species with a shot noise term being applied to a single atom, in the same spirit that the Langevin approach replaces the true dynamical interactions with the substrate with Gaussian white noise. The ISA model corresponds to a Langevin description, except there are two

effective friction terms, corresponding to a collisional friction, in addition to the usual adsorbate–substrate friction.

Application of the model gives remarkable reproduction of TOF measurements of Na/Cu(001), without requiring free parameters to be adjusted. However, we should note that the single-atom nature of the scheme does not allow for the effects of multiple-atom correlations in the motion that have been seen in recent spin-echo measurements [130]. Previous TOF experiments did not observe the correlated motion because the energy resolution did not allow a full deconvolution of the scattered signal [82]. While powerful, the ISA model should not be regarded as giving a full description of the correlated aspects to the motion in the Na/Cu(001) system.

5.4. Molecular dynamics techniques

Most real systems contain a mixture of the above signatures and cannot be analysed fully using simple analytical methods. The most general alternative approach, which has been widely used in the interpretation of QHAS, is the application of molecular dynamics simulations. Such simulations have two distinct aspects, as they need to both simulate the trajectory of adsorbed atoms on the surface and calculate the scattered helium intensities. QHAS MD simulations are usually treated as a minimalist computational experiment, and the results are treated in exactly the same way as experimental QHAS data. Simulation parameters are adjusted to enable features in the data to be understood, rather than providing a comprehensive simulation of the system.

For the trajectory simulation part, both many atom slab simulations [144,145] and Langevin simulations have been used (for example, [27,125,30,130]). Slab calculations can in principle reproduce a wide range of the motion in the system, associated with both substrate motion (phonons) and adsorbates (internal vibrations, frustrated translations, diffusion etc.). Langevin simulations have been used more widely, as the simulations usually run more quickly and the associated parameters can be related to simple models of the system more directly, enabling key features in the data to be identified. The simple Langevin friction parameter can also include contributions from electronic processes, as well as phononic, potentially improving the overall fit [146]. Currently, first principles molecular dynamics simulations are too computationally expensive to be of use for analysing behavior in the nanosecond regime, and are not yet very reliable for surface systems, as diffusion barriers are often much smaller than the uncertainty in the calculations. Accelerated trajectory techniques are generally not appropriate, since the simulations need to create $G(\mathbf{R}, t)$ through the complete time evolution of the simulation.

To date, almost all published simulations use simple kinematic scattering from mobile adsorbate atoms, with a constant form factor. One report using an improved approximation showed little difference [125]. Since the scattering calculations have to be repeated throughout the time evolution of the system, the more sophisticated techniques, such as quantum mechanically exact calculations using a realistic, soft, potential are prohibitively time consuming.

5.5. Requirements and limitations for spin-echo QHAS measurements

It is informative to point out a few of the practical requirements for spin-echo QHAS measurements. Clearly, it is essential that the system is mobile, in a stable dynamic equilibrium. Measurements typically take between a few minutes and a few hours, depending on the levels of signal available and the system must behave in a consistent way during this time. The surface species must also be mobile in a suitable time window, usually between picoseconds and nanoseconds. Whilst temperature can be used to adjust the rate of the system, if it is increased too much many species will also begin to desorb. Desorption can be countered, to some extent, through the use of an overpressure to maintain a dynamic equilibrium coverages [30].

It is self evident that the species being studied must be visible to the helium beam. Most species have relatively large diffuse scattering cross sections for helium [54], enabling measurements down to low coverages. As indicated by calculations using different scattering models [125], the detailed shape (the form factor) of adsorbates does not seem to be critical in understanding dynamics. For simple adsorbed atoms, measurements at around 1% coverage can be obtained [105], corresponding to a

mobile population of around 2×10^{12} cm^{-2}. Since QHAS provides no direct chemical sensitivity, it is essential to have good independent understanding of the species present. Complementary information from other techniques is often essential.

The range of dynamical systems that are accessible is determined by the Fourier time range, or equivalently the energy resolution, of the instrument concerned. In fact, there are three relevant 'resolution' quantities. The intrinsic resolution corresponds directly to the maximum Fourier time. For the Cambridge apparatus with a beam energy of 8 meV, the maximum Fourier time is ∼700 ps, giving an energy spectrum reconstruction resolution of ∼3 μeV. In practice, if we make the assumption of random motion, such that the form of $I(\Delta \mathbf{K}, t)$ will be exponential, it is usually possible to fit the curvature of a measurement and obtain dephasing rates as low as about 0.75 ns^{-1}, which corresponds to a Lorentzian energy broadening of about 1 μeV. Finally, if we also assume the level to which $I(\Delta \mathbf{K}, t)$ decays, and its dependence on $\Delta \mathbf{K}$, it is possible to extract dephasing rates which are much smaller again, typically down to ∼0.015 ns^{-1} or ∼20 neV. However, although such an assumption may allow useful relative information to be extracted, it can introduce significant systematic errors in the absolute rates.

The maximum Fourier time depends on the magnetic design of a given instrument, but is also a strong function of beam energy. Currently, times as long as a few nanoseconds have been realised using very low energy beams [100]. Larger magnetic field integrals can be achieved using longer and stronger magnets, providing sufficient signal is available to make $1/r^2$ intensity losses in acceptable. In the long term, ongoing neutron scattering instrumentation projects aim to achieve a spin-echo time of ∼1 μs [99], and similar approaches may eventually be possible with helium-3 beams. Although the velocity spread has only a weak, second order effect on the energy resolution of QHAS measurements, it does affect the momentum spread in the beam, placing an uncertainty on $\Delta \mathbf{K}$ resolved measurements which increases linearly with $\Delta \mathbf{K}$. The finite angular resolution of the scattering apparatus also broadens the momentum spread, but this effect is usually much smaller. Finally, the major limitation on current ^{3}HeSE experiments is the signal level available, which is dominated by the detector efficiency, as discussed above.

6. Experimental measurements of translation, rotation and vibration

A number of systems studied with helium spin-echo have now been published. We summarise them here to illustrate the modes of motion described in the previous section and to demonstrate some of the opportunities the technique presents in increasing our understanding of fundamental surface processes. The experimental results are separated into measurements of diffusion and vibration, with a further section discussing the more distinct field of selective adsorption resonance. Within the diffusion measurements, we look first at atomic adsorbates, followed by simple and increasingly complex molecular species.

6.1. Adsorbed atoms

6.1.1. Alkali metals on Cu(001): Na/Cu(001), Cs/Cu(001)
Na on Cu(001) is the system which has been most extensively studied using QHAS, and consequently has become a benchmark system for both experiment and theory. A substantial body of literature based on TOF–QHAS measurements has characterised the diffusive motion seen in some detail [82,131,144,133,27,146,147,125], and at low coverages the system is well understood. However, despite extensive efforts, the high coverage aspects of the original time of flight data had remained unexplained, making the system an exciting proposition for further measurements using the greater resolution offered by ^{3}HeSE. To understand the context of the new data, we briefly summarise the prior knowledge obtained through the TOF experiments.

Initial QHAS measurements at a coverage of 0.1 ML showed widely separated adatoms hopping between sites [82]. The diffusion mechanism was seen to be predominantly single jumps between nearest neighbour lattice sites, while an Arrhenius plot of quasi-elastic broadenings gave an effective activation energy of 51 meV. Moving slab MD simulations modeling the data showed good agreement with

experiment, except for the lowest momentum transfers, where the broadenings were larger in the model, an effect the authors attributed to an over-estimation of multiple jumps [144]. A series of further quasi-elastic and T-mode vibrational measurements at low coverages, below 0.11 ML, were analysed using Langevin MD simulations [27,146]. The work established a detailed empirical adsorbate–substrate PES which successfully reproducing both diffusive and vibrational properties of the system. Corresponding adiabatic diffusion barriers over the top and bridge sites were 84 meV and 75 meV, respectively, with a friction coefficient of 0.9 ps^{-1} describing the coupling between the sodium and the substrate. Finally, TOF measurements at even higher coverages (up to 0.18 ML) showed an increasing activation energy with coverage, higher maximum quasi-elastic broadenings and an increasingly rapid rise of the quasi-elastic energy broadening at small momentum transfers, which became almost constant at larger values of $\Delta \mathbf{K}$ [125]. The first of these features was explained in terms of an increased amount of correlated motion at higher coverages caused by dipole–dipole repulsion between adsorbed sodium atoms. These repulsive forces were successfully modeled in the MD simulations by incorporating a Kohn–Lau dipole repulsion model [148]. However, the anomalous behavior at small momentum transfer and the dramatic increase in the maximum broadening remained unexplained.

Prior to the latest experimental data, a body of theoretical work began to form, firstly comparing Kramers' turnover theory with the experimental diffusion measurements [143], then modeling the positions, widths and temperature dependence of the T-mode data [137]. Further work by Martinez-Casado et al. concerned a generalised Chudley–Elliot model, which accounts for coupling between the T-mode and diffusive motion, also used Na/Cu(001) as a model system [142]. In order to try to explain the strong coverage dependence of the original TOF data, the same authors then considered an interacting single adsorbate (ISA) model [32,34,35] where a white noise term gives the surface friction and the adsorbate–adsorbate interaction potential is replaced by a shot noise term. Although the model apparently gives a good fit to the original TOF data, the features of correlated motion resolved by the more recent spin echo measurements cannot be reproduced within the ISA formalism. Conversely, other work predicted signatures of correlated motion in the system which were not observed in the early experimental data [147,149].

The increased resolution of the spin-echo technique allowed measurements to be performed on the Na/Cu(001) system without requiring assumptions about the quasi-elastic lineshape [130]. Low coverage measurements were consistent with the TOF data, while at higher coverages, direct observation of the lineshape revealed more complex surface dynamics than had previously been assumed. In the low coverage limit, as shown in Fig. 13a, the momentum transfer dependence of the dephasing rate, α, follows the characteristic jump diffusion shape. Increasing the coverage to just 0.04 ML (Fig. 13b) introduces a regime where the adsorbate–adsorbate repulsive interaction gives rise to de Gennes narrowing features, which had previously been predicted but were not observed experimentally due to the lack of resolution. A further increase of the coverage, to 0.05 ML or more, saw the onset of an unanticipated change, shown in Fig. 13c and d. Here, $I(\Delta \mathbf{K}, t)$ was seen to maintain a finite dephasing rate even in the limit of small $\Delta \mathbf{K}$, which was accompanied by the curves decaying to a non-zero value. The effects could only be caused by motion perpendicular to the surface, with a distance of $\sim$0.2 Å, since the surface parallel momentum transfer under these conditions is zero. At slightly larger momentum transfers, contributions from surface parallel and perpendicular motions mix together, resulting in a complex lineshape. It is this phenomenon which gave rise to the deviations between the low resolution TOF measurements and the MD analysis of the system.

A quantitative analysis of the features corresponding to perpendicular motion showed that the phenomena has a similar activation energy to diffusion, suggesting that at higher coverages the adatoms must hop between locations which have different apparent heights above the surface (note that a transient change in height *during* the jump would not explain the data). 2D Langevin MD simulations reproduced the low coverage data using an adsorbate–substrate PES with the same energy barriers as the previous studies and with a friction coefficient of 0.5 ps^{-1}. Including the Kohn–Lau dipole repulsion model described earlier enabled the de Gennes repulsion features to be quantitatively reproduced, as shown by the dotted lines in Fig. 13. For the higher coverages, a simple 3D model for perpendicular adsorbate motion was included, shown by the solid lines in Fig. 13, where the vertical position of an adatom depended on the local Na density, which naturally fluctuates during the diffusion process.
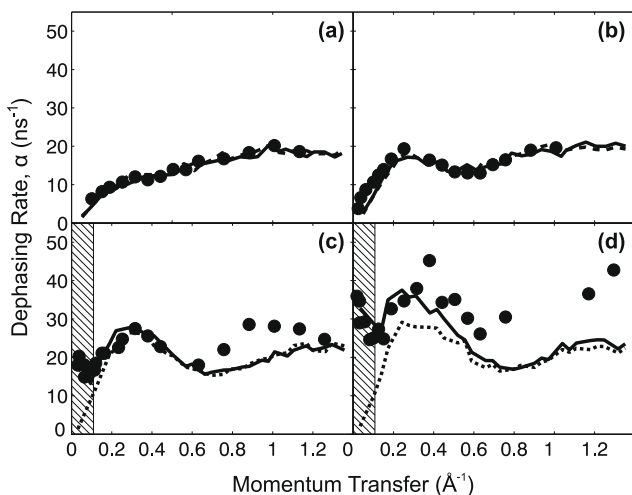
Fig. 13. Experimental dephasing rate data for the diffusion of Na on Cu(0 0 1), reproduced from [130]. The points correspond to measurements at coverages of 0.02, 0.04, 0.05 and 0.08 ML, respectively. (a) Shows jump diffusion in the low coverage limit, while (b) also shows the onset of correlated motion, resulting in the additional peak and dip de Gennes narrowing structure. (c and d) Also show the onset of an additional process at low momentum transfers, shown by the shaded region and discussed in the text. The dotted and solid lines show 2D and 3D Langevin MD simulations, respectively, used to reproduce the data.

Further theoretical work [150] has established a more complete understanding of the 3D motion, which highlights the significance of the electronic properties of the system in the resulting QHAS data. Using *ab initio* density functional theory simulations, Fratesi et al. [150] studied the contribution of both the position of the ion cores and of the electronic distribution to the apparent height of the sodium atoms, and how this varied with local coverage. A similar level of perpendicular motion was observed and found to be attributable to alterations in the electron distribution, which followed fluctuations in the local concentration of adatoms. It is thus an electronic effect, rather than the motion of the sodium ion cores, which can reproduce the experimental data, illustrating the potential of the spin-echo technique for measurement of surface electronic properties.

Another example where high resolution spin-echo measurements have dramatically changed our understanding of adsorbate dynamics is the Cs/Cu(0 0 1) system. Here, measurements reported in [105] demonstrated that Cs is in fact highly mobile, and is not simply vibrating, as previously understood to be the case [151]. As with Na, these measurements contrasted with previous attempts using TOF, which had been unable to identify diffusion, although a very low energy Cs overlayer acoustic vibrational mode had been seen [151]. Measurements were made for coverages between 0.014 ML and 0.056 ML (limited by the available scattered intensity), and temperatures between 80 K and 130 K. One of the main features of the Cs system was that the low energy acoustic mode was found to mix in with the diffusion characteristic, as both occur on similar timescales in the accessible experimental window. Although the vibration gives rise to decaying amplitude oscillations in $I(\Delta\mathbf{K}, t)$, while diffusion gives rise to an overall decay, the two are difficult to separate, as evident from the typical results in Fig. 14a and b. Consequently, ^{3}HeSE analysis was carried out in the energy domain, shown in Fig. 14c and d, where distinct energy transfer peaks and their associated widths could be distinguished.

Although the mechanism for Cs transport remains jump-like, the system is rather different to that of Na. Cs moves much more freely, and from the $\alpha(\Delta\mathbf{K})$ characteristic [105], there is a significant contribution from multiple jumps at low coverages, indicating low adsorbate–substrate friction. At higher coverages, inter-adsorbate repulsion again dominates the dynamics. Cs repulsion causes very strong de Gennes features in the momentum transfer dependence of the quasi-elastic energy broadening, $\Gamma(\Delta\mathbf{K}) = 2\hbar\alpha(\Delta\mathbf{K})$, and is the origin of the previously observed acoustic overlayer vibrational mode. In the range of coverages studied, no sodium-like perpendicular motion was observed.
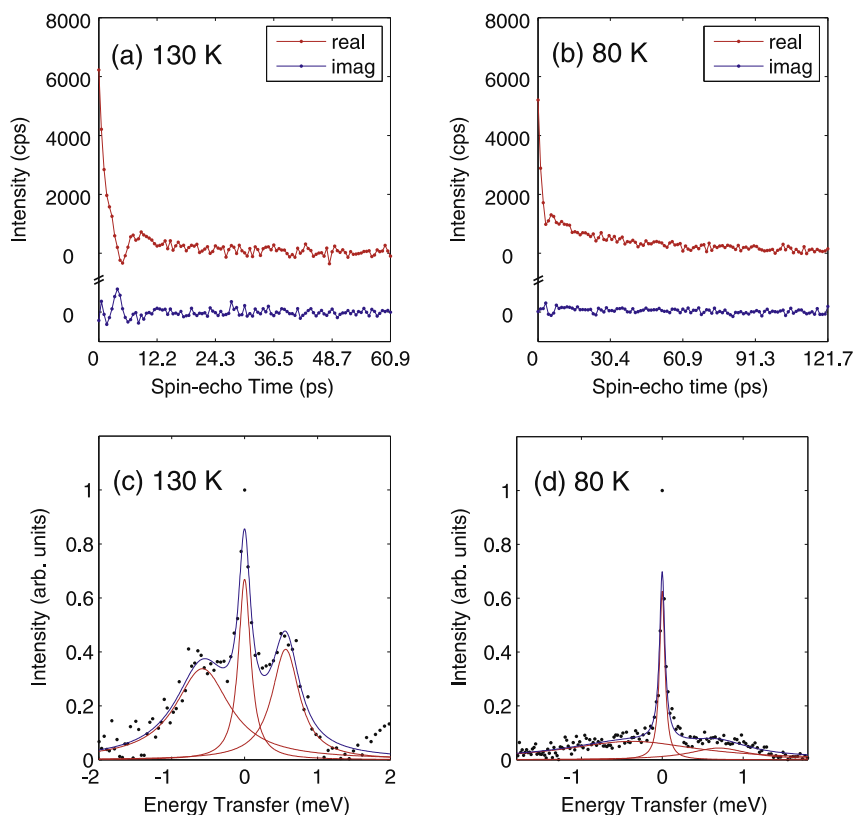
Fig. 14. Typical ³HeSE measurements for the diffusion and vibration of Cs on Cu(001) at a coverage of 0.044 ML, reproduced from [105]. (a and b) Show data in the time domain where the effects of diffusion and vibration are mixed together, due to the similar timescales involved. (c and d) Show the same data converted to the energy domain, where inelastic peaks at finite energy transfer can be distinguished more easily. The solid lines in show an optimised 3-Lorentzian fit to the data.

The application of Langevin MD simulations was used to investigate and quantify the behavior of the diffusion and vibrations. The detailed form of the behavior is a result of the balance between Cs–Cs and Cs-surface forces and of the frictional regime of the system. The true characteristics are revealed through the temperature and coverage dependence of the diffusion and, in particular, of the presence of the acoustic vibrations. Qualitative agreement between the simulations and experiment requires a small but finite PES corrugation and a small but finite friction. The simulations were then optimised to give a PES with a corrugation of 20 meV and an adsorbate–substrate friction of $1/40$ ps^{-1}. Again, good support was obtained for using the Kohn–Lau dipole force model to represent the interactions between Cs atoms.

6.2. Simple adsorbed molecules

6.2.1. CO/Cu(001)

One of the first sets of data resulting from the application of the ³HeSE technique was a measurement of the dynamics of CO/Cu(001) at a coverage of 0.1 ML [30]. The data was particularly useful as the results helped resolve a vigorous discussion in the literature regarding the activation energies obtained using QHAS, compared to other techniques (discussed in Section 2.3.3), and has identified limitations in *ab initio* models of this system.
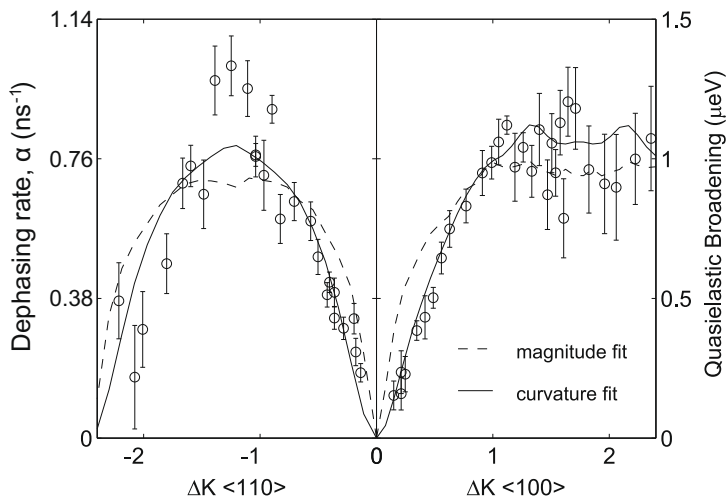
Fig. 15. Plot of experimental dephasing rates for the diffusion of CO on Cu(100) at a coverage of 0.1 ML and temperature of 190 K, reproduced from [30]. The lines are from 2D Langevin MD simulations where the friction is adjusted to either reproduce the maximum values of the dephasing rate (the *magnitude fit*) or the shape of the experimental data, particularly at low momentum transfer (the *curvature fit*).

The momentum transfer dependence of the measured dephasing rates for CO on Cu(001) at 190 K, shown in Fig. 15, clearly indicated a jump diffusion mechanism. Despite working at relatively high temperatures, by using an overpressure to maintain a dynamic equilibrium coverage above the usual desorption temperature, the rate of CO diffusion was still very small, giving dephasing rates of less than 0.5 ns^{-1}. These rates were much smaller than those expected from an earlier, but rather limited, TOF measurement on the same system [28]. Similar peak dephasing rates were seen in both lattice directions, indicating similar energy barriers across both bridge and hollow sites. Temperature dependent data gave Arrhenius activation energies of ∼125 meV.

Langevin MD simulations, treating the CO as a point adsorbate, were able to reproduce the approximate shape of the data and the peak dephasing rates, using an adsorbate–substrate friction of 1/13 ps^{-1}. The resulting potential was nearly isotropic with barrier direction, indicating that recent *ab initio* calculations of the adsorbate–substrate PES [91,152] require correction, at least at the fourfold hollow site.

However, these simulations also contain too many long jumps (they systematically overestimated the dephasing rates at low momentum transfer), as shown by the *magnitude fit* in Fig. 15, which gives the best overall fit to the data. The jump distribution could be improved by increasing the friction to 1/2 ps^{-1}, as shown by the *curvature fit*, although the absolute rate then became about five times too large (and which is scaled by a factor of about five to lie on top of the data for comparison). These observations suggested an alternative mechanism to remove long jumps was necessary [30], such as position dependent friction or the coupling of other molecular modes. An intermediate estimate of the friction parameter, at 1/8 ps^{-1}, from a previous study of the width of the CO *T*-mode [153] supports the suggestion that higher dimensionality is most important.

The resolution of the controversy in the literature came from the realisation that the hopping rates are much lower than expected from [28], and the corresponding PES barriers are much higher. We now believe [88] the previous measurements corresponded to intra-cell motion, which were mixed in by the limited resolution available with TOF. Intra cell diffusion is much more weakly activated, hence yielding the unusually small barriers that sparked the controversy. Finally, we should note that analysis of this particular set of very slow dephasing rate spin-echo data required the assumption of both an exponential decay form and an elastic background level (see Section 5.2). Whilst these assumptions enabled the data to be analysed satisfactorily, they make it impossible to distinguish unexpected phenomena, such as those seen in the case of Na/Cu(001).

6.2.2. CO/Pt(1 1 1)

CO on Pt(1 1 1) is the prototypical surface system and a vast body of both experimental and theoretical literature exists. Of particular relevance is a well established drop in both the heat of adsorption and the desorption temperature with increasing coverage [46,154,155]. These changes have been widely attributed to strong pairwise repulsion between CO molecules. Despite the general consensus that the system was well understood, after decades of research, recent [3]HeSE measurements [135] made the remarkable observation that these forces are absent, and have consequently forced a major reinterpretation of the nature of the system.

As expected, the diffusion of CO on Pt(1 1 1) was found to be strongly coverage dependent. [3]HeSE measurements [135] of the dephasing rate, α, are shown with increasing coverage in Fig. 16a. The shape of the curves clearly indicates jump diffusion. As the coverage increases, the magnitude of $\alpha(\Delta \mathbf{K})$ increases, reflecting an increase in the diffusion rate. However, the shape remains the same for all coverages studied between 0.065 and 0.3 ML. In contrast, pairwise CO–CO repulsion was expected to cause strong signatures of correlated motion in the data, as illustrated by the predictions of two MD simulations using the pairwise potential calculated by McEwen [156] and the substrate mediated interaction potential suggested by Petrova et al. [157], shown in Fig. 16b and c, respectively.

The unchanging shape of $\alpha(\Delta K)$ meant Alexandrowicz et al. could immediately conclude that pairwise repulsive forces between CO molecules cannot be driving the increase in the CO dynamics with coverage. They also concluded, via MD simulations and the incontrovertible differences between Fig. 16a and b/c, that the expected forces between CO molecules cannot be present, and estimated an upper limit of possible forces that could be consistent with experiment. Understanding the CO/Pt(1 1 1) system therefore requires a new *interpretation* of the existing experimental data. At first, the usual approach of modeling the experimental data using Langevin MD simulations seems inappropriate for this system. However, Alexandrowicz et al. found that the Arrhenius barriers for the motion decreased from 175 to 115 meV as the coverage increased from 0.065 to 0.3 ML, implying that an effective PES became significantly less corrugated [135]. In fact, the experimental data was successfully reproduced, without introducing pairwise CO–CO forces, using MD simulations in which the PES corrugation is reduced as a function of coverage and friction is taken, from a previous *T*-mode
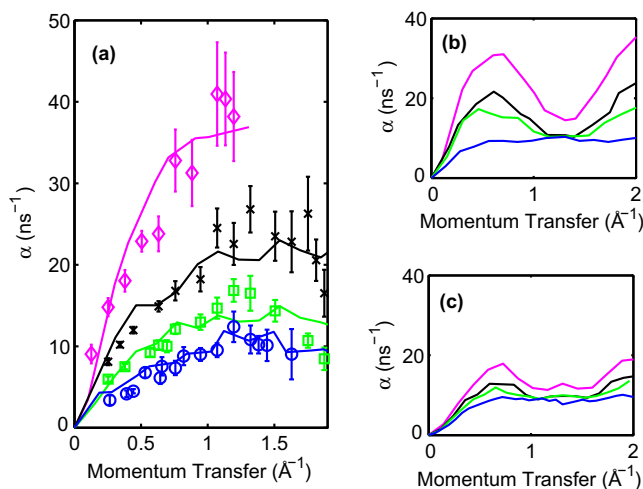

Fig. 16. (a) Shows [3]HeSE dephasing rate measurements for the diffusion of CO on Pt(1 1 1) at 340K along the $\langle 1\,1\,\bar{2}\rangle$ substrate direction, reproduced from [135]. The circle, square, cross and diamond markers correspond to coverages of 0.065, 0.165, 0.22 and 0.3 ML, respectively. The solid lines correspond to the results of Langevin MD simulations used to reproduce the data. (b) Shows equivalent MD simulations using the pairwise force model proposed by McEwen et al. to describe experimental data previously available for CO/Pt(1 1 1) [156]. (c) Shows equivalent MD simulations using an alternative substrate mediated force model proposed by Petrova et al. [157]. The results in (b and c) obtained using existing force models show strong signatures of correlated motion which are absent in the experimental data.

measurement [29], to be 0.7 ps^{-1}. It was concluded that CO adsorption results in 'mean-field' changes to the CO-substrate interaction, which are delocalised over a distance much larger than the typical CO–CO separation, and allow the molecules to move in a practically uncorrelated way.

It is now clear that the CO/Pt(1 1 1) system cannot be modeled realistically using any pairwise scheme, and it seems likely that the same may be true for many other systems that have been treated within the popular pairwise framework. Since measuring the fast, atomic scale dynamics provides the only adequate test of interaction models that is currently available, many similar dynamics measurements appear to be necessary, before we can in general be confident that the interactions in surface systems are represented correctly. In the specific case of CO/Pt(1 1 1), it seems likely that a detailed explanation of the underlying physical phenomena will prove a significant theoretical challenge.

6.3. Larger adsorbed molecules

6.3.1. Benzene/HOPG
Measurements of the diffusion of benzene on a highly-ordered pyrolytic graphite (HOPG) surface at 140 K illustrated for the first time a definitive observation of a high-friction viscous regime, where the adsorbate–substrate potential is unimportant to adsorbate diffusion [126]. The variation of dephasing rate with momentum transfer, obtained at a coverage of half a saturated monolayer, showed a quadratic dependence, as expected for continuous Brownian motion (see Section 10). For this system, the resulting motion can therefore be adequately described by a simple diffusion coefficient of $D = 5.39 \times 10^{-9}$ m^2 s^{-1}. Temperature dependent measurements gave an Arrhenius activation energy of 17 ± 12 meV, confirming the negligible PES corrugation. Langevin MD simulations modeling the benzene molecule as a hard-wall disk reproduced the data, identifying an adsorbate–substrate dissipative friction parameter of 2.2 ps^{-1} which was in good agreement with the value derived from the diffusion coefficient and adjusted for intermolecular collisions [126]. A further series of moving slab molecular dynamics simulations have been performed using the Compass force-field within the Cerius package [145]. These give good agreement with the experimental data, providing further insights into the system and supporting the use of such force-fields for surface oriented calculations. They also identify friction in the benzene/graphite system as being predominantly phononic. The unusually high values of friction suggest that such graphitic systems may be of particular use in future phononically driven nanoelectromechanical systems (NEMS), as recently demonstrated [158].

6.3.2. Propane/Pt(1 1 1)
The diffusion of propane on the Pt(1 1 1) provided an unusual opportunity for more complex forms of motion [124]. The system is unusual as the propane molecule sits conveniently within the hexagonal structure of the (1 1 1) surface. In principle, rotational motion around the hexagonal units of the surface is possible, as well as translational motion.

The system was studied using ^{3}HeSE at a coverage of 0.02 ML [124] and the usual quasi-elastic measurements were obtained with momentum transfer for a temperature of 115 K. Analysis demonstrated that the dynamics are dominated by translational diffusion within the surface plane, with an Arrhenius activation energy of 57 ± 4 meV. Additionally, $I(\Delta\mathbf{K}, t)$ was found to deviate from a purely exponential decay at small spin-echo times and reconstruction of the energy transfer spectrum allowed a broad, weak foot around the quasi-elastic peak to be resolved. The width of the feature reflects the frictional coupling between the adsorbate and substrate [88,137], allowing the friction coefficient for propane on Pt(1 1 1) to be estimated at 1.1 ps^{-1}.

An existing pseudo-triatom potential by Stinnett and Madix had previously been used to describe the trapping of propane on the Pt(1 1 1) surface [159] and was used as a starting point for Langevin MD analysis of the system. However, this PES was shown to completely disagree with the observed dynamics as it permitted fast rotations of the propane about the adsorption site and gave unrealistically low energy barriers to motion. Fig. 17 shows the alternative PES proposed, for the interaction between a methyl (methylene) group and the Pt surface, which is capable of reproducing the observed dynamics. While the validity of the pseudo-triatom approach in general and this PES in particular are not guaranteed, this result illustrates the basic properties of the true energy landscape, i.e. the barrier to both translation and rotation must be ~60 meV.

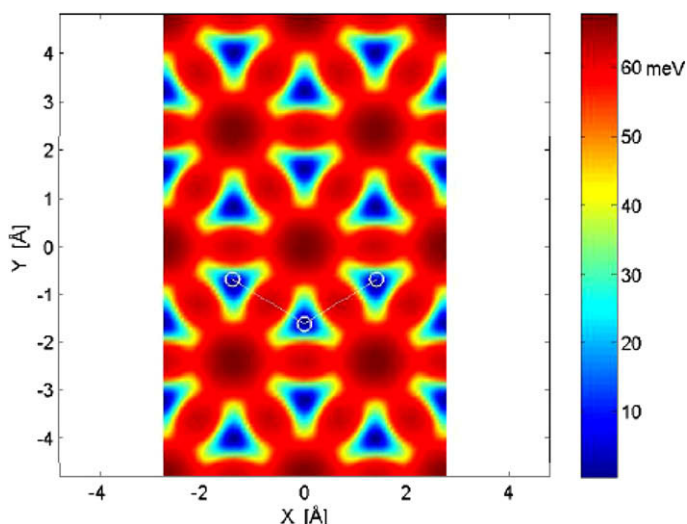**Fig. 17.** Illustration of the PES for propane adsorbed on Pt(1 1 1) which reproduces the essential features of the [3]HeSE data, reproduced from [124]. The potential is based on the existing PES of Stinnett and Madix [159], but was modified to reduce the amount rotational motion to that seen in experiment, and to fit the temperature and momentum transfer dependencies of the data. The white joined circles illustrate the position of the carbon atoms in a typical adsorbed propane molecule.

6.3.3. Coronene/Au(1 1 1)

The earliest application of helium spin-echo to the study of well defined adsorbate dynamics was performed by the de Kieviet group on the system of coronene ($C_{24}H_{12}$) adsorbed on a Au(1 1 1) surface [160]. The quasi-elastic energy broadening was measured for a selection of points in the temperature range 95–437 K and over a momentum transfer range of up to 0.25 Å^{-1}. The authors compared the experimental data with the expected forms for both continuous diffusion and a jump mechanism, concluding motion occurred along the [1$\bar{1}$0] in discrete jumps of ~19 Å. The Arrhenius energy barrier in this direction was measured as 30 ± 5 meV.

6.4. Phonon and low energy adsorbate vibrations

[3]HeSE studies have been used to provide phonon and adsorbate vibrational information for several systems. Measurements on the Cs/Cu(0 0 1) system [105] included an acoustic overlayer mode. Data was obtained by performing standard spin-echo measurements over a wide range of spin-echo times (including both real and imaginary components), followed by Fourier transforming to the wavelength domain and converting to energy to give $S(\Delta\mathbf{K}, \Delta\omega)$. The procedure gives spectra which are analogous to time of flight energy spectra, and resulting energy loss and gain peaks for a typical measurement are visible in Fig. 14c and d. Dispersion curves were obtained from the spectra, which were consistent with existing measurements and extended to much smaller energies and values of momentum transfer. Note that in a measurement tuned for the quasi-elastic peak (a standard spin-echo measurement) the quasi-elastic measurement is only limited by the maximum Fourier time of the instrument, but the finite energy transfer peaks are also broadened by the projection of the feature in the wavelength intensity transfer matrix, as illustrated in Fig. 5C. The true mode width can be obtained by calculating the broadening effect and accounting for both the spread of energies in the He beam and for the curvature of the dispersive mode, if necessary. The Cs/Cu(0 0 1) phonon data at low energy transfer provided strong support for the observation of a true acoustic mode. In conjunction with the observation of correlated hopping diffusion this data led to the determination of the low friction behavior of the system [105].

Cu(0 0 1) phonons have been studied using optimised tilted projections [104,78]. Here, much higher energy resolution at finite energy transfers was obtained by 'tilting' the ratio of the current in the two
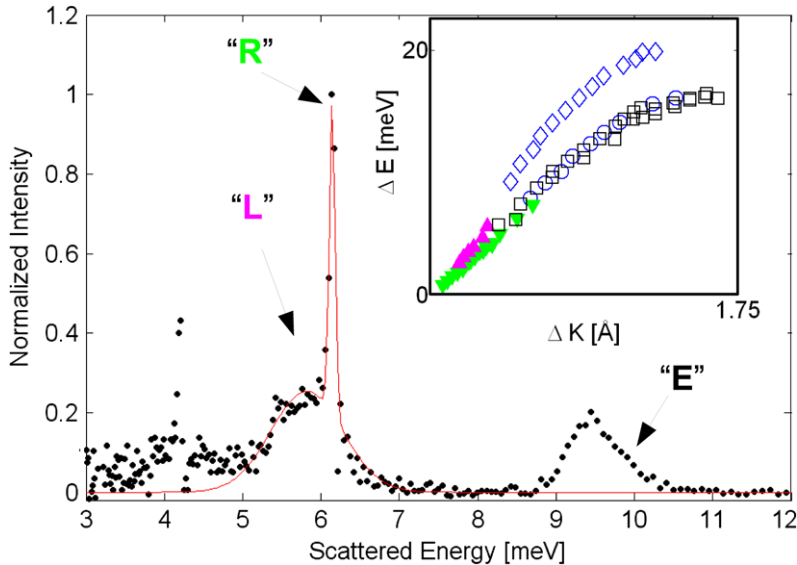
Fig. 18. Plot of the reconstructed energy distribution in a beam of helium scattered from a Cu(1 0 0) surface, using an optimised 'tilted-projection' to measure the Rayleigh mode (R) with minimal instrumental broadening (reproduced from [78]). Additional features are the longitudinal mode (L) and the elastic peak (E) which is broadened by the non-elastic optimised tilted-projection. The solid red line is a double Gaussian fit, used to extract the position of the peaks [78]. The inset shows dispersion curves obtained using spin-echo measurements (solid points) along with existing data obtained using time of flight HAS and EELS [162,163].

spin-echo coils, as described in Section 3.3. A typical measurement is shown in Fig. 18, which contains the elastic peak (E), the narrow Rayleigh mode peak (R) and the longitudinal resonance (L). The tilt has been adjusted to minimise the instrumental broadening of the Rayleigh mode, which is seen to be only ∼70 μeV wide. A consequence of this particular tilt angle is that the width of the elastic mode is broadened substantially instead. Dispersion curves at higher energies have already been established for the Cu(1 0 0) system, whereas these measurements extend the data set to much longer length-scales, as shown in the inset to Fig. 18 (solid markers). The measurements have also been used to provide highly accurate linewidth information and measurements of shift in phonon mode position with temperature. These gave a shift of 260 neV/K^{-1} for the Rayleigh mode at a momentum transfer of 0.27 $Å^{-1}$ along the ⟨1 0 0⟩ azimuth. Surprisingly, the surface mode appears to have a lower anharmonicity than the bulk, unlike the situation at large momentum transfers [161].

7. Elastic and resonant scattering with ^{3}HeSE

As well as being used for diffusion measurements, the spin-echo technique has found important application in providing measurements of resonant and elastic scattering. In this section we describe the background to such measurements, the Fourier transform helium atom scattering approach, and recent applications to probe helium-surface interaction potentials.

7.1. Selective adsorption resonance

The phenomenology of resonant scattering has been known since the earliest experiments with atomic beams and surfaces [57,164] and in its simplest form is a scattering process that is purely elastic. A simple semi-classical view of the process is illustrated in Fig. 3. Scattering at the resonance condition corresponds to a double scattering event; part of the incident wave is scattered directly into an open channel, **B**, while a fraction undergoes diffractive scattering into an evanescent, resonant state

propagating parallel to the surface. After a short time, a second process coherently scatters the wave into an open channel, **D**. Subsequent interference between the directly scattered and the resonantly scattered components leads to modulations in the outgoing intensity, which can be observed in experiment.

The semi-classical picture provides insights into the origin of the experimental intensity variations, however, the process can only be understood fully from a quantum standpoint [69]. For elastic diffraction involving the reciprocal lattice vector, **G**, the z-component of the scattered wave, $k_{G,z}$, can be written, in terms of the incident wavevector $k_i(\mathbf{K}_i, k_{iz})$ as

$$k_{G,z}^2 = k_i^2 - (\mathbf{K}_i + \mathbf{G})^2. \tag{50}$$

Open diffraction channels, with $k_{G,z}^2 > 0$, have a real and positive wavevector that corresponds to a beam emerging from the surface. The full, elastic intensity is carried by the open channels. Closed channels have $k_{G,z}^2 < 0$ and carry no intensity, since the z-component of the wavevector is imaginary and the wave is evanescent. The locus of points with $k_{G,z}^2 = 0$, for a given **G** vector, defines the threshold condition for that channel. Resonant scattering occurs in the region immediately below a threshold when the kinematic condition is such that

$$k_{G,z}^2 = k_i^2 - (\mathbf{K}_i + \mathbf{G})^2 = \frac{2m}{\hbar^2} E_n, \tag{51}$$

and, in the free atom approximation, E_n is the energy of an atom in the nth bound state of the laterally averaged potential, $V_0(z)$. If the surface is not strongly corrugated, the helium wavefunctions in the resonant state can be approximated as

$$\Psi_{(\mathbf{K}+\mathbf{G}),n}(\mathbf{R}, z) \approx \phi_n(z) \exp[i(\mathbf{K} + \mathbf{G}) \cdot \mathbf{R}], \tag{52}$$

where $\phi_n(z)$ is an eigenfunction of $V_0(z)$ and the **R** dependence is like that of a plane wave [165]. The length of time spent in the resonant state depends on the lateral corrugation of the potential since that controls the strength of the diffractive scattering. Both the time spent in the resonant state and the z-dependence of $\phi_n(z)$ make resonant scattering a useful experimental probe of the atom-surface potential. Resonances involving the ground state are most sensitive to the potential near the minimum, as this is where $\phi_0(z)$ has most weight, while the higher lying states, which extend further into the vacuum region, probe the shape of the potential at larger values of z.

Many experimental studies and most of the early calculations used approximations, such as Eq. (52), in order to simplify the analysis. Potentials derived in that way are necessarily approximate and the bound-state energies are known to be systematically misplaced [166]. The full picture is more analogous to a 2D band structure of nearly-free particles arising from the periodic corrugation of the surface-potential. Each bound state in the laterally averaged potential gives rise to a 2D sub-band within the overall band structure. With increasingly powerful computational tools there is less need to rely on a free-atom approximation and it is possible to solve the elastic scattering problem exactly. Time-dependent approaches, such as wavepacket propagation [167–169], and time-independent methods, such as close coupling [69,170–173], have been used with 1D and 2D corrugated surfaces. While the close-coupling method is often most practical and convenient, the wavepacket approach provides particularly helpful insights. The scattering process is illustrated in Fig. 19 from a quantum mechanical viewpoint, using an exact wavepacket calculation in a weakly corrugated 1D Morse potential [174]. The scattering is at normal incidence and the conditions are chosen to give five open channels, $G = 0, \pm 1, \pm 2$, as well as satisfying the resonance condition (Eq. (51)) for the ground state, $\phi_0(z)$, of the laterally averaged potential. The plots show the z-dependence of the scattered wavepacket, over a period of 2 ps after the wavepacket has scattered from the potential. The directly scattered fraction is evident from the majority intensity in the open channels, which can be seen moving to the right, from 10 Å < z < 40 Å, in (a), to 30 Å < z < 70 Å in (b). The resonantly scattered component is a minority component that may be seen, fixed, at the left of both figures (z < 5 Å). Notice that the z-dependence of the wavefunction in the resonant state (magnified in the inset to (b)) has the form expected for $\phi_0(z)$, as in Eq. (52), which confirms the assignment of the resonant scattering as arising from coupling to the ground state. As t increases, the intensity leaks from the resonant state, which may be seen from
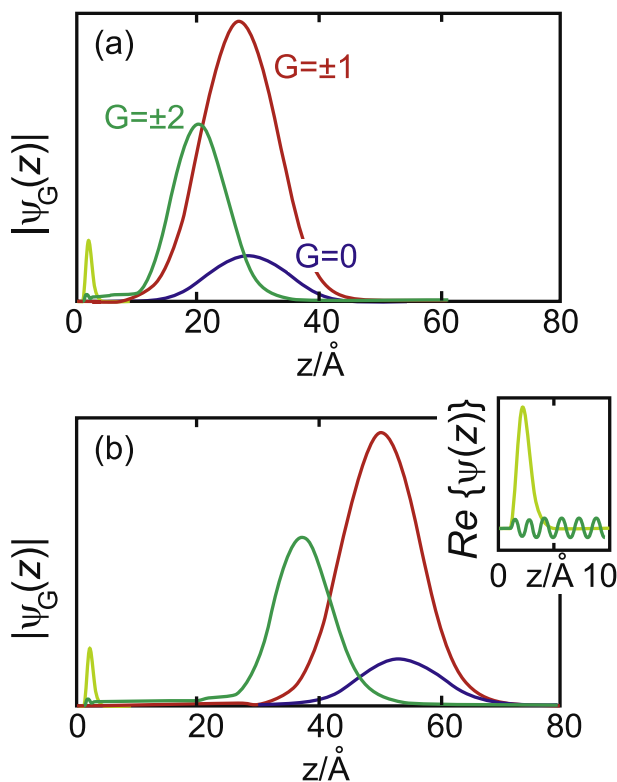
Fig. 19. Illustration of a Gaussian wavepacket after scattering, at normal incidence, from a 1D corrugated Morse potential located at the left of the figure, from [174]. The curves show the wavepacket projected onto particular open or closed diffraction channels and are labeled accordingly. Panel (a) corresponds to a time, $t = 4$ ps, shortly after the majority of the wavepacket has scattered from the surface, while panel (b) shows events slightly later, at $t = 6$ ps. Direct scattering into the open channels is evident form the three, large components, which all move to the right, away from the surface. The small resonantly scattered fraction is located at a fixed $z < 5$ Å. In (b), the inset shows a magnified view of the real part of the wavefunction in the region of the resonantly scattered fraction. From the z-dependence, it is evident that the resonant channel is associated with the ground vibrational state, $\phi_0(z)$, of the laterally averaged potential.

the slightly smaller magnitude of the resonant component at the later time, in panel (b). The leakage occurs with a characteristic lifetime that determines the linewidth of the resonance profile [69,167]. It also follows that, relative to the incoming wavepacket, the trailing edge of the emerging wavepacket is extended significantly during the process of scattering.

The two key properties that may be observed during resonant scattering are the kinematic conditions giving rise to a particular resonance, and the resonance lineshape. In general, the resonance conditions give information on the energy of the resonant state and hence, in the weak corrugation limit, the z-dependence of the laterally averaged potential, while the lineshape provides information about the corrugation [69,54,165]. Taken together, these offer one of the most precise sources of information about physisorption potentials [175]. The great majority of experiments have concentrated on measuring resonance positions in order to determine an effective, laterally averaged potential [69,165,175]. However, significant theoretical effort has been devoted to understanding resonance lifetimes and their relation to experiment [69,176,177].

The ease with which information can be extracted from resonant scattering data depends on the magnitude of the corrugation. In the semi-classical picture (Fig. 3), the strength of diffractive scattering both into and out of the resonant state is determined by the surface corrugation. Thus, as the corrugation increases, the resonances become stronger, as more of the incident wave scatters into the

resonant state, while becoming simultaneously broader, as the resonance lifetime decreases through stronger scattering out of the resonant state. In addition, a larger corrugation leads to a greater deviation from the free-atom analysis (Eqs. (51) and (52)) so that, in an experiment, it becomes more difficult to identify energies of the states in the laterally averaged potential. Indeed, for large corrugation, the value of the concept of eigenstates in a laterally averaged potential becomes questionable, as we demonstrate below.

Analysis of resonant scattering is also affected by the dimensionality of the corrugation. In the free-atom limit, where the corrugation becomes vanishingly small, the density of resonant states is given by standard formulae. Thus, the density of resonant states for a 1D corrugation decreases strongly with incident energy, $g(E_i) \sim 1/(E_i - E_n)$ for the nth sub-band, while the density of states in 2D is constant and independent of the incident energy. One-dimensional problems, such as stepped and fcc (1 1 0) surfaces [69,167,178], have a simple band structure for the resonant states. The number of open channels that couple to the resonant states is limited, so there is little ambiguity over the assignment of resonances. Furthermore, since the density of resonant states decreases with incident energy it is usually possible to find conditions where resonance features are well separated. Both experiment and calculation are relatively straightforward. The situation for a system that is corrugated in 2D is less auspicious. There are many more open channels and, since the density of resonant states is approximately constant, it is difficult to find energy windows where isolated resonances can be observed, and more difficult still to find kinematic conditions where resonant scattering plays no role. These effects are apparent in recent wavepacket calculations for 2D potentials [168,169] where all of scattering conditions show a resonant component in the scattering. From an experimental perspective, systems having a large, 2D corrugation present significant difficulties in interpretation since the resonances are broad and overlap, as well as showing strong deviation from simple free-atom like dispersion [173].

Overall, in order to study corrugated 2D systems accurately, large amounts of high resolution, high quality data are required. Fortunately, such data can be provided by the Fourier transform scattering technique described below.

7.2. Fourier transform atom spectroscopy

In a conventional SAR experiment [54], there are three variables; the incident energy, E_i, together with the polar and azimuthal scattering angles, θ_i and ϕ_i. Typically, the energy and polar angles are fixed while the azimuth is varied, or the angles are fixed while the energy is varied. Energy analysis of the scattered beam is not usually applied. In both cases the resulting data represents a single slice through the energy-angle space. In both types of experiment, the data is limited by the energy spread in the incident beam and the angular resolution of the apparatus. Since resonances can have sub-meV width, the effect is to broaden and obscure narrow resonance features so that in general, only strong, broad resonances have been observed. Curiously, this effect did not affect the very first observations of resonant scattering [57], where systematic intensity variations within diffraction peaks were observed. Here, the dispersive effects of the crystal itself helped to overcome the energy spread limitations. For diffraction peaks rather than the specular peak, collimation can be used to define an effective energy resolution that is better than the spread of energies within the beam. The same technique was employed recently to obtain resonance positions in the predominantly 1D system Ne/Cu(1 1 0) [178].

The recently developed alternative technique, referred to as Fourier transform helium atom spectroscopy (FT-HAS) [172,173,179], takes a different approach. Here, the spread of energies in the incident beam is broadened as far as possible, then spin-precession in a single coil of the spin-echo apparatus is used to analyse the energy distribution in the beam, providing energy dependent reflectivity information. Within the tilted projection framework (see Section 3.3), such measurements correspond to projections angles of either 0 or 90°, depending on whether the distribution is analysed before or after scattering, respectively.[3] In either case, as given by Eqs. (29) and (30), the spin-phase

---

[3] Inelastically mediated selective adsorption processes can affect the total scattering angle of helium atoms with certain energies, leading to additional small differences in the measured energy distribution obtained using the incoming or outgoing coils [180].

accumulated by a particular atom in the precession coil is given by $\phi = C\lambda I$ and the subsequent beam averaged polarisation measurement, as a function of current in the relevant precession coil, I, corresponds to the Fourier transform of the distribution of wavelengths in that solenoid, $\rho(\lambda)$,

$$P(I) = \int \rho(\lambda) \exp(2\pi i C\lambda I)d\lambda. \tag{53}$$

Hence, a single coil polarisation measurement, $P(I)$, simultaneously provides information at all the resonance conditions that are 'illuminated' by the energies in the incident beam, for the particular value of the scattering angles used.

Fourier transform atom spectroscopy has a number of advantages compared with conventional experiments. First, the energy resolution is unaffected by the spread in the incident beam, so that line-shapes can be recovered without recourse to dispersive scattering. Secondly, the Fourier-transform method ensures that a wide range of incident energies can be studied at once, which produces large datasets covering a correspondingly wide range of kinematic conditions. Finally, the new method has the advantage, implicit in any Fourier spectroscopy, that since all components in the spectrum are measured simultaneously, the data taking time depends on the required spectral resolution, rather than the spectral range. In fact, FT-HAS is directly analogous to optical techniques such as Fourier transform infra-red spectroscopy (FTIR), in which sharp adsorption bands in the transmission of the reflectivity of a sample can be obtained both quickly and with high resolution [181].

As with the conventional spin-echo experiment, we can also consider the FT-HAS experiment from a quantum viewpoint. The principle is analogous to the behavior of a Michelson interferometer in conventional optics [182]. As before (Section 3.2), the magnetic field splits the helium atom wavepackets into two spin components and, simultaneously introduces controlled phase shifts, or equivalently time delays, τ, between them. However, in a single coil experiment, the components are not recombined. Instead, the two components superpose directly at the detector, where the observed signal provides a measurement of the correlation between the two wavepackets, as a function of the relative time delay, τ. The correlation measurement has a Fourier relationship with the spectral distribution, as given by the Wiener–Khintchine theorem [182], hence providing the same information as before.

The changes occurring in the profile of the wavepacket during resonant scattering help to visualise the SAR measurement from a quantum interference viewpoint. Fig. 20 shows the experiment schematically. Here, a Gaussian wavepacket, incident from the left, is split into its two spin-components. The components are separated, along the beam axis, by a time, τ, so that, in general, there is no longer any overlap between the components. If a resonant state becomes populated during the scattering event, the extension of the trailing edge of the wavepacket through leakage from the resonant state allows the modified wavepackets to overlap and interfere, as shown in the outgoing beam. Thus, the interference pattern as the time delay, τ, is varied relates directly to the lifetime of the resonant
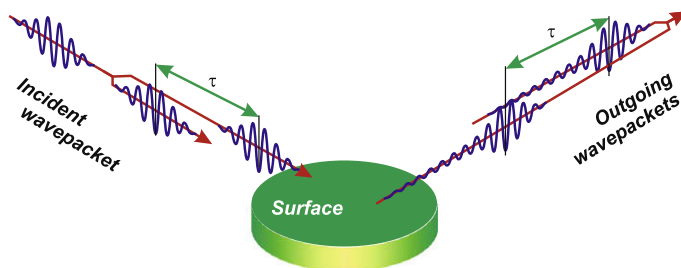

Fig. 20. Illustration of resonant scattering in Fourier transform atom spectrometry. The incident wavepacket is split into its two spin-components and separated longitudinally by time, τ, which may be longer than the coherence time of the incident beam. Note that the two spin-components take a collinear path throughout the experiment but, for clarity, they have been separated laterally in the diagram. On the outgoing leg, the two components retain their longitudinal separation but now overlap, and interfere, due to the extended trailing edge caused by leakage from the resonant state populated in the scattering (see text). The splitting and shifting of the wavepacket does not need to be done before scattering, as shown, but may equally be performed after surface scattering.

state and the observed lifetime is independent of the energy spread in the incident beam, provided the kinematic conditions to excite the resonant state are satisfied.

7.3. Experimental determination of the helium-surface potential using FTHAS

We illustrate the above principles in the context of two recent FT-HAS studies. The systems (LiF(001) [172] and Si(111)–(1 × 1)H [179]) have certain aspects in common; both surfaces are non-metallic with comparable magnitude to the corrugation in the repulsive part to the potential (∼0.6 Å) and the corrugation in both cases is two-dimensional. Differences evident in the results demonstrate the value of measurements where the lineshape of the resonance, as well as the position of the resonance are measured.

The LiF(001) surface was the first surface on which helium diffraction was observed and it has been studied extensively since those early experiments [165]. The best existing theoretical potentials for He–LiF(100), as well as for other systems, are based on summed pair potentials and, if one ignores a relative shift in the origins of the two potentials, the differences between alternative formulations are slight [171,183,184]. In a Fourier transform of these potentials, the dominant terms are also the lowest order terms ({01}, {10}) and a feature of both potentials is that the corrugated terms decay strongly away from the surface so that they are only significant at short-range and are negligible beyond the minimum in the laterally averaged potential. In other words these potentials follow the common prescription of having a strongly corrugated wall and a weakly corrugated well.

Experimental FT-HAS results [172], are reproduced in Fig. 21a, where the specular intensity is shown as a colour map plotted against incident energy, E_i, and azimuthal angle, ϕ. The results show
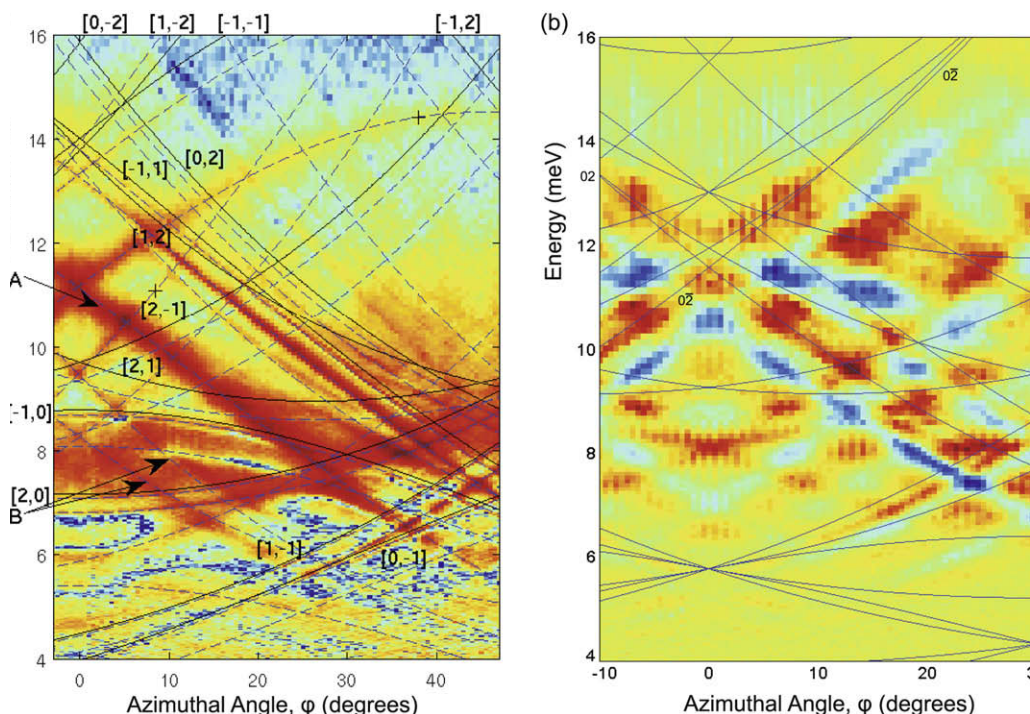

Fig. 21. Experimental Fourier transform helium atom spectroscopy results for (a) ^{3}He–LiF(100), from [172] and (b) ^{3}He–Si(111)–(1 × 1)H, from [179]. Scattered intensity is shown in colour (red/blue corresponding to high/low intensities, respectively) as a function of azimuthal angle and helium energy. The data for LiF(100) shows a large number of narrow selective adsorption resonances, while in the case of Si(111)–(1 × 1)H there are fewer, much broader resonances. (For interpretation of the references to colour in this figure legend, the reader is referred to the web version of this article.)

a large number of sharp resonant features that disperse strongly across the plot and many can be related directly to the various diffraction thresholds, which are shown as solid lines in the plot. In general, the resonances behave as expected. Those lying just below a threshold are narrow, since the majority of the weight in the bound state wavefunction, $\phi_n(z)$ in Eq. (52), lies well away from the repulsive wall and so couples weakly to the lateral corrugation. Hence they have a long lifetime and a narrow width in energy. In contrast, the lower lying states are broader, reflecting greater coupling to the repulsive corrugation. Although there are a large number of features, they can usually be identified as isolated resonances and, in general, it is obvious whether a feature is a maximum or a minimum. Comparison with scattering calculation using the theoretical potentials showed a good degree of agreement, both in the resonance positions and in the line-shapes (maxima or minima). The detail in the experimental spectra have allowed small but significant modifications to be made to the theoretical potentials to give an optimised empirical potential for this system [172].

The case of Si(1 1 1)–(1 × 1)H is quite different [179]. Data from Fourier transform atom spectroscopy measurements are shown in Fig. 21b. Again, the solid lines show all the diffraction thresholds for the system. What is immediately obvious in comparing the LiF(0 0 1) data (Fig. 21a) with the Si(1 1 1)–(1 × 1)H results (Fig. 21b) is that the resonances in Si are fewer in number and much broader in energy. The energy width of the measured resonances greatly exceeds the experimental resolution and so cannot be attributed to an artifact of the measurement. Resonant features lying just below a threshold are as broad as more deeply lying states, unlike the behavior in LiF, and it is difficult to attribute features to isolated resonances. An earlier potential [185], based on a diffraction analysis combined with low-resolution measurements of resonances, does not reproduce the new data at a quantitative level. The calculated resonances are larger in number and much narrower in energy. Differences between the new data and predictions from the existing potential have been attributed to the differences in the range of the corrugated terms in the potential. The existing potential [185] has similar characteristics to the LiF potential in that the corrugation decays strongly away from the surface and is negligible in the region of the well. In contrast, the new data indicates a potential whose corrugation extends much further into the region of the well.

The difference between the observed resonances in LiF and those Si(1 1 1)–(1 × 1)H indicates that the two atom-surface potentials have a radically different character. It is not simply a case of minor changes to the depth or shape of the laterally averaged potential. The differences are much more profound and demonstrate the importance of high resolution measurements, where there can be no ambiguity about the lineshape, and where the dataset covers a sufficient range of energies and angles to identify features uniquely.

7.4. Quantum reflection at the helium-surface potential

Recently, the Heidelberg spin-echo apparatus has been applied to measurements of quantum reflection of helium atoms by the attractive potential at an α-quartz surface [186]. The technique demonstrates grazing incidence measurements can be used to provide information about the helium-surface potential at distances of some tens of Angstroms above the surface. Their analysis provides a quantitative information and suggests that the interaction potential near the surface falls off more quickly than a pure van der Waals potential. For these measurements, as with the selective adsorption measurements described above, the spin-echo technique is used to provide a very precise way of determining the energetic properties of the beam.

8. Summary and outlook

In this review, we have set out the way in which the helium-3 spin-echo (^{3}HeSE) technique has been used dramatically to increase the resolution available in a wide range of helium scattering experiments. We have described the technique, its implementation and application in some detail. ^{3}HeSE provides a general purpose method which can be applied to elastic, inelastic and quasi-elastic processes. Its main application has been to revolutionise quasi-elastic helium atom scattering (QHAS) experiments. The first measurements using the QHAS technique, carried out using time of flight

(TOF) instrumentation, were published about 20 years ago. Then, the instrumental resolution of ~0.3 meV limited measurements to a few extremely fast moving systems. Analysis required a line-shape to be assumed and made it impossible to distinguishing between more than one dynamical process in the data.

Today, the Cambridge ^{3}HeSE instrument can perform measurements on length-scales between about 1.5 Å and 100 Å, with an effective resolution of ~1 μeV, corresponding to timescales as long as 1 ns. The Heidelberg instrument has a resolution over 10 times higher again, but is restricted to longer length-scales. With these tremendous improvements in resolution, a much wider range of physical processes can be studied, including dynamical processes with a number of distinct time scale contributions. The scientific output of ^{3}HeSE measurements to date fall under a convenient series of headings:

1. **Mechanisms of surface diffusion** can now be clearly elucidated, by using the momentum transfer dependence of the QHAS dephasing rate to study atomic scale motion on nanosecond to picosecond timescales. A range of previously unidentified phenomena have been clearly distinguished, ranging from single and multiple jump distributions to Brownian and ballistic regimes.
2. **Experimentally determined potential energy surfaces** have been constructed for several systems by using a combination of QHAS data and MD analysis. These potentials provide a detailed description of the dynamics of a system and give insights into the controlling factors. Empirical potentials provide excellent benchmark data for evaluating first principle calculations [152,30], such as density functional theory (DFT). DFT has become a widely used tool for modeling behavior at surfaces, but it is widely accepted that there are important systematic errors which are affected by, for example, the choice of functionals. We hope the rapidly expanding body of experimental PESs available for systematic comparison with theory will spur further developments of first principle methods.
3. **Adsorbate–surface 'friction'** otherwise known as the rate of adsorbate–substrate energy transfer, has a controlling effect on the dynamics of surface species. QHAS data enables meaningful surface average friction parameters to be evaluated for a wide range of adsorbed species. Such measurements relate closely to ongoing efforts in the nanotribology community. While most nanotribological measurements focus on the static friction, QHAS provides the associated frictional damping term, at the individual molecule level. Only a few theories of adsorbate–substrate friction currently exist [187] which give limited agreement with experiment. Here, we also hope the availability of reliable friction data should stimulate theoretical work on the poorly understood area of adsorbate–substrate energy transfer rates.
4. **Interactions between adsorbed species** can be obtained from analysis of correlation features. ^{3}HeSE data yields a uniquely direct measure of interaction forces on the atomic scale, unlike all other techniques which must make considerable assumptions about the underlying force mechanism, in order to utilise macroscopic data. New results have both supported existing force models [130] and shown others to be completely inappropriate [135].
5. **Ultra high resolution inelastic measurements** can be obtained by optimising spin-echo measurements using the tilted-projection formulation. These measurements provide a high resolution/ low energy compliment for TOF phonon measurements and enable both the determination of very low energy phonon and adsorbate dispersion curves, and allow low energy linewidths to be extracted with high precision, giving invaluable information on the vibrational mode lifetimes.
6. **Precision energy profiles** of the energy distribution in scattered helium beams allows selective adsorption resonance (SAR) processes to be studied, and is useful for quantum scattering experiments. SAR measurements enable the shape of the attractive part of the helium-surface potential to be established with astonishing precision. The helium-surface potential is fundamental to the scattering process and when combined with diffraction data, resonance data provides the most precise empirical approach to realistic potential construction.

In each of these areas, important new advances have been made. However, we should also point out that since ^{3}HeSE is a reciprocal space technique, additional information about the nature of the mobile species is crucial. As experiments progress to more complex systems, we expect this issue

to become progressively more important in the future. As described in Section 2, conventional helium scattering experiments provide considerable structural information, as does information from other 'traditional' surface probes. One approach of particular note, which we expect to become progressively more important, is the combined use of HeSE and STM imaging, since STM experiments provide complimentary real space and long timescale information.

8.1. Towards future instrumentation

The scientific advances described in this review have been driven by the development of new forms of instrumentation. We therefore look towards the scope for further instrumentation advances in the future. There are two key factors that limit the performance of any spin-echo measurement, the maximum spin-echo time available (corresponding to the energy resolution) and the available signal level.

The spin-echo time can be increased by either increasing the magnetic field integral of the spin-echo coils or by reducing the beam energy. Since the spin-echo time scales with beam energy, E, as $E^{-3/2}$, while momentum transfer scales as $E^{1/2}$, a relatively small change in beam energy can provide a substantial improvement in resolution. Operation at an energy intermediate between the Cambridge and Heidelberg instruments would therefore give significantly higher resolution, with only a small reduction in momentum transfer. Given the basic coil construction described in Section 4, heat dissipation limits the field to 0.15 T for continuous operation. Pulsed operation could allow twice this field to be achieved. Longer coils could also provide up to about a fivefold increase in resolution, although an order of magnitude reduction in signal would have to be accepted, due to $r^{-1/2}$ losses in the scattered beam. Between these factors, an improvement in resolution of up to about 30 is reasonably achievable using the basic design principles already established, with only a 40% reduction in momentum transfer range. However, to go beyond this level would likely require a different design concept.

As described in Section 4, new approaches for detection are continually underway [120,122], making use of the fact that spin-echo experiments do not require high temporal resolution. We expect a substantial improvement in detection efficiency, which will improve the rate of measurement, increase the *useful* momentum transfer range (since diffuse scattered intensity drops off rapidly with increasing momentum transfer), and should be able to offset the possible losses described above. Improved detector sensitivity is central to the development of both the energy and momentum transfer capabilities of the spin-echo technique.

We can also look towards the techniques being developed for the more established field of neutron spin-echo (NSE). Superconducting solenoids provide an opportunity to achieve much stronger magnetic fields, although also pose additional difficulties due to flux-trapping, causing hysteresis [99]. Additionally, the strong fields used in neutron spin-echo require aberration correction coils, which are standardly placed in the beamlines of NSE instruments. Unfortunately, since helium atoms can only travel through a vacuum, such correction coils are not possible in the case of ^{3}HeSE. Currently, NSE has a major focus on developing wide angle techniques [97]. Whilst an in vacuo implementation would be challenging, they indicate the benefits of parallel data acquisition, for example using multiple outgoing arms. Other NSE techniques such as the concept of resonance spin-echo and time-dependent coils may also find surface scattering analogies in the future [96].

8.2. Prospects for dynamical analysis

To date, the analysis of QHAS data has been based almost entirely on theory and simulations within the kinematic scattering approximation (Eq. (7)). For isolated adsorbate species, the assumption is reasonable, especially for close-packed metal surfaces which appear flat to helium atoms. However, at higher coverages the situation is less clear. Comparative experiments with NSE [87] (where the kinematic approximation is reliable) suggest the kinematic approximation is still good at around 0.5 ML, even with large species. However, full quantum mechanical scattering calculations from a fully mobile surface will provide the most rigorous route for analysis. Calculations with enough adsorbate species

to correctly represent the adsorbate dynamics will be extremely demanding, but represent an exciting prospect for the future.

Since the spin-echo technique measures in reciprocal space, it is inevitable that interpreting the experimental data will require a fair degree of modeling. Usually, analytic theory is used as far as possible, supported by MD simulations, as discussed in Section 5. As a wider range of experimental data becomes available, the need for more sophisticated analytic theory increases steadily. We hope the range of measurements will stimulate new work. For example, analytically reproducing the characteristics of 2D correlated motion would be of considerable importance in order to identify adsorbate–adsorbate interaction models.

As more complex adsorbates are studied at higher resolution, longer and more complex MD simulations will be required. Current simulations run conveniently on computing resources commonly available. However, with increasing system complexity, they will quickly become prohibitive. As simulations become more complex, it also becomes harder to ensure a unique fit to the data. Both these issues will have to be addressed by the development of new, possibly cruder yet still meaningful simulation techniques, which will need to be combined with a better developed understanding of the characteristic signatures of complex processes.

8.3. Future physical challenges

So far, ^{3}HeSE experiments have mainly concentrated on simple species moving on a few relatively well understood metal surfaces. Without doubt, in the near future there will be substantial further development of the six themes of measurement described above. The established aims are be to extend the body of empirical knowledge about diffusion at surfaces, given a much richer range of behavior has already been observed than simple theory would predict. There is already considerable interest in examining the generality of the novel phenomena seen in both the alkali metal systems and CO systems, on a range of other materials and surfaces. We also expect a number of general trends:

- There is already a trend towards **larger and more complex systems**. These will include larger, more complex molecules with more internal and external degrees of freedom, and more complicated substrates, ranging from simple asymmetric surfaces like the fcc (1 1 0), to stepped surfaces and even artificially nanostructured geometries.
- Developing techniques to distinguish systems exhibiting **multiple dynamical characteristics** is likely to prove important, for example in complex systems where several internal modes, rotation and translation may all occur.
- **Delicate surface systems** are likely to be of considerable interest. These will likely include insulators, many of which require specialist preparation, weakly bound species which will require particularly low substrate temperatures and easily damaged species such as water, which are difficult to study using conventional spectroscopies.
- At present, most ^{3}HeSE studies have concentrated on individual adsorbate systems. In the future, we expect more **comparative studies**, which will enable physical trends between similar species to be understood. Although mundane, simple advances in instrumentation such as sample-transfer are likely to have a major impact on such work.

Overall, current ^{3}HeSE experiments have barely touched on the range of novel phenomena in this hitherto unstudied regime of atomic length and pico- to nano-second timescale dynamics. Between the possibilities for advancement of instrumentation, the huge scope for further development and testing of both dynamical and first principles total energy theory, and the immense range of experimental studies which can be pursued, we expect there to be a long and productive future for this field.

Acknowledgement

References

[1] D.P. Woodruff, T.A. Delchar, Modern Techniques of Surface Science, Cambridge University Press, 1986.
[2] Y.J. Chabal, Surf. Sci. Rep. 8 (1988) 211.
[3] H. Ibach, Surf. Sci. 299/300 (1994) 116.
[4] G. Comsa, Surf. Sci. 299/300 (1994) 77–91.
[5] G. Benedek, J.P. Toennies, Surf. Sci. 299–300 (1994) 587.
[6] J.V. Barth, Surf. Sci. Rep. 40 (2000) 75.
[7] R. Gomer, Rep. Prog. Phys. 53 (1990) 917.
[8] P. Hänggi, P. Talkner, M. Borkovec, Rev. Mod. Phys. 62 (1990) 251.
[9] A. Fick, Ann. Phys. 59 (1855) 170.
[10] A.G. Naumovets, Y.S. Vedula, Surf. Sci. Rep. 4 (1985) 365.
[11] E.G. Seebauer, L.D. Schmidt, Chem. Phys. Lett. 123 (1986) 129.
[12] G.L. Kellog, Surf. Sci. Rep. 21 (1994) 1.
[13] H. Brune, Surf. Sci. Rep. 31 (1998) 121.
[14] D.A. King, J. Vac. Sci. Technol. 17 (1980) 241.
[15] T. Ala-Nissila, R. Ferrando, S.C. Ying, Adv. Phys. 51 (2002) 949.
[16] S. Miret-Artes, E. Pollak, J. Phys.: Condens. Matter 17 (2005) S4133.
[17] T. Ala-Nissila, S.C. Ying, Prog. Surf. Sci. 39 (1992) 227.
[18] H. Risken, The Fokker–Planck Equation, Springer, Berlin, 1989.
[19] D.C. Rappaport, The Art of Molecular Dynamics Simulations, Cambridge University Press, 1995.
[20] M.P. Allen, D.J. Tildesley, Computer Simulation of Liquids, Oxford University Press, 1987.
[21] R. Ferrando, R. Spadacini, G.E. Tommei, Surf. Sci. 265 (1992) 273.
[22] L.Y. Chen, M.R. Baldan, S.C. Ying, Phys. Rev. B 54 (1996) 8856.
[23] R. Ferrando, R. Spadacini, G.E. Tommei, Phys. Rev. E 48 (1993) 2437.
[24] J.L. Vega, R. Guantes, S. Miret-Artes, Phys. Chem. Chem. Phys. 4 (2002) 4985.
[25] R. Kubo, Rep. Prog. Phys. 29 (1966) 255.
[26] F. Hofmann, J.P. Toennies, Chem. Rev. 96 (1996) 1307.
[27] A.P. Graham, F. Hofmann, J.P. Toennies, L.Y. Chen, S.C. Ying, Phys. Rev. Lett. 78 (1997) 3900.
[28] A.P. Graham, F. Hofmann, J.P. Toennies, G.P. Williams, C. Hirschmugl, J. Ellis, J. Chem. Phys. 108 (1998) 7825.
[29] A.P. Graham, J.P. Toennies, Europhys. Lett. 42 (1998) 449.
[30] G. Alexandrowicz, A.P. Jardine, P. Fouquet, S. Dworski, W. Allison, J. Ellis, Phys. Rev. Lett. 93 (2004) 156103.
[31] E.H.G. Backus, A. Eichler, A.W. Kleyn, M. Bonn, Science 310 (2005) 1790.
[32] R. Martinez-Casado, J.L. Vega, A.S. Sanz, S. Miret-Artes, Phys. Rev. Lett. 98 (2007) 216102.
[33] R. Martinez-Casado, J.L. Vega, A.S. Sanz, S. Miret-Artes, Phys. Rev. E 75 (2007) 051128.
[34] R. Martinez-Casado, J.L. Vega, A.S. Sanz, S. Miret-Artes, J. Phys.: Condens. Matter 19 (2007) 305002.
[35] R. Martinez-Casado, J.L. Vega, A.S. Sanz, S. Miret-Artes, Phys. Rev. B 77 (2008) 115414.
[36] R. Ferrando, R. Spadacini, G. Tommei, Phys. Rev. A 46 (1992) R699.
[37] O.M. Braun, R. Ferrando, Phys. Rev. E 65 (2002) 061107.
[38] A. Cucchetti, S.C. Ying, Phys. Rev. B 54 (1996) 3300.
[39] R. Metzler, J. Klafter, J. Phys. A: Math. Gen. 37 (2004) R161.
[40] G. Ehrlich, Surf. Sci. 299/300 (1994) 628.
[41] C.M. Yim, K.L. Man, X. Xiao, M.S. Altman, Phys. Rev. B 78 (2008) 155439.
[42] J. Zhao, S. Granick, Macromolecules 40 (2007) 1243.
[43] M.J. Rost, D.A. Quist, J.W.M. Frenken, Phys. Rev. Lett. 91 (2003) 026101.
[44] E. Wahlstrom, E.K. Vestergaard, R. Schaub, A. Ronnau, M. Vestergaard, E. Laegsgaard, I. Stensgaard, F. Besenbacher, Science 303 (2004) 511.
[45] X. Xiao, Y. Xie, Y.R. Shen, Surf. Sci. 271 (1992) 295.
[46] Y.Y. Yeo, L. Vattuone, D.A.J. King, Chem. Phys. 106 (1997) 392.
[47] H.H. Rotermund, Surf. Sci. Rep. 29 (1997) 265.
[48] A. Kubo, N. Pontius, H. Petek, Nano Lett. 7 (2007) 470.
[49] A. Krasyuk, A. Oelsner, S.A. Nepijko, A. Kuksov, C.M. Schneider, G. Schonhense, Appl. Phys. A 76 (2003) 863.
[50] M. Bee, Quasielastic Neutron Scattering, IOP Publishing, Bristol, 1988.
[51] T. Engel, K.H. Rieder, Springer Tracts in Modern Physics, vol. 91, Springer-Verlag, 1982.
[52] B. Poelsema, G. Comsa, Scattering of Thermal Energy Atoms, Springer, 1989.
[53] E. Hulpke (Ed.), Helium Atom Scattering from Surfaces, Springer-Verlag, 1992.
[54] D. Farías, K.-H. Rieder, Rep. Prog. Phys. 61 (1998) 1575.
[55] J.P. Toennies, Appl. Phys. 3 (1974) 91.
[56] David R. Miller, in: G. Scoles (Ed.), Atomic and Molecular Beam Methods, vol. 1, Oxford University Press, 1988, pp. 14–53.
[57] R. Frisch, O. Stern, Z. Phys. 84 (1933) 430.
[58] R. Frisch, Z. Phys. 84 (1933) 443.
[59] A.P. Graham, A. Menzel, J.P. Toennies, J. Chem. Phys. 111 (1999) 1676.
[60] M.F. Luo, D.A. MacLaren, I.G. Shuttleworth, W. Allison, Chem. Phys. Lett. 381 (2003) 654.
[61] L. Casalis, M.F. Danisman, B. Nickel, G. Bracco, T. Toccoli, S. Iannotta, G. Scoles, Phys. Rev. Lett. 90 (2003) 206101.
[62] M.F. Danisman, L. Casalis, G. Scoles, Phys. Rev. B 72 (2005) 085404.
[63] A.W. Rosenbaum, M.A. Freedman, S.B. Darling, I. Popova, S.J. Sibener, J. Chem. Phys. 120 (2004) 3880.
[64] M.F. Danisman, L. Casalis, G. Bracco, G. Scoles, J. Phys. Chem. B 106 (2002) 11771.
[65] C. Wöll, Prog. Surf. Sci. 82 (2007) 55.
[66] M.T. Suter, P.U. Andersson, J.B.C. Pettersson, J. Chem. Phys. 125 (2006) 174704.
[67] P.U. Andersson, M.T. Suter, N. Markovic, J.B.C. Pettersson, J. Phys. Chem. C 111 (2007) 15258.

[68] J. Vogt, J. Chem. Phys. 126 (2007) 244710.
[69] A.S. Sanz, S. Miret-Artes, Phys. Rep. 451 (2007) 37.
[70] D. Kosloff, R. Kosloff, J. Comp. Phys. 52 (1983) 35.
[71] G. Wolken Jr., J. Chem. Phys. 58 (1973) 3047.
[72] S. Nave, D. Lemoine, J. Phys.: Condens. Matter 14 (2002) 6263.
[73] B.J. Hinch, Surf. Sci. 221 (1989) 346.
[74] J.P. Toennies, J. Vac. Sci. Technol. A 2 (1984) 1055.
[75] W. Kress, F.W. de Wette (Eds.), Surface Phonons, Springer-Verlag, Berlin, 1991.
[76] A.P. Graham, Surf. Sci. Rep. 49 (2003) 115.
[77] G. Witte, Surf. Sci. 502 (2002) 405.
[78] G. Alexandrowicz, A.P. Jardine, J. Phys.: Condens. Matter 19 (2007) 305001.
[79] J.W.M. Frenken, B.J. Hinch, Helium Atom Scattering from Surfaces, vol. 298, Springer-Verlag, Berlin, 1992 (Chapter 12).
[80] J.W.M. Frenken, J.P. Toennies, C. Wöll, Phys. Rev. Lett. 60 (1988) 1727.
[81] B.J. Hinch, J.W.M. Frenken, G. Zhang, J.P. Toennies, Surf. Sci. 259 (1991) 288.
[82] J. Ellis, J.P. Toennies, Phys. Rev. Lett. 70 (1993) 2118.
[83] J. Frenken, B. Hinch, Helium Atom Scattering from Surfaces, Springer-Verlag, Berlin, 1992 (Chapter 12).
[84] A.P. Jardine, J. Ellis, W. Allison, J. Phys.: Condens. Matter 14 (2002) 6173.
[85] L. Van Hove, Phys. Rev. 95 (1954) 249.
[86] P. Fouquet, H. Hedgeland, A.P. Jardine, Z. Phys. Chem., submitted for publication.
[87] P. Fouquet, H. Hedgeland, A.P. Jardine, G. Alexandrowicz, W. Allison, J. Ellis, Physica B 385 (2006) 269.
[88] A.P. Jardine, J. Ellis, W. Allison, J. Chem. Phys. 120 (2004) 8724.
[89] Q. Ge, D.A. King, J. Chem. Phys. 111 (1999) 9461.
[90] A.P. Graham, J.P. Toennies, J. Chem. Phys. 114 (2001) 1051.
[91] Q. Ge, D.A. King, J. Chem. Phys. 114 (2001) 1053.
[92] A.P. Graham, J.P. Toennies, J. Phys. Chem. B 105 (2001) 4003.
[93] M. Ondrejcek, W. Stenzel, H. Conrad, V. Chab, Z. Chvoj, W. Engel, A.M. Bradshaw, Chem. Phys. Lett. 215 (1993) 528.
[94] Ralf Kunkel, Bene Poelsema, Laurens K. Verheij, George Comsa, Phys. Rev. Lett. 65 (1990) 733.
[95] F. Mezei (Ed.), Neutron Spin Echo, Lecture Notes in Physics, vol. 128, Springer-Verlag, 1980.
[96] F. Mezei, C. Pappas, T. Gutberlet (Eds.), Neutron Spin Echo Spectroscopy: Basics, Trends and Applications, Springer-Verlag, Heidelberg GmbH & Co., Berlin, 2002.
[97] P. Fouquet, G. Ehlers, B. Farago, C. Pappas, F. Mezei, J. Neutron Res. 15 (2007) 39.
[98] M. Ohla, M. Monkenbusch, D. Richter, C. Pappas, K. Lieutenant, T. Krist, G. Zsigmond, F. Mezei, Physica B 350 (2004) 147.
[99] W. Walter, M. Borlein, F. Eyßelein, M. Gehring, T. Kozielewski, A. Kramer, M. Monkenbusch, M. Ohl, A. Paul, B. Schrauth, C. Tiemann, IEEE Trans. Appl. Supercond. 17 (2007) 1209.
[100] M. DeKievet, D. Dubbers, C. Schmidt, D. Scholz, U. Spinola, Phys. Rev. Lett. 75 (1995) 1919.
[101] M. DeKievet, D. Dubbers, M. Klein, C. Schmidt, M. Skrzipczyk, Surf. Sci. 377–379 (1997) 1112.
[102] F. Mezei, Neutron Spin-echo, vol. 3, Springer-Verlag, 1980 (Chapter 1).
[103] R. Gähler, R. Golub, K. Habicht, T. Keller, J. Felber, Physica B 229 (1996) 1.
[104] G. Alexandrowicz, Helium Spin Echo Spectroscopy: Measuring the Dynamics of Atoms, Molecules and Surfaces, PhD thesis, University of Cambridge, 2005.
[105] A.P. Jardine, G. Alexandrowicz, H. Hedgeland, R.D. Diehl, W. Allison, J. Ellis, J. Phys.: Condens. Matter 19 (2007) 305010.
[106] A. Steinhof, Nucl. Instrum. Meth. Phys. Res. A 397 (1997) 371.
[107] P. Fouquet, A.P. Jardine, S. Dworski, G. Alexandrowicz, W. Allison, J. Ellis, Rev. Sci. Instrum. 76 (2005) 053109.
[108] A.P. Jardine, P. Fouquet, J. Ellis, W. Allison, Rev. Sci. Instrum. 72 (2001) 3834.
[109] S. Dworski, G. Alexandrowicz, P. Fouquet, A.P. Jardine, W. Allison, J. Ellis, Rev. Sci. Instrum. 75 (2004) 1963.
[110] K. Halbach, Nucl. Instrum. Meth. 169 (1980) 1.
[111] C.M.E. Zeyen, P.C. Rem, Meas. Sci. Technol. 7 (1996) 782.
[112] H. Hedgeland, P.R. Kole, W. Allison, J. Ellis, A.P. Jardine, Rev. Sci. Instrum. 80 (2009) 076110.
[113] H. Hedgeland, A.P. Jardine, W. Allison, J. Ellis, Rev. Sci. Instrum. 76 (2005) 123111.
[114] D. Bassi, Atomic and Molecular Beam Methods, vol. 1, Oxford University Press, New York, 1988.
[115] M. Faubel, W.M. Holber, J.P. Toennies, Rev. Sci. Instrum. 49 (1978) 449.
[116] K.M. Martini, W. Franzen, M. El-Batanouny, Rev. Sci. Instrum. 58 (1987) 1027.
[117] C.C. Hayden, S.M. Penn, K.K. CarlsonMuyskens, F.F. Crim, Rev. Sci. Instrum. 61 (1990) 775.
[118] K. Kuhnke, K. Kern, R. David, G. Comsa, Rev. Sci. Instrum. 65 (1994) 3458.
[119] A. Amirav, A. Fialkov, A. Gordin, Rev. Sci. Instrum. 73 (2002) 2872.
[120] M. DeKievet, D. Dubbers, M. Klein, U. Pieles, C. Schmidt, Rev. Sci. Instrum. 71 (2000) 2015.
[121] A.V. Kalinin, L.Y. Rusin, J.P. Toennies, Instrum. Exp. Tech. 49 (2006) 709.
[122] A.R. Alderwick, A.P. Jardine, H. Hedgeland, D.A. MacLaren, W. Allison, J. Ellis, Rev. Sci. Instrum. 79 (2008) 123301.
[123] G.H. Vineyard, Phys. Rev. 110 (1958) 999.
[124] A.P. Jardine, H. Hedgeland, D. Ward, Y. Xiaoqing, W. Allison, J. Ellis, G. Alexandrowicz, New J. Phys. 10 (2008) 125026.
[125] J. Ellis, A.P. Graham, F. Hofmann, J.P. Toennies, Phys. Rev. B 63 (2001) 195408.
[126] H. Hedgeland, P. Fouquet, A.P. Jardine, G. Alexandrowicz, W. Allison, J. Ellis, Nature Phys. 5 (2009) 561.
[127] C.T. Chudley, R.J. Elliot, Proc. Phys. Soc. London 77 (1961) 353.
[128] J.W.M. Frenken, B.J. Hinch, J.P. Toennies, C. Wöll, Phys. Rev. B 41 (1990) 938.
[129] J. Ellis, A.P. Graham, J.P. Toennies, Phys. Rev. Lett. 82 (1999) 5072.
[130] G. Alexandrowicz, A.P. Jardine, H. Hedgeland, W. Allison, J. Ellis, Phys. Rev. Lett. 97 (2006) 156103.
[131] L.Y. Chen, S.C. Ying, Phys. Rev. Lett. 71 (1993) 4361.
[132] J.L. Vega, R. Guantes, S. Miret-Artes, D. Micha, J. Chem. Phys. 121 (2004) 8580.
[133] J. Ellis, A.P. Graham, Surf. Sci. 377 (1997) 833.
[134] P. DeGennes, Physica 25 (1959) 825.

[135] G. Alexandrowicz, P. Kole, E. Lee, H. Hedgeland, R. Ferrando, A. Jardine, W. Allison, J. Ellis, J. Am. Chem. Soc. 130 (2008) 6789.
[136] J.L. Vega, R. Guantes, S. Miret-Artes, J. Phys.: Condens. Matter 14 (2002) 6193.
[137] J.L. Vega, R. Guantes, S. Miret-Artes, J. Phys.: Condens. Matter 16 (2004) S2879.
[138] R. Martinez-Casado, J.L. Vega, A.S. Sanz, S. Miret-Artes, J. Phys.: Condens. Matter 19 (2007) 176006.
[139] R. Martinez-Casado, A.S. Sanz, S. Miret-Artes, J. Chem. Phys. 129 (2008) 184704.
[140] G.L. Squires, Introduction to the Theory of Thermal Neutron Scattering, Cambridge University Press, 1978 (Chapter 4).
[141] L.Y. Chen, S.C. Ying, Phys. Rev. B 49 (1994) 13838.
[142] R. Martinez-Casado, J.L. Vega, A.S. Sanz, S. Miret-Artes, J. Chem. Phys. 126 (2007) 194711.
[143] R. Guantes, J.L. Vega, S. Miret-Artes, E. Pollak, J. Chem. Phys. 119 (2003) 2780.
[144] J. Ellis, J.P. Toennies, Surf. Sci. 317 (1994) 99.
[145] P. Fouquet, M.R. Johnson, H. Hedgeland, A.P. Jardine, J. Ellis, W. Allison, Carbon, doi:10.1016/j.carbon.2009.05.018.
[146] A.P. Graham, F. Hofmann, J.P. Toennies, L.Y. Chen, S.C. Ying, Phys. Rev. B 56 (1997) 10567.
[147] A. Cucchetti, S.C. Ying, Phys. Rev. B 60 (1999) 11110.
[148] H. Lau, W. Kohn, Solid State Commun. 18 (1976) 553.
[149] A. Serra, R. Ferrando, Surf. Sci. 515 (2002) 588.
[150] G. Fratesi, G. Alexandrowicz, M.I. Trioni, G.P. Brivio, W. Allison, Phys. Rev. B 77 (2008) 235444.
[151] P. Senet, J.P. Toennies, G. Witte, Chem. Phys. Lett. 299 (1999) 389.
[152] P. Fouquet, R.A. Olsen, E.J. Barends, J. Chem. Phys. 119 (2003) 509.
[153] A.P. Graham, F. Hofmann, J.P. Toennies, J. Chem. Phys. 104 (1996) 5311.
[154] B. Poelsema, R.L. Palmer, G. Comsa, Surf. Sci. 136 (1984) 1.
[155] G. Ertl, M. Neumann, K.M. Streit, Surf. Sci. 64 (1977) 393.
[156] J.S. McEwen, S.H. Payne, H.J. Kreuzer, M. Kinne, R. Denecke, H.P. Steinruck, Surf. Sci. 545 (2003) 47.
[157] N.V. Petrova, I.N. Yakovkin, Surf. Sci. 519 (2002) 90.
[158] A. Barreiro, R. Rurali, E.R. Hernandez, J. Moser, T. Pichler, L. Forro, A. Bachtold, Science 320 (2008) 775.
[159] J.A. Stinnett, R.J. Madix, J. Chem. Phys. 105 (1996) 1609.
[160] M. DeKieviet, D. Dubbers, S. Hafner, F. Lang, in: R. Campargue (Ed.), Atomic and Molecular Beams: The State of the Art, vol. 161, Springer, 2001.
[161] G. Benedek, J. Toennies, Phys. Rev. B 46 (1992) 13643.
[162] G. Benedek, J. Ellis, N.S. Luo, A. Reichmuth, P. Ruggerone, J. Toennies, Phys. Rev. B 48 (1993) 4917.
[163] M. Wuttig, R. Franchy, H. Ibach, Z. Phys. B 65 (1986) 71.
[164] J.E. Lennard-Jones, A.F. Devonshire, Nature 137 (1936) 1069.
[165] H. Hoinkes, H. Wilsch, in: E. Hulpke (Ed.), Helium Atom Scattering from Surfaces, Springer Verlag, Berlin, 1992 (Chapter 6).
[166] M.C. Vargas, W.L. Mochán, Surf. Sci. 409 (1998) 130.
[167] M.I. Hernández, J. Campos-Martinez, S. Miret-Artés, R.D. Coalson, Phys. Rev. B 49 (1994) 8300.
[168] L. Tribe, Chem. Phys. 327 (2006) 468.
[169] L.W. Bruch, F.Y. Hansen, J. Chem. Phys. 122 (2005) 114714.
[170] J.M. Hutson, C. Schwartz, J. Chem. Phys. 79 (1983) 5179.
[171] J.R. Buckland, B. Holst, W. Allison, Chem. Phys. Lett. 303 (1999) 107.
[172] D.J. Riley, A.P. Jardine, S. Dworski, G. Alexandrowicz, P. Fouquet, J. Ellis, W. Allison, J. Chem. Phys. 126 (2007) 104702.
[173] D.J. Riley, A.P. Jardine, G. Alexandrowicz, H. Hedgeland, J. Ellis, W. Allison, J. Chem. Phys. 128 (2008) 154712.
[174] D. Riley, Atom Surface Potentials from Measurements of Selective Adsorption Resonances, PhD thesis, University of Cambridge.
[175] L.W. Bruch, R.D. Diehl, J.A. Venables, Rev. Mod. Phys. 79 (2007) 1381.
[176] G. Delgado-Barrio, P. Villarreal, P. Mareca, J.A. Beswick, Int. J. Quantum Chem. 27 (1985) 173.
[177] M. Hernández, S. Miret-Artés, P. Villarreal, G. Delgado-Barrio, Surf. Sci. 274 (1) (1992) 21.
[178] P. Linde, S. Andersson, Phys. Rev. Lett. 96 (2006) 086103.
[179] F.E. Tuddenham, H. Hedgeland, J.R.B. Knowling, A.P. Jardine, D.A. MacLaren, G. Alexandrowicz, J. Ellis, W. Allison, J. Phys.: Condens. Matter 21 (2009) 264004.
[180] S. Dworski, Atom Optical Methods for Surface Studies, PhD thesis, University of Cambridge, 2003.
[181] P.R. Griffiths, J.A. de Haseth, Fourier Transform Infrared Spectrometry, Wiley, New York, 1986.
[182] M.B.E. Wolf, Principles of Optics, sixth ed., Pergamon Press, 1984.
[183] P.W. Fowler, J.M. Hutson, Phys. Rev. B 33 (1986) 3724.
[184] D. Eichenauer, J.P. Toennies, Surf. Sci. 197 (1988) 267.
[185] J.R. Buckland, W. Allison, J. Chem. Phys. 112 (2000) 970.
[186] V. Druzhinina, M. DeKieviet, Phys. Rev. Lett. 91 (2003) 193202.
[187] B.N.J. Persson, Sliding Friction, Springer, 1998.